Characterization of contaminated sites and monitoring of processes accompanying bioremediation using spectral induced polarization imaging

Dissertation

zur Erlangung des Doktorgrades (Dr. rer. nat)

an der Mathematisch-Naturwissenschaftlichen Fakultät

der Rheinischen Friedrich-Wilhems-Universität Bonn

vorlegt

von

Adrián Flores Orozco

aus

Mexiko-Stadt, Mexiko

Bonn, 2012

Angefertigt mit Gehemigung an der
Mathematisch-Naturwissenschaftlichen Fakultät
der Rheinischen Friedrich-Wilhems-Universität Bonn

1. Referent: Prof. Dr. Andreas Kemna
2. Referent: Prof. Dr. Andrew Binley

Tag der Promotion: 21.08.2012

Erscheinungsjahr: 2012

Abstract

Measurements of spectral induced polarization (SIP) provide information about the electrical conduction and polarization properties of the subsurface, and their frequency dependence. Several laboratory studies in the last decade have highlighted the advantages of the SIP method for environmental applications. Nevertheless, to date only a few studies have been conducted at the field scale. This work demonstrates the application of SIP imaging at the field scale for the characterization of contaminants as well as for the monitoring of processes associated with the microbial remediation of contaminated sites.

The first part of this work presents a series of well-controlled measurements collected in the laboratory in order to investigate the distribution of data error in SIP tomographic measurements. Based on a thorough analysis of discrepancies between normal and reciprocal measurements, a power-law error model is proposed to quantify the error present in phase measurements. Implementation of the proposed error model in the inversion algorithm demonstrates an improvement in the resolution of the SIP images.

Based on the methodology proposed for the data analysis, the second part of this work investigates the potential of SIP images to discriminate between the source zone and the plume of dissolved contaminants in a BTEX (benzene, toluene, ethylbenzene and xylene) contaminated site. For dissolved BTEX (concentrations below 1.7 g/l), imaging results reveal an increase in the polarization values with increasing BTEX concentrations. An abrupt decrease to low polarization values is observed at higher BTEX concentrations (> 1.7 g/l) associated with the occurrence of free-phase products. Moreover, for BTEX concentrations below saturation concentration, the spectral response in the low frequencies (< 40 Hz) exhibits a typical Cole-Cole response, characterized by a frequency peak; whereas higher BTEX concentrations reveal a flat spectra and a low polarization effect. Debye decomposition is used to model the spectral response and investigate the correlation between spectral parameters and the concentration of BTEX contaminants.

The application of SIP imaging for the monitoring of a bioremediation technique is presented in the third part of this work. The studied remediation technique involves the stimulation of iron and sulfate reducing bacteria through acetate injection to remove aqueous uranium from groundwater. SIP monitoring images collected over a two-year period reveal spatiotemporal changes in the polarization of aquifer sediments. These changes correlate with variations in the concentrations of aqueous iron (Fe(II)) in groundwater and precipitation of metallic minerals (e.g., FeS) following the iterative stimulation of iron and sulfate reducing microorganism. However, poor reciprocity in the raw-data was observed for measurements collected at frequencies higher than 4 Hz, most probably as a result of electromagnetic coupling.

To overcome electromagnetic coupling at high frequencies, field procedures were improved permitting the collection of time-lapse SIP data sets with a good reciprocity in the frequency bandwidth between 0.06 and 256 Hz, as presented in the fourth part of this work. Cole-Cole model fitted to pixel values extracted from the computed SIP images permitted the determination of the chargeability and time constant. The determination of such parameters is critical for the application of existing petropyhsical models required for the hydrogeological characterization of the site. Results presented here reveal changes in time constant and chargeability values consistent with variations in groundwater geochemistry and pore-space geometry (due the accumulation of metallic particles) resulting from the stimulation of subsurface microbial activity.

Based on the results presented in this study, SIP imaging appears to be a suitable technique (i) to discriminate between source zone and plume of non-aqueous-phase contaminants, like BTEX; (ii) to monitor remediation techniques in order to maintain favorable conditions for the efficient remediation of contaminants; and (iii) to infer hydrogeological information of the shallow subsurface based on existing petro-physical models, for the assessment of contaminated sites and the evaluation of remediation techniques.

Zusammenfassung

Die Methode der spektralen induzierten Polarisation (SIP) liefert Informationen über elektrische Leitfähigkeits- und Polarisationseigenschaften des Untergrundes und deren Frequenzabhängigkeit. Im vergangenen Jahrzehnt haben verschiedene Laborstudien die Vorteile des Einsatzes von SIP im Umweltbereich aufgezeigt. Dennoch wurden bis heute nur wenige Untersuchungen auf Feldskala durchgeführt. Diese Arbeit veranschaulicht die Anwendung der SIP-Bildgebung zur Charakterisierung von Schadstoffen im Untergrund und Prozessen im Zusammenhang mit mikrobiellem Abbau an kontaminierten Standorten.

Die erste Studie beschäftigt sich mit Labormessungen, die an einem Tank durchgeführt wurden, um die Verteilung des Datenfehlers bei SIP-Messungen zu charakterisieren. Mittels einer statistischen Auswertung der Differenzen von normal und reziprok gemessenen Rohdaten wurde ein exponentielles Phase-Fehlermodell formuliert. Die Implementierung dieses Fehlermodells in einen Inversionsalgorithmus zeigt eine Verbesserung in der Auflösung der invertierten SIP-Tomogramme.

In der zweiten Studie wird das Potential der SIP-Bildgebung zur Differenzierung von Quell- und Transportzonen von BTEXen (Benzol, Toluol, Ethylbenzol und Xylol) geprüft. Die Messungen wurden auf dem Gelände eines ehemaligen Hydrierwerkes durchgeführt. Die SIP- Antworten zeigen einen Anstieg der Polarisation bei BTEX-Konzentrationen unterhalb der Sättigungskonzentration (~1.7 g/l). Eine deutliche Abnahmeder Polarisation ist bei höheren BTEX-Konzentrationen und dem Auftreten von freie-Phase Produkten zu verzeichnen. Außerdem weist das spektrale Antwortsignal bei BTEX-Konzentrationen bis zu 1.7 g/l einen charakteristischen Höchstwert in der Frequenz auf, wohingegen höhere BTEX- Konzentrationen und das Auftreten von freie-Phase Produkten am Schadstoffherd eher ein flaches Spektrum und einen geringen Polarisationseffekt für Frequenzen bis 40 Hz zeigen. Die SIP-Antworten wurden mittels Debye-Zerlegung modelliert, um die Korrelation zwischen den spektralen Parametern und den BTEX-Schadstoffen zu ermitteln.

Der dritte Teil der vorliegenden Arbeit behandelt die Anwendung der SIP-Bildgebung als Beobachtungsverfahren der Langzeiteffizienz einer Bio-Remediationstechnik. Diese benutzt Acetat-Injektionen zur Stimulierung von eisen(Fe)- und sulfatreduzierenden Bakterien, die gelöstes Uran aus dem Grundwasser entfernen können. Das Monitoring über einen Zeitraum von zwei Jahren zeigt sowohl räumliche als auch zeitliche Änderungen des Polarisationseffekts im Aquifer. Diese Änderungen korrelieren mit dem Anstieg des gelösten Eisens (Fe(II)) sowie mit der Ausfällung metallischer Minerale (z.B. FeS) nach der iterativen Stimulierung eisen- und sulfatreduzierender Mikroorganismen.

Eine geringe Reziprozität in den Rohdaten wurde auf Grund elektromagnetischer Kopplung bei Frequenzen von mehr als 4 Hz festgestellt. Um diese elektromagnetische Kopplung zu minimieren, wird im letzten Kapitel dieser Studie eine Methode zur Feldmessung vorgestellt, die das Aufzeichnen von SIP-Daten zu verschiedenen Zeiten mit einer guten Reziprozität im Frequenzbereich von 0,06 bis 256 Hz erlaubt. Die Tomogramme ermöglichen für unterschiedliche Zeiten die Bestimmung der charakteristischen Zeitkonstante, die für die Anwendung von petrophysikalischen Modellen aus Labormessungen notwendig ist. Die gemessenen Änderungen von Zeitkonstante und Aufladbarkeit stimmen dabei mit Änderungen in der Geochemie des Grundwassers und der Porenraumgeometrie überein, die durch die unterirdische Stimulierung der mikrobakteriellen Aktivität erzeugt wurden.

Basierend auf den beobachteten Korrelationen erweist sich die SIP-Bildgebung als eine geeignete Technik, um (i) zwischen Quell- und Transport-Bereichen von nicht oder schwer wasserlöslichen organischen Schadstoffen, wie BTEXen, zu unterscheiden und (ii) über den Einsatz von Sanierungsmaßnahmen zur Entscheidungsunterstützung über den effizienten Einsatz der Remediationstechnik zu überwachen und (iii) hydrogeologische Informationen des nahen Untergrundes unter Zuhilfenahme petrophysikalischer Modelle zur Beurteilung kontaminierter Standorte und Evaluation geeigneter Sanierungsmaßnahmen abzuleiten.

Resumen

Mediciones de inducción polarizada espectral (SIP por sus siglas en inglés) permiten obtener información acerca de las propiedades de conducción y polarización eléctrica del subsuelo, y su dependencia a diferentes frecuencias. Comúnmente utilizada para la prospección de yacimientos metálicos, en los últimos años varios estudios en el laboratorio han demostrado las ventajas de la aplicación del método de SIP en el área ambiental. Sin embargo, a la fecha, muy pocas investigaciones han sido llevados acabo en el campo. A través de cuatro estudios, éste trabajo intenta demostrar las aplicación de la técnica de imágenes de SIP para la caracterización de contaminantes y el monitoreo de procesos asociados con técnicas bioremediación para sitios contaminados.

La primera parte de éste estudio presenta una serie de mediciones tomadas en un tanque en el laboratorio, con el fin de investigar la distribución y características del error presente en mediciones tomográficas de SIP. Por medio de un detallado análisis estadístico de las discrepancias entre mediciones normales y recíprocas, se propone modelo matemático para cuantificar el error presente en mediciones de SIP. La implementación de éste modelo, en el algoritmo de inversión, permitió la obtención de imágenes de SIP con una mayor resolución. La segunda parte de éste trabajo investiga la posibilidad de distinguir zonas fuente y pluma de dispersión, para sitios contaminados con BTEX (benceno, tolueno, ethybenceno y xileno). Las imágenes de SIP, revelaron un incremento en los valores de polarización inducida relacionado con el incremento en las concentraciones de BTEX, para concentraciones de BTEX menores a

1.7 g/l. Un abrupto cambio a valores muy bajos de polarización inducida se reporta para concentraciones de BTEX mayores a 1.7 g/l y la presencia de fase libre del contaminante. Además, la respuesta espectral revelo un modelo típico de Cole-Cole en las bajas frecuencias (< 40 Hz), en áreas asociadas con un máximo de 1.7 g/l de BTEX; mientras que mayores concentraciones de BTEX se caracterizaron por una respuesta constante (sin cambios en las diferentes frecuencias) en mediciones recolectadas en las bajas frecuencias (< 40 Hz). Se utiliza el método de la descomposición de Debye para poder describir la respuesta espectral, y poder así investigar la correlación existente entre parámetros espectrales de SIP y variaciones en la concentración de contaminantes.

La tercera parte de este trabajo presenta la aplicación de imágenes de SIP para el monitoreo de una técnica de bioremediación. Dicha remediación consiste en la inyección de acetato para estimular el crecimiento y actividad de bacterias reductoras de hierro y sulfatos. Dichas bacterias son capaces de disinuir las concentraciones de uranio presente en agua subterránea de un sitio contaminado. El monitoreo a lo largo de más de dos años demostró un decremento en las concentraciones de uranio en el agua subterránea, así como cambios en la polarización de los sedimentos del subsuelo. Estos cambios están

estrechamente relacionados con variaciones en las concentraciones de hierro disuelto en agua subterránea (Fe(II)) y la precipitación de minerales metálicos (por ejemplo FeS) causados por la estimulación de actividad de los microorganismos. Sin embargo, mediciones de SIP en frecuencias mayores a 4 Hz revelaron una alta contaminación de los datos por campos electromagneticos parásitos, provocando una mala correlación entre mediciones normales y recíprocas.

Para poder incrementar la calidad de mediciones a frecuencias mayores a 4 Hz, en este trabajo se propone una mejora en las técnicas de campo. Con base en estos nuevos procedimientos, se obtuvieron datos confiables en un ancho de banda de 0.06 a 256 Hz, como se describe en el cuarto estudio de éste trabajo. Imágenes de SIP para dichos datos permitieron determinar los valores de cargabilidad (asociada con la magnitud del efecto de polarización espectral) y la constante de tiempo (inversamente proporcional a la frecuencia en el que se registró el mayor efecto de polarización inducida). La obtención de dichos parámetros es critica para poder aplicarlos modelos petro-físicos existentes. Cambios en cargabilidad y la constante de tiempo observados son consistentes con variaciones en la química de agua subterránea y en la geometría del espacio poroso del acuífero causado por la estimulación de microorganismos en el subsuelo.

Con base en los resultados presentados en este estudio, la técnica de imágenes de SIP demuestra ser una herramienta útil para (i) la caracterización de la zona fuente y pluma de contaminantes, como BTEX; (ii) para el monitoreo de procesos durante la remediación de contaminantes (por ejemplo cambios en el agua subterránea), de forma que se puedan mantener condiciones que favorecen la remediación de contaminantes; y (iii) para estimar información hidrogeológica del subsuelo (tal como conductividad hidráulica) con base en modelos petro-físicos existentes, tal que se pueda predecir el transporte de contaminantes o la pérdida en la eficacia en las técnicas de remediación.

ACKNOWLEDGMENTS

As every Journey, this one would not safely land without the valuable help and guide of a great number of advisers and friends. First of all, I want to thank my supervisor Andreas Kemna, for giving me the opportunity to join his team, to learn and to make a lot of errors on the way to conclude this work. In the same way, I would not be able to write this study without the advice and help of Ken Williams, who gave me the opportunity to get involved in very interesting projects and has been a good friend for the last years. I also want to thank Andrew Binley, for his advices and suggestions which permitted me to improve my understanding of the topics to be discussed in this work.

I also want to acknowledge the selfless help and advices of Egon Zimmermann, Bernd Kröger, Christoph Oberdörster, Anja Drenkelfuß, Klaus Haaken, as well as the working groups ICG-IV in the FZ-Jülich and Applied Geophysics in the University of Bonn, always ready to aid and support my steps on this Journey.

In a very special place, I want to thank for the patience and the unconditional support of my family: mi madre, mi padre, mi hermano, mi sobrino Arturo and, specially, Yana, who have been walking with me all this time and without her love and time I would never be able to finish this.

Finally, I want to acknowledge the CONACyT-DAAD scholarship which financed my studies and work.

Adrián Flores Orozco

TABLE OF CONTENTS

1. INTRODUCTION 17

2. BACKGROUND 21

2.1. Remediation techniques 21

2.2. Drilling-based methods for site characterization and monitoring 24

2.3. Electrical methods for site characterization and monitoring 25

2.3.1. Electrical Resistivity 25

2.3.2. Induced Polarization 28

3. DATA ERROR QUANTIFICATION IN SPECTRAL INDUCED POLARIZATION IMAGING 37

3.1. Abstract 37

3.2. Introduction 37

3.3. Data error treatment in complex resistivity imaging 38

3.3.1. Complex resistivity inversion scheme 38

3.3.2. Parameterization of resistance error 40

3.3.3. Parameterization of phase error 40

3.4. Analysis of spectral data from a laboratory experiment 41

3.4.1. Experimental setup and measurement scheme 41

3.4.2. Data analysis and new phase error model 44

3.5. Imaging results 48

3.6. Application to single-frequency field data 51

3.6.1. Setup 51

3.6.2. Results 51

3.7. Discussion 54

3.8. Conclusions 56

4. DELINEATION OF SUBSURFACE HYDROCARBON CONTAMINATION AT A FORMER HYDROGENATION PLANT USING SPECTRAL INDUCED POLARIZATION IMAGING 59
4.1. Abstract 59
4.2. Introduction 59
4.2.1. Induced Polarization Imaging 61
4.3. Material and Methods 65
4.3.1. Site description 65
4.3.2. Groundwater sampling 65
4.3.3. Direct-push survey 66
4.3.4. Electrical imaging 66
4.4. Results 68
4.4.1. Conductivity images 68
4.4.2. Phase images 69
4.5. Discussion 73
4.6. Conclusions 77

5. USING COMPLEX RESISTIVITY IMAGING TO INFER BIOGEOCHEMICAL PROCESSES ASSOCIATED WITH BIOREMEDIATION OF A URANIUM-CONTAMINATED AQUIFER 79
5.1. Abstract 79
5.2. Introduction 79
5.3. Material and Methods 81
5.3.1. Complex resistivity method 81
5.3.2. Site description 83
5.3.3. Experimental set-up 84
5.3.4. Inversion approach 86
5.3.5. Data error parameterization 87
5.4. Results 88
5.5. Discussion 97
5.6. Conclusions 101

6. TIME-LAPSE SPECTRAL INDUCED POLARIZATION IMAGING OF STIMULATED URANIUM BIOREMEDIATION 105
6.1. Abstract 105
6.2. Introduction 105
6.3. Methods 107
6.4. Results 111
6.4.1. Raw data analysis 111
6.4.2. Imaging results 113
6.4.3. Geochemical interpretation of SIP images 115
6.4. Conclusions and Outlook 120

7. CONCLUSIONS 121

8. PERSPECTIVES 125

9. REFERENCES 127

1. INTRODUCTION

Groundwater comprises more than 98% of the world's available freshwater, excluding the water contained in polar ice (Bouwer, 2002) and supplies approximately over 1.5 billion urban dwellers (Zekster and Margat, 2004). However, in addition to natural processes, practically every type of human physical activity may cause groundwater quality problems (Zaporozec and Miller, 2004). For instance, industry and energy production accounts for nearly 20% of total global water withdraw (UN WWAP, 2000) and this water is typically returned in a degraded condition. It is estimated that industry is responsible for dumping worldwide 300-400 millions of tons of heavy metals, solvents and other waste into waters each year (UN WWAP, 2000). Additionally, the disposal of mining solid waste (tailings) and the accidental (or illegal) spills of hazardous substances represent major threats to groundwater quality (U.S. EPA, 1997).

The increasing demand in drinking water and widespread groundwater contamination has prompted the development of different remediation techniques to improve groundwater quality. In order to select an adequate remediation method, it is necessary to conduct a detailed assessment of the existing and potential sources of contamination, the actual contaminated area and its spatial extent. The characterization of contaminated sites should include the following:

- Assessment of the groundwater flow system and hydraulic parameters (e.g., porosity, hydraulic conductivity), and characterization of preferential flow paths.
- Determination of the concentration and extent of contamination.
- Delineation of contamination source area and the plume of dissolved contaminants.
- Characterization of contaminant processes (e.g., attenuation), as well as transport rates and pathways.

Once remediation has started, a frequent assessment of changes in groundwater chemistry and hydraulic parameters is also critical to maintain high rates of remediation and operational efficency. Changes in groundwater geochemistry (e.g., pH) concurrent with the precipitation of minerals or the accumulation of microbial cells (e.g., biofilms) may lead to clogging effects, loss in the reactivity of the materials or shifts in the microbial community, typically resulting in a decrease in the effectiveness of the remediation techniques by, e.g., reducing the rates of remediation, the scale at which the remediation takes place or its life time (as addressed in the next chapter). Moreover, it has been observed that the combination of certain processes may result in the release of toxic compounds, for example aerobic bacteria is commonly effective to degrade volatile organic compounds; however, reduced chlorinated hydrocarbons may become toxic if they are in contact with aerobic bacteria.

Commonly, the analyses of water and soil samples collected in boreholes (hereafter referred to as drilling-based methods) are used for the characterization of contaminated sites and for the monitoring of remediation techniques. However, their associated cost and limited spatial and temporal resolution has urged the development of new methods. Non-invasive geophysical methods appear as a suitable solution due to their relatively low cost and high spatial resolution, especially in comparison to drilling-based methods. Among the different geophysical methods, induced polarization (IP) has emerged as a very promising tool for environmental applications, particularly if measurements are performed at different acquisition frequencies (referred to as spectral induced polarization, SIP). During the last decade, a vast number of studies performed in the laboratory have demonstrated the sensitivity of SIP measurements to relevant environmental processes, such as, to changes in groundwater geochemistry and pore-space geometry, to the accumulation of microbial cells, and to processes associated with microbial growth (e.g., attenuation of contaminants).

This study investigates the potential of SIP images to gain information about geochemical, microbial and hydrogeological changes in the subsurface due to groundwater contamination and remediation at the field scale. While numerous laboratory studies have demonstrated the value of using spectral induced polarization (SIP) measurements to infer information about contaminated soils, pore-space geometry, or induced pore-scale processes induced trough remediation, remarkably few studies have been conducted at the field scale to validate such inferences. In particular, this work evaluates the application of the SIP imaging method for the assessment of hydrocarbon-contaminated sites and for the monitoring of processes associated with bio-stimulation experiments performed at the field scale. In addition, this study also evaluates the relevance of SIP imaging in comparison with single frequency (IP) surveys and/or measurements collected in the time-domain (TDIP). To better address the objectives of this study, this work also provides a revision of field procedures required for the acquisition of reliable SIP data sets, as well as a thorough data analysis and processing, in order to adequately quantify the error in the data sets and improve the resolution of the computed SIP images.

This work is divided into seven chapters, with the introduction to the problem, the description of the objectives and structure of this work being addressed in this first chapter. The next chapter provides a description of the most common methods used nowadays for the remediation of contaminated sites. The second chapter also presents a description of the drilling-based methods, applied to date, for site characterization and monitoring, followed by the introduction of the SIP method.

An adequate data analysis prior to the inversion is critical for quantitative imaging. However, to date only a few studies have addressed the description of data-error in SIP tomographic measurements. Hence, the third chapter of this work deals with quantification of the data error in SIP measurements and describes the methodology used

in this study for the analysis of raw data prior to the inversion. To better address this, the third chapter begins with a revision on the sources of error in SIP measurements, as well as the previous approaches for the quantification of data-error. Then, a description of the inversion algorithm used to compute the images in this study is presented, as well as the implications of the error parameterization in this inversion schema. This is followed by the description of the laboratory experiments and raw-data analysis performed to investigate and quantify the distribution of data error in SIP measurements. The implementation of the proposed error quantification in the inversion algorithm is then used for the inversion of the laboratory data. The chapter three presents a comparison of the resulting images by means of the proposed error parameterization and those obtained by means of previous error parameterization, as well as the analysis and imaging of a single-frequency data set collected at the field scale.

The fourth chapter presents the application of the SIP imaging method for the discrimination of source zone and plume in a site contaminated with benzene, toluene, ethylbenzene and xylene (BTEX), on the ground of a former hydrogenation plant. This chapter also presents the comparison of images for data collected before and after the removal of anthropogenic structures (associated with the hydrogenation plant), in order to assess the effect of such structures in SIP imaging results. Additionally, resulting images are compared for measurements collected in the frequency-domain and in the time-domain to evaluate the imaging results for both acquisition methods; to my knowledge such comparison has not been addressed before for field-scale imaging results. Finally this chapter investigates the correlation of spectral parameters as obtained from Debye decomposition in an imaging framework and BTEX concentrations.

The fifth chapter presents SIP imaging results computed for data collected at regular intervals over a two years period during and after a set of bioremediation experiments. The aim is to demonstrate the use of SIP images for monitoring biogeochemical changes in the subsurface accompanying stimulation of indigenous aquifer microorganisms. The correlation between the observed SIP response and relevant geochemical parameters at different periods of the remediation approach is investigated in order to evaluate the potential of SIP images to detect changes in groundwater geochemistry that affect the efficiency of the bio-remediation method.

The sixth charter presents time-lapse SIP imaging results for a short bio-stimulation experiment similar to those presented in the fifth chapter; however with a particular improvement in the field procedures in order to collect data at a wider frequency band. The aim of this chapter is to evaluate the application of existing petrophysical models linking the SIP response to changes in pore-space geometry associated with the precipitation of metallic minerals. Following this, I present in chapter seven the conclusions of this work and close in chapter eight with remarks regarding my perspectives for future studies.

2. BACKGROUND

2.1. Remediation techniques

Different remediation techniques have been developed aiming the clean-up of contaminated sites to improve groundwater quality. In the following the most common remediation approaches used nowadays will be described, particularly highlighting their main advantages and limitations.

The pump-and-treatment approach was one of the first developed techniques for groundwater remediation and it still is the most used method worldwide. It involves the extraction (pumping) of contaminated groundwater by wells or drains and *ex situ* treatment of the extracted water (Mackay and Cherry, 1989), for example to remediate chlorinated compounds (e.g., Mackay and Cherry, 1989; Mackay et al., 2000; McCarty, 2010; Vignola et al., 2008). However, such approach is shown to be commonly inefficient, with site remediation requiring several years to decades to be completed, and thus, resulting in high expenses (e.g., Karn et al., 2009). To overcome this disadvantage, different approaches have been developed to increase the mobility of the contaminants and, thus, enhancing a higher contaminant extraction. Some methods use high temperatures (> 100 °C, depending on vapor pressure of the contaminant) to mobilize and volatilize contaminants (e.g., Chesnut, 1994); the thermal treatment based on the steam-enhanced extraction; electrical resistive heating (e.g., Friis et al., 2006) and thermal conductive heating. However, such approaches are typically very expensive due to the large energy consumption and infrastructure required, as well as several concerns raised due to the impacts on natural microbial populations (Friis et al., 2006; Grieger et al., 2010). Other approaches may include the injection of chemical additives with surface active agents (surfactants), or alcohols, which increase the water solubility, for instances of the oil phase (e.g., Knox et al., 1999; Krebsyuill et al., 1995; West,1992), or the injection of chemical agents for contaminant degradation via oxidation (e.g., Chen et al., 2009; Crimi and Siegrist, 2004; Ferrarese et al., 2008; Tsai et al., 2011; Urynowicz and Siegrist, 2005; Weichgrebe and Vogelpohl, 1994). However, such techniques rely on the injection of relatively harsh chemicals which may trigger undesired effects like mobilization of metals (Crimi and Siegrist, 2004). An additional disadvantage of *ex situ* treatment is that they commonly result in highly contaminated waste that has to be disposed.

The installation of granular iron permeable reactive barriers (PRB) have emerged as an effective *in situ* treatment method for the remediation, for instance of petroleum hydrocarbons (e.g., Arora et al., 2011; Chen et al., 2011; Vesela et al., 2006), chlorinated hydrocarbons (e.g., Blowes et al., 2000; Choi et al., 2007; Jeen et al., 2011; Puls et al., 1999; Tsai et al., 2011; Urynowicz and Siegrist, 2005), chromium (e.g., Garg et al., 2011; Jeen et al., 2011; Li and Benson, 2010; Puls et al., 1998; Wilkin et al., 2003;

Wilkin et al., 2005; Zhou et al., 2009), arsenic (e.g., Ahn et al., 2003; Cortina et al., 2010; Cundy et al., 2008; Hayes et al., 2011; Morrison et al., 2003; Wilkin and Lee, 2010; Wilopo et al., 2008), uranium (e.g., Morrison et al., 2001; Morrison et al., 2006; Naftz et al., 2003), among other contaminants (e.g., Calabro and Moraci, 2010; Farrell and Mishra, 2004). The PRB are typically installed as vertical treatment walls filled with a reactive material, which act as electron donor- or acceptor-releasing compounds (Richardson and Nicklow, 2002). Typically granular zero-valent iron (Fe^0) is used as reactive material; however, other reduced metal or materials can also be used, depending on the contaminant (Richardson and Nicklow, 2002). As the contaminated groundwater flows through this zone, contaminants are degraded and transformed to innocuous components, adsorbed, or chemically altered so that they form insoluble precipitates (Richardson and Nicklow, 2002). Zero-valent PRB account for the majority of the PRB used worldwide, with more than 200 installations (Jeen et al., 2006).

Here, the PRB use the strongly negative reactive potential of Fe^0 to reduce oxidants such as chlorinated aliphatics to non-chlorinated compounds (e.g., Baciocchi et al., 2003; Chen et al., 2011) or to enhance the reductive precipitation of soluble contaminants, like uranium U(VI) (e.g., Dickinson and Scott, 2010), and heavy metals like soluble copper Cu(2+) or zinc Zn(2+) (e.g., Rangsivek and Jekel, 2005). However, precipitation of by-products within the PRB, mostly carbonate minerals, or the formation and accumulation of microbial cells (biofilms) lead to pore-clogging effects limiting the long-term efficacy of the PRB (e.g., Jeen et al., 2006; Köber et al., 2002; Mackenzie et al., 1999; Zhang and Gillham, 2005). Moreover, the clean-up effect of the PRB is spatially restricted to the groundwater flowing through it, limiting their application on a large scale (N´Guessan et al., 2008).

In order to overcome difficulties and limitations arising from the installation of PRB, recent studies on the injection of reactive nanomaterials (individual particles smaller than 100 nm) for the *in situ* transformation and detoxification of pollutants have been conducted at the field scale (e.g., Grieger et al., 2010; Karn et al., 2009). In particular, iron nanoparticles (nFe^0) have received much attention regarding the high surface area to volume ratio, high surface energy and their potential for groundwater treatment (Dickinson and Scott, 2010; Zhang et al., 1998). The injection of nFe^0 permits the remediation of sites not accessible with PRB, e.g., underneath buildings or contaminants located below 5 m depth (e.g., Elliott and Zhang, 2001; Karn et al., 2009). Furthermore, remediation is significantly faster compared to other approaches (Grieger et al., 2010; Karn et al., 2009). To date, the injection of n Fe^0 has been used to treat mining waste, chlorinated and polycyclic aromatic hydrocarbons, atrazine, pesticides, radionuclides (e.g., uranium) and heavy metals (Abernathy et al., 2007; Amir and Lee, 2011; Barnes et al., 2010; Bezbaruah et al., 2009; Gan et al., 2009; Schrick et al., 2000; Sethi et al., 2009; Taghavy et al., 2010; Varanasi et al., 2007; Will et al., 2003; Yu Ting et al., 2009; Zhang, 2004). Although promising, the main concern of this remediation technique is related to the delivery and transport of the injected nFe^0. The

surface of nFe^0 will quickly oxidize, leading to the formation of magnetite or maghemite, decreasing the reactivity of the particles, i.e., the effectiveness of the technique (Sethi et al., 2009). In addition, Fe^0 particles are prone to rapid aggregation, resulting in a loss in reactivity and decreased mobility (Theron et al., 2008). Current research explores the possibility to coat Fe^0 particles with different surface modifiers to better control their reactivity and mobility (Amir and Lee, 2011; Bennett et al., 2010; Grieger et al., 2010; He et al., 2009; Zhang et al., 2010). However, a limited mobility has been observed even for coated Fe^0, limiting their distribution, and thus, the extension of the remediation area (Jones et al., 2011; Schrick et al., 2004). Moreover, rapid agregation may also impede the delivery of the Fe^0 (Lowry et al., 2008), remaining a challenge for the application of the method on a large scale. Besides this, many concerns have been raised due to the possible long-term effects of injected nanoparticles and by-products, particularly regarding its toxicology and unknown environmental risks, urging the development of monitoring methods to better assess fate and transport of Fe^0 (Grieger et al., 2010).

The activity of microorganisms naturally found in the subsurface might lead to the attenuation of contaminants or their transformation into less toxic compounds through metabolic or enzymatic processes. Microorganisms, such as bacteria, grow by transferring electrons from an electron donor to an electron acceptor; through this process reducing- oxidation (redox) reactions occur. Aerobic degradation takes place only when oxygen is available, here bacteria use oxygen as the terminal electron acceptor (TEA); whereas anaerobic degradation occurs in absence of oxygen, for a diversity of TEAs, like iron (for iron-reducing bacteria) or sulfate (sulfate-reducing bacteria). It has been demonstrated that volatile organic compounds (VOCs), like BTEX, are degraded by microorganisms in aerobic conditions (e.g., Chapman et al., 1997; Chen et al., 2011; Gibson et al., 1998; Schirmer et al., 2006; Vesela et al., 2006), as well as polycyclic aromatic hydrocarbons (PAHs) (e.g., Samanta et al., 2002). Anaerobic degradation has been explored, for example, to treat mining waste water through the oxidation of pyrite enhanced by sulfate-reducing bacteria (e.g., Elliott et al., 1998; Neculita et al., 2007; Radhika et al., 2006). In addition, iron-reducing bacteria have been used to remove uranium from groundwater by reducing mobile uranium (U(VI)) to U(IV) and, thus lowering the concentration of uranium in groundwater or the extension of contaminant plume (e.g., Lovley et al., 1991; Vrionis et al., 2005). A complete review of the microbial processes involved in the biodegradation of metal and radionuclide contaminants through anaerobic process is given, for example in the works of Barkay and Schaefer, (2001) and Nies (1999). Although bioremediation may be performed in a natural way (natural attenuation), stimulated bioremediation aims to maintain high rates of contaminant degradation through the injection of compounds in order to preserve conditions favorable for the targeted microbial activity (e.g., Boopathy, 2000).

In situ bioremediation offers many advantages compared to other methods. In terms of cost, bioremediation reduces the expenses associated with excavation or installation of

facilities (e.g., PRB), and it does not require the disposal of contaminated material. In addition, the soil is not destroyed due to the injection of harsh chemicals or the construction of utilities. Furthermore, the contamination is not transferred elsewhere and the method has a greater public acceptance than other remediation approaches. The main disadvantage is that bioremediation requires the occurrence of adequate bacteria at the contaminated site (i.e., the right bacteria in the right place); although exogenous microbial populations might be added, just a few studies have been conducted in this direction. Furthermore, the effectiveness of the bioremediation is strongly dependent on the availability of electron donors (energy sources), TEA, an adequate pH and nutrients (for a detailed description see, for instances, Boopathy, 2000). Variations in pH and temperature may shift microbial community, decreasing the rates of biodegradation, or significantly, impeding microbial growth or resulting in the release of toxic compounds. Hence, stimulated bioremediation requires an adequate monitoring in order to know when the subsurface conditions need to be adjusted to maintain adequate rates of biodegradation.

2.2. Drilling-based methods for site characterization and monitoring

To date, drilling-based methods are the most common technique applied for site characterization and monitoring of groundwater. Those methods are based on direct measurements of relevant parameters (e.g., lithology, concentration of contaminants, and hydraulic conductivity) in open holes or in soil and water samples collected in existing wells or during the drilling of new wells. Based on the measurements performed, interpolated maps might be constructed to characterize the distribution of aquifer properties, for instances, the extent of contaminant plumes, source-zones, or enhanced remediation. It is clear that the resolution of this method will be given by the number and distribution of wells, as well as the number of samples, leading to an increase in the costs if high resolution is required, particularly if new wells need to be drilled.

Aquifer heterogeneities and well design (e.g., diameter, screening length) may result in an inadequate sampling, biasing the estimated concentration of contaminants. Multilayer sampling techniques have been proposed to overcome this problem (e.g., Puls and Paul, 1997). Those are based on small discrete multi-layer well points, which permit the identification of extremely sharp vertical concentration gradients over very short distances (< 3 m) in subsurface systems (e.g., Nikolaidis et al., 1994). It has also been proposed to measure the contaminant concentration versus pumping time (e.g., Bauer et al., 2004; Jarsjö et al., 2005). Such a technique, referred to as an integral approach, is based on the assumption that the longer the pumping takes, the further the sample is drawn from the well and the bigger the sampling volume; thus the uncertainty in the concentration measured in water samples decreases considerably as the sampled volume of water increases (Béland-Pelletier et al., 2011; Destouni and Graham, 1997). Although such methods provide more accurate estimations of contaminant concentrations,

they also require longer acquisition times, which may become a limitation when sampling and analyzing a large number of wells, as well as assessing fast processes during, for instances remediation. In addition, integral approaches or multilayer sampling are typically associated with larger volumes of extracted water that needs to be disposed afterwards.

In order to improve the spatial resolution of drilling-based methods, faster sampling methods (referred to as "push" techniques) have also been conducted for the characterization of contaminated sites. These "push" technologies are based on probes of very small diameter which can be advanced into the ground to collect water or soil samples, avoiding the pre-construction of an open hole. Modern devices also permit the collection of different hydrogeological, geotechnical and geophysical properties by the so-called Direct-Push technologies (e.g., McCall et al., 2006). However, those methods are not applicable to all site conditions and a large number of samples are required to reliably characterize contaminated sites, also resulting in elevated costs.

2.3. Electrical methods for site characterization and monitoring

Another approach to site characterization is based on geophysical exploration. Here, different techniques are applied to gain information about the physical properties (e.g., magnetic, elastic, electric) of the subsurface. From these measurements, the distribution of hydrogeological properties of the aquifer can be inferred. Due to their relative low costs and robustness, electrical methods are the mostly used geophysical techniques in environmental applications. Furthermore, electrical measurements are typically collected in conjunction with other methods, like seismic (e.g., Garambois et al., 2002), ground penetrating radar (e.g., Slater and Reeve, 2002; Kettridge et al., 2008; Wisitsoraat et al., 2008), self potential (SP) (e.g., Revil et al., 2004), and time domain reflectometry (TDR) (e.g., Oberdörster et al., 2010). The deployment of more than one geophysical method permits to gain complementar y information and improve the interpretation of results, with numerous studies performed in the laboratory and a few at the field scale. This section provides a short summary of the concepts underlying the electrical methods, referencing only studies performed at the field scale, especially for the assessment of contaminated sites, beginning with the electrical resistivity (dc-method), before introducing the spectral induced polarization (SIP).

2.3.1. Electrical Resistivity

Geophysical methods aiming at the characterization of electrical properties of the subsurface have emerged as a promising tool for environmental studies, regarding the intuitive connection between groundwater conduction and electrical conductivity, as mentioned in Slater (2007). Furthermore, these methods are non-invasive, thus measurements can be collected without disturbing the study area and avoiding expenses due to drilling or the disposition of extracted materials. Moreover, modern multi-channel measuring devices are able to collect thousands of measurements in a few hours. This, in

conjunction with state-of- the-art computational resources and sophisticated inversion algorithms, has lead to the development of imaging techniques that provide a powerful tool for site characterization (Binley and Kemna, 2005). The computed images (sometimes referred to as tomograms) provide a clear advantage in terms of spatial resolution, permitting to gain detailed information of the subsurface, for instance about heterogeneities or preferential flow-paths, which is poorly solved solely by drilled-methods (Abdel Aal et al., 2006). Furthermore, time- lapse measurements can be collected to investigate temporal changes for groundwater monitoring in order to assess fate and transport of contaminants or to evaluate the effectiveness of remediation methodologies.

The electrical resistivity method is probably the most applied geophysical method for environmental studies. First described by the brothers Schlumberger (Schlumberger, 1941), this method is based on a four-electrode arrays. Here two electrodes are used to inject current and the other two measures the resultant electric voltage. Nowadays multi-electrode measurements can be performed simultaneously with tens to hundreds of electrodes placed on the surface, in boreholes or in combinations of both. Inversion of multi-electrode measurements (voltage-to-current ratios) permits to compute the distribution of electrical resistivity values (ρ) in the subsurface. Based on its analogy to medical tomographic applications, the inversion of multi-electrode measurements has been called electrical resistivity tomography (ERT), for example in Daily and Owen (1991), Daily et al. (2004). However, as denoted in Binley and Kemna (2005), the term tomography, for geophysical investigations, was originally used for measurements in which sensors bounded the region under investigation, which is not the case in subsurface investigations.

To better account for the analogy with the groundwater flow, electrical resistivity values (ρ) can be expressed in terms of its reciprocal, the electrical conductivity ($\sigma=1/\rho$). The electrical conductivity (σ) of sediments without electronically conductive minerals is mainly controlled by the electrical properties of the pore-filling electrolyte (i.e., electrical conductivity of the electrolyte, σ_W), the porosity (θ) and water saturation (S), described by a well-established petrophysical relationship in the absence of surface conductivity (Archie, 1942):

$$\sigma_b = a\sigma_w\theta^m S^n, \tag{2.1}$$

where σ_b is the bulk formation electrical conductivity and a, m and n represent dimensionless parameters related to the grain shape, cementation and saturation respectively. Taking into account the model presented in Equation 2.1, ERT studies conducted at the field scale have been used for the characterization of aquifers (e.g., Bowling et al., 2005; Dahlin, 2001; Miller et al., 2008; Singhal et al., 1998; Sumanovac, 2006) and to estimate relevant hydrogeological parameters like porosity and hydraulic conductivity (e.g., Boucher et al., 2009; Daily and Ramirez, 1984; Linde et al., 2006;

Looms, 2007; Purvance and Andricevic, 2000a; Purvance and Andricevic, 2000b). Based on the monitoring of tracer test experiments, inversion of time-lapse ERT data-sets have also proven to provide reliable estimates on flow and transport parameters (e.g., Day-Lewis and Singha, 2008; Englert et al., 2007; Kemna et al., 2002; Oldenborger et al., 2007; Singha and Gorelick, 2006).

Regarding the higher σ_W of saline water, ERT images have been used to delineate seawater intrusion and changes in sea- and groundwater interface (e.g., de Franco et al., 2009; Frohlich and Urish, 2002; Nassir et al., 2000; Nguyen et al., 2009; Ogilvy et al., 2009). Furthermore, it has been observed that organic contaminants (e.g., petroleum hydrocarbons or lixiviates from landfills) dissolved in groundwater may act as insulators decreasing the σ_W in contaminated groundwater (e.g., Mazac et al., 1987; Urish, 1981). Regarding this, ERT images have been used to map landfill geometry (e.g., Chambers et al., 2006; Dahlin, 2001; Naudet et al., 2004); and some attempts have been made to delineate petroleum hydrocarbon contaminated plumes and associated changes during pump-and-treat remediation processes (e.g., Bentle y and Gharibi, 2004; Chambers et al., 2010; Daily and Ramirez, 1995; Goes and Meekes, 2004; Ramirez et al., 1993). Moreover, it has been observed that microbial activity taken place in aged hydrocarbon is associated with the release of organic carbons, leading to etching and weathering of minerals, which may result in increasing porosity and increasing σ_b values. Regarding the increase in σ_b, ERT surveys have been used to distinguish areas with ongoing natural biodegradation of hydrocarbon contaminants (e.g., Atekwana et al., 2005; Atekwana et al., 2000). In addition to this, a decrease in electrical resistivity values has also been explained due to the development of microbial structures permitting fast current conduction (e.g., geobacterries, nanowires) (e.g., Revil et al., 2010). Taking those findings into account, studies have been conducted to assess microbial remediation by means of resistivity imaging (e.g., Chambers et al., 2010).

The relationship in Equation 2.1 has proven to be true in case of sediments where the grain surface conductivity (σ_S) does not contribute to the bulk electrical conduction. In order to account for this surface conduction, for example in presence of clays, small grain size minerals or conductive minerals (i.e., metallic minerals), Archie's model might be extended, assuming that electrolytic conduction (σ_{el}) and surface conduction (σ_S) add in parallel to the bulk formation electrical conductivity (Waxman and Smits, 1968),

$$\sigma_b = \sigma_{el} + \sigma_s = a\sigma_w\theta^m S^n + \sigma_s, \tag{2.2}$$

Based on its capability to measure low-frequency conduction and polarization properties, the spectral induced polarization (SIP) method has been proposed to gain information about surface conduction (σ_S) properties (e.g., Marshall and Madden, 1959; Waxman and Smits, 1968).

2.3.2. Induced Polarization

2.3.2.1. Measuring techniques

The induced polarization (IP) method is an extension of the electrical resistivity method. Based on the same four-electrode array, IP measurements can be performed in time-domain and/or in frequency-domain with multi-electrode systems, permitting the computation of images to assess the spatial distribution of low-frequency conduction and capacitive (polarization) properties of the subsurface. The IP method is also referred to as complex resistivity (CR), complex conductivity (CC), low frequency dielectric spectroscopy or electrical impedance tomography (EIT). A detailed review of the method is given in, for example, Sumner (1972); Ward (1990); Binley and Kemna (2005); and Kemna et al. (*submitted to Near Surface Geophysics*).

When performed in time-domain, IP measurements are given in terms of transfer resistances (R) and integral chargeability (m_i) values. The former is given by the ratio of measured voltage to current ratio during current injection; whereas the chargeability is defined as the ratio of voltage immediately after (secondary voltage, V_S), to the voltage immediately before (primary voltage, V_P) cessation of an infinitely long charging current (Seigel, 1959). However, for practical reasons, measuring devices (e.g., Syscal PRO from IRIS Instruments) typically use an integral measure of apparent chargeability (m_a), which can be written as (e.g., Binley and Kemna, 2005):

$$m_a = \frac{1}{t_2 - t_1} \frac{1}{V_p} \int_{t1}^{t_2} V(t) dt \tag{2.3}$$

Although traditional time-domain instruments measure a number of points on a decay curve, modern instruments digitize the signal at relatively high sampling rates and permit Fourier analysis in frequency-domain (e.g., Zimmermann et al., 2007; Zimmermann et al., 2008). In doing so, time-domain instruments can also provide a measure of IP in terms of complex resistivity, although the frequency range will be constrained by the sampling rate of the instrument (Binley and Kemna, 2005).

Measurements collected in the frequency-domain provide impedances comprised of magnitude (i.e., transfer resistances, R) and phase-angles (ϕ), by measuring the phase shift (hereafter referred to as phase) between periodic voltage and current signals. In addition, measurements can be collected at different frequencies to gain information about the frequency dependence of the subsurface electrical impedance, in the so-called spectral induced polarization (SIP) method. The inversion of measured impedances (magnitude and phase) computes images of complex resistivity (ρ^*), or complex conductivity (σ^*), which can be expressed in term of real (ρ') and imaginary (ρ'') components, or by means of the magnitude ($|\rho|$) and phase (ϕ) of the complex resistivity, as

$$\frac{1}{\sigma^*} = \rho^* = \rho' + \rho'' = |\rho| \exp(i\phi), \tag{2.4}$$

where i is the imaginary unit (i^2=-1), and

$$\phi = \arctan\left(\frac{\rho''}{\rho'}\right) = \arctan\left(-\frac{\sigma''}{\sigma'}\right), \tag{2.5}$$

$$|\rho^*| = \sqrt{\rho'^2 + \rho''^2}. \tag{2.6}$$

The real component (ρ') of the complex resistivity, (or of the complex conductivity), accounts for ohmic conduction and will be controlled by the same parameters as presented in Equation 2.1 (for "free" sediments, i.e., without clays, microbial cells and metallic minerals) and Equation 2.2; whereas the imaginary part accounts for charge transfer mechanisms (i.e., polarization) taking place at the surface of minerals in contact with pore-water (e.g., Lesmes and Frye, 2001; Lesmes and Morgan 2001). The mechanisms underlying the polarization response of sediments are not fully understood and conclusive interpretation of induced polarization data remains challenging, as does quantitative estimation of hydrologic and biogeochemical parameters derived from IP datasets (e.g., Binley and Kemna, 2005; Slater, 2007).

2.3.2.2. Cole – Cole model

In most of the cases, the SIP response exhibits a characteristic frequency, fc, where a maximum phase shift is observed. In such cases, due to its relatively simple parameterization, commonly the phenomenological Cole-Cole model (Cole and Cole, 1941) is used to describe the spectral behavior of the complex resistivity. Such model can be written in terms of complex resistivity as (Pelton et al., 1978):

$$\rho(\omega) = \rho_0 \left[1 + m\left(\frac{1}{1 + (i\omega\tau)^c}\right)\right], \tag{2.7}$$

where ω is the angular frequency. The direct-current resistivity ($\rho 0$) simulates unblocked pore paths, which allow parallel conduction through pure resistivity elements, m the chargeability (amplitude of polarization), c the frequency exponent (related to the shape of the spectrum, i.e., the degree of dispersion), and τ the time constant. The latter is related to the position of the maximum phase shift in the spectrum and is inversely proportional to the characteristic frequency (f_c), as described for example in Wong (1979):

$$\tau = \frac{1}{2\pi f_c} \tag{2.8}$$

Modifications of the model presented in Equation 2.7 have been proposed (for a review see Dias, 2000). For instance, if the frequency exponent c is equal to 1 in Equation 2.7, the resulting equation is known as the Debye model (Debye, 1929). Morgan and Lesmes (1994) have also proposed to use the superposition of n numbers of Debye terms, referred to as Debye decomposition, to better describe the shape of the spectra in SIP measurements which do not exhibit a symmetric shape about the critical frequency.

2.3.2.3. Mechanisms and applications

2.3.2.3.1. Electrode polarization

As described in Sumner (1976), the principal cause of IP in mineralized rocks is a current- induced electron transfer reaction between electrolyte ions and metallic luster minerals (i.e., electronic conductors), referred to as electrode polarization (e.g., Marshall and Madden, 1959; Pelton et al., 1978; Wong, 1979). Here the application of an external field (i.e., current) results in an electrochemical reaction such as the oxidation or reduction of some ion toward the mineral-electrolyte interface, leading to charge carried physically across the interface by electron transfer (Ward, 1980). As described in Revil and Cosenza (2010), the membrane polarization involves electromigration of redox ionic species (e.g., Fe(II)/Fe(III)) and the transfer of electrons between these electron donors/acceptors and abiotic or biotic electronic conductors. Hence, the chemical composition of the electrolyte might play a critical role in the magnitude of the phase response (e.g., Angoran and Madden, 1977; Merriam, 2007; Wong, 1979), leading to the concept of "active" ions, as such ions that facilitate charge transfer (redox reactions), whose availability is associated with higher phase response (e.g., dissolved Fe(II) in the Fe(II)/Fe(III) couple); however, the "active" role of the ions might be dependent on the excitation frequency, concentration and pH (Angoran and Madden, 1977; Wong, 1979).

Regarding the strong IP response associated with metallic minerals (i.e., metallic luster minerals), IP measurements have been used for the prospection of metallic and sulfide ore deposits (e.g., Marshall and Madden, 1959; Pelton et al., 1978; Seigel, 1959; Seigel et al., 1997; Spitzer and Chouteau, 2003; Sumner, 1976; Wong, 1979; Wong and Strangway, 1981). SIP measurements performed in artificial rocks containing pyrite (described in detail in Pelton et al., 1978) revealed that an increase in the volumetric content of metallic minerals was associated with an increase in chargeability (m) and time constant (τ); whereas an increase in grain size is related to an increase in τ but a decrease in m. Furthermore, the study of Pelton et al. (1978) also demonstrated that metallic minerals (copper, chalcopyrite, magnetite, pyrrhotite, pyrite, graphite and massive sulfides) occurring as discrete disseminated grains are associated with lower τ values than minerals distributed in veins; those minerals exhibited overall higher m and τ values. The work of Pelton et al. (1978) permitted to conclude that spectral parameters of the SIP response (m and τ) were not dependent on the mineral composition, with m exhibiting an ambiguous correlation with mineral size, but that τ was strongly dependent on the mineral length scale (i.e., grain size and texture) (Pelton et al., 1978). Besides these

findings, Wong (1979) proposed an electrochemical model to describe the polarization of metallic minerals, permitting the derivation of a relationship between the critical frequency observed in SIP data sets and the radius of metallic minerals (r). As proposed by Wong (1979), the relationship for small minerals is given by:

$$f_c \alpha \frac{\chi D}{r} \tag{2.9}$$

where D is the surface ionic diffusion coefficient and χ is related to the Debye screening length. For the characterization of larger minerals, Wong (1979) proposed the relationship

$$f_c \alpha \frac{D}{r^2} \tag{2.10}$$

However, the study does not define which size is small and large. Moreover, the model assumes that the minerals exhibit a spherical shape and a constant volume, leading to an overestimation of the volumetric content of metallic minerals with an elongated shape (Wong and Strangway, 1981).

Regarding the strong polarization effects observed in presence of metallic minerals, in the last decade several studies have evaluated the potential of SIP measurements for monitoring groundwater remediation techniques which involve the precipitation of metallic minerals (e.g., Williams et al., 2009; Williams et al., 2005), or based on the deployment of metallic particles, for example PRB (e.g., Slater and Binley, 2006). Experiments performed at the laboratory scale demonstrated that SIP signatures were sensitive to the precipitation of metallic minerals with a size of a few hundred nanometers (e.g., Williams et al., 2005), resulting from the stimulation of *Geobacter* species to remove U(VI) from groundwater. Further bio-stimulation experiments in the laboratory demonstrated that SIP measurements can also track spatio-temporal changes in the location of the mineralization (e.g., Ntarlagiannis et al., 2005a), as well as reversible reactions (i.e., dissolution of the minerals) accompanying changes in fluid chemistry and microbial transformations (e.g., Personna et al., 2008; Slater et al., 2007). At the field scale, anomalous IP signatures at different frequencies were found to correlate with the accumulation of iron sulfides following a bio-stimulation experiment (Williams et al., 2009). Further applications will be discussed in chapter 3, 4, 5 and 6 of this work.

Abiotic studies have also been performed at the laboratory scale in order to evaluate the potential of SIP measurements to monitor expected processes in PRB (e.g., Slater and Binley, 2006; Slater et al., 2006; Slater et al., 2005; Wu et al., 2005). Here, collected SIP measurements in sand mixtures containing zero-valent iron (Fe^0) particles (2.8 m^2/g and ~0.4 mm) demonstrated a strong lineal correlation between the surface area per unit

volume of Fe^0 and the imaginary component of the complex conductivity (σ') and with the computed chargeability values (m) after fitting Cole-Cole parameters. Moreover, in their study the authors reported variations in τ values with pH, which they correlated with changes in the surface (i.e., oxidation) of metallic particles (Slater et al., 2005). Further studies also demonstrated that non-metallic minerals (e.g., calcite) precipitating in column experiments may decrease the SIP signature of Fe^0, as they precipitate on the surface of the metallic particles, reducing their active surface area (Wu et al., 2008). Those studies suggest that SIP measurements can provide insight on the long-term performance of Fe^0–PRB, as they could gain information about loss of reactivity of the Fe^0–particles due to oxidation, as well as clogging effects as a consequence of the precipitation of calcite (Wu et al., 2009). At the field scale, complex resistivity images permitted to predict changes in PRB based on real measurements and numerical studies (Slater and Binley, 2006; Slater et al., 2010).

2.3.2.3.2. Electrochemical Polarization

IP measurements performed in sediments with negligible amounts of metallic minerals, have exhibited low but measurable polarization effects. Hence, several studies have been lately conducted in order to better understand the IP response in absence of metallic minerals. At low frequencies (< 100 Hz), the dominating mechanism enhancing the IP response is the polarization of the Stern layer coating the mineral surface. Initially proposed by Schwarz (1962) to describe the polarization of spherical colloids suspended in solution, this model has been used to explain the polarization of the mineral grains in contact with water. Here the fixed charge at the surface of the minerals is counterbalanced by charges in the so-called Stern layer coating the minerals surface and charges (at a larger distance) located in the diffuse layer. Under the effect of an external electrical field, the charges in the Stern and diffuse layer become polarized due to movement of the charges tangentially to mineral surface (e.g., Leroy et al., 2008; Lesmes and Frye, 2001). However, recent studies suggest that the grain-to-grain contacts in porous media may impede the polarization of the diffuse layer. Hence, the dominating polarization mechanism (at low frequencies) is given b y polarization of the Stern layer, with a frequency-dependence on the surface chemical properties of the porous media, i.e., surface area, surface charge density and surface ionic mobility (Lesmes and Frye, 2001). A detailed description of this mechanism is given in, for instances Leroy et al., 2008; Lesmes and Frye, 2001; Morgan and Lesmes, 1994; Revil and Florsch, 2010; Schwarz, 1962.

Two other processes need to be considered for the polarization of porous media: the Maxwell-Wagner and the membrane polarization. The Maxwell-Wagner polarization is caused by the accumulation of free charges at the interface of different phases, characterized by different dielectric constants, significant for measurements at high frequencies (> 100 Hz) (e.g., Leroy et al., 2008; Or and Wraith, 1999; Revil and Florsch, 2010; Vinegar and Waxman, 1984), while the membrane polarization is enhanced

particularly in the presence of clays, which act as ion-selective zones producing local concentration gradients under applied external voltage (for detailed description see, e.g., Cosenza et al., 2008; Ghorbani et al., 2008; Jougnot et al., 2010; Revil and Glover, 1998).

Initial laboratory studies revealed a linear negative correlation between the imaginar y component of the complex conductivity (σ'') and grain size (Slater and Lesmes, 2002b; Vanhala, 1997), as well as positive correlation between chargeability (measured in time-domain) and clay content (Slater and Lesmes, 2002a), while later measurements demonstrated a more robust correlation with the total area normalized to the pore volume (*Spor*) (Börner and Schön, 1995; Slater and Glaser, 2003; Weller et al., 2010) or with pore- size (Titov et al., 2002). As pointed out by Slater and Glaser (2003), the relationship between σ'' and representative grain size parameters depends on the distribution of the surface area across the grain size-distribution and the presence of clay minerals. Furthermore, a strong dependence of the SIP response on fluid chemistry (fluid electrical conductivity and pH) has been studied (Lesmes and Frye, 2001; Skold et al., 2011), as well as on saturation (e.g., Titov et al., 2004; Ulrich and Slater, 2004) and on temperature (Binley et al., 2010; Zisser et al., 2010a). Moreover, based on the analysis of the spectral response, a negative correlation has been identified between dominant pore-throat diameter and the critical frequency of the phase response for SIP measurements (Scott and Barker, 2003).

Taking into account the observed dependence of IP measurements on pore-scale texture, several studies have evaluated empirical relationships between the polarization (σ'') and hydraulic conductivity (K), as described in the works from Binley et al. (2005) and Slater (2007). Furthermore, considering that the length scales (i.e., grain size and texture) controlling the polarization relaxation time (τ) are intuitively the same as those controlling groundwater flow, analysis on the spectral response of the complex conductivity was performed on different laboratory studies revealing a strong lineal τ-k correlation (Binley et al., 2005; Kemna et al., 2005; Scott and Barker, 2003; Tong et al., 2005a; Tong et al., 2006; Tong et al., 2005b; Tong et al., 2004; Zisser et al., 2010b). Recently, a model has been proposed linking the main relaxation time (τ) and the hydraulic permeability (k), for sediments in a range of grain sizes (Revil and Florsch, 2010). This model was accurately fitting diverse data sets collected in the laboratory with bacteria- and metallic-free sediments (Revil and Florsch, 2010), demonstrating the possibility to extract quantitative hydraulic parameters from SIP data. Such model may be written as (Revil and Florsch, 2010):

$$k = \frac{D_j \tau_0}{4m^2 (F-1)^2 F} \tag{2.11}$$

where m is the cementation exponent (as in Equation 2.1), Dj is the diffusion coefficient of species j, τ_0 the main relaxation time and F the formation factor (related to porosity θ, as $F=\theta^{-m}$). However, to my knowledge, the described equation has not been

evaluated with field data. Regarding SIP imaging for field applications, (Slater and Glaser, 2003) used a relationship observed in laboratory measurements to determine clay content based on time-domain data collected at the field scale; (Kemna et al., 2004a) demonstrated that complex resistivit y imaging provides an improved lithological characterization and some insight in distribution of hydraulic parameters (e.g., k) based on single-frequency field data collected in frequency- domain. SIP measurements collected at the Krauthausen test site (Hördt et al., 2007; Hördt et al., 2009; Kemna et al., 2002) were also used to image the distribution of k values; however the authors reported a constant phase response for all acquisition frequencies (from 100 mHz to 1 kHz) hindering the possibility to compute the distribution of τ values. The inconsistency of k estimations based on single-frequency or constant phase response has been addressed in some studies (Binley et al., 2005; Revil and Florsch, 2010; Slater, 2007). Complex resistivity images were used in combination with GPR to gain information about the saturation and the distribution of structures in peat lands (Kettridge et al., 2008). Along with temperature sensors, complex resistivity images obtained for waterborne surveys (i.e., electrodes placed on the river stream), have been used to characterize discharge areas of a uranium contaminated aquifer into a river (Slater et al., 2010). Regarding the spectral capabilities of the method, measurements collected at the field scale and in core samples, have demonstrated the potential of SIP data to delineate crack and fractures, with the possibilit y to differentiate between open and filled fractures (Schmutz et al., 2011).

For the characterization of contaminants, a series of studies have been carried out in the laboratory with samples containing clay minerals and contaminated with petroleum hydrocarbons, especially VOCs (e.g., toluene). Such studies reported an increase in phase values (ϕ) for SIP measurements at low frequencies (< 10 Hz) (Olhoeft, 1985; Vanhala et al., 1992). Meanwhile, studies performed in sand and till samples with fresh oil revealed a decrease in the phase response (Börner et al., 1993; Vanhala, 1997); although changes were reported with continued oil maturation time (Vanhala, 1997). Regarding the spectral response of IP measurements, recent studies have reported an increase in time constant (τ) values for SIP measurements collected in samples with different saturation of non-aqueous phase liquids (e.g., octanol), concluding that changes in SIP responses are caused by pore obstruction by electrically non-conductive liquids and not by the electrochemical effects at the grain-electrolyte interface (Cassiani et al., 2009). Furthermore, an extension of the model proposed by (Revil and Florsch, 2010) (Equation 2.11) was fit to laboratory data collected in sand samples with different grain sizes contaminated with fresh-oil (Schmutz et al., 2010). Here, the authors modeled a decrease in the imaginary part of the complex conductivity (σ'') with increasing oil (i.e., non-aqueous phase) saturation. At the field scale, complex resistivity imaging was used to characterize the extent of contamination in an aquifer underlying a landfill (Aristodemou and Thomas-Betts, 2000; Dahlin et al., 2002), to delineate the presence of petroleum hydrocarbon due to fuel spills with single-frequency data collected with electrodes

placed in boreholes (Kemna et al., 2004a) and surface time-domain measurements (Sogade et al., 2006).

SIP measurements have revealed also an increase in σ'' and ϕ for samples collected from a BTEX contaminated site (Abdel Aal et al., 2006). However, the authors suggest the microbial colonization of mineral surfaces and their release of ions into solution as the mechanisms underlying the SIP response and not the changes in the mineral surface due to the weathering or etching, more related to changes in the σ' as described before. Furthermore, they conclude that the enhanced SIP response might occur due to pore constrictions as a consequence of ion-selective biological membranes (Abdel Aal et al., 2006). Several studies in the laboratory have demonstrated that accumulation of microbial cells (i.e., biofilms) may result in measurable SIP response (e.g., Abdel Aal et al., 2009; Abdel Aal et al., 2004; Abdel Aal et al., 2006; Davis et al., 2006; Ntarlagiannis et al., 2010; Ntarlagiannis et al., 2005b). Hence, SIP measurements can be used in the emerging discipline of biogeophysics to characterize microbial-related processes (Atekwana and Atekwana, 2010; Atekwana and Slater, 2009). At the field scale, time-domain measurements were used to monitor the remediation of a tar contaminated site by means of a PRB enhancing high rates of microbial activity (Doherty et al., 2010). Nevertheless measurable IP signatures at the field scale due to the accumulation of biofilms remain open to debate, particularly in presence of other materials with stronger polarization properties (Ntarlagiannis et al., 2010).

2.3.2.3.3. Electrical Imaging

Images of the distribution of the complex resistivity in the subsurface might be computed through the inversion of multi-electrode (also referred to as tomographic) data sets of electrical impedance, whether if the measurements were collected in the time-domain or in the frequency-domain. The aim of the inversion algorithm is to find a model that is consistent with the measured data, in this case the model is given by the distribution of complex conductivity and the data are given by the measurements of electrical impedances (e.g., Kemna, 2000). Methods for inverting IP data (i.e., electrical impedances) can also solve for the distribution of electrical resistivity and chargeability (e.g., Oldenburg and Li, 1994; 1999; Loke et al., 2006; Chambers et al., 2004), for data collected in time-domain or frequency-domain. A different approach consist in the inversion of the complex resistivity, either given by magnitude and phase (e.g., Kemna and Binley 1996; Ramirez et al., 1999; Kemna, 2000, among others), or in real and imaginary components (e.g., Zimmermann et al., 2008; Commer et al., 2011). For the complex inversion of time-domain data, it is necessary to convert the chargeability measurements to apparent phase-angles (i.e., to real and imaginary components of the electrical impedance) in order to perform the inversion. The conversion of chargeability values to phase-angle values might be performed based on a linear approximation (Siegel, 1959), as described in the fourth chapter of this study. Here the conversion of time-domain data into apparent phase values was calculated following the approach

described in Kemna et al. (1999); although the determination of an experimental factor has also provided a good approximation (e.g., Slater and Lesmes, 2002a; Slater and Binley, 2006). A complete description of the inversion procedures and of the tomographic approach for the complex resistivity can be found in Binley and Kemna (2005) and Kemna et al. (*submitted to Near Surface Geophysics*).

The increasing use of the IP method in emerging research areas (e.g., biogeophysics) has prompted the development of the IP imaging technique, leading to the improvement of the inversion techniques. Efforts have been applied in the development of 3D imaging codes for the IP method (e.g., Li and Oldenburg, 2000; Chambers et al., 2004; Commer et al., 2011). However, the long acquisition times required for the collection of SIP measurements (particularly for low frequencies < 1 Hz), justify the application of 2D surveys, at cost of the 3D spatial information, in order to gain information over a broad frequency bandwidth (as discussed in the chapter 4 and 6 of this work), as required by existing petrophysical models (Equations 2.9, 2.10, 2.11). Images of complex resistivity for 2D surveys have demonstrated to provide an improved lithological characterization (e.g., Kemna et al., 2004a; Kettridge et. al., 2008), to estimate hydraulical parameters at the field scale (e.g., Kemna, 2000; Slater and Glaser 2003; Hördt et al., 2007; 2009); to permit the characterization of contaminant plumes (e.g., Kemna and Binley, 1996; Kemna et al., 1997; 1999; 2004a; Slater et al., 2010; Vaudelet et al., 2011), and for the monitoring of remediation techniques (Slater and Binley, 2006; Williams et al., 2009). Further improvements in the inversion algorithm include the capability to use different spatial regularizations to the smoothness-constraint (e.g., Kemna, 2000; Blaschek et al., 2008), or with a temporal regularization for the inversion of time-lapse data sets (e.g., Johnson et al., 2010; Karaoulis et al., 2011), as described in the review by Kemna et al. (*submitted to Near Surface Geophysics*). However, the lack of reliable tomographic data sets, the difficulties and long acquisition times associated with the collection of SIP measurements at the field scale together with the difficulties regarding the interpretation of the polarization response, have slowed the development of the inversion algorithms for electrical impedance measurements in comparison with the development of the modeling techniques developed for the dc-resistivity method.

In this study, SIP images were computed with CRTomo, a smoothness-constraint inversion code by Kemna (2000). CRTomo permits to compute 2D images of the complex resistivity for data sets collected in a single-frequency; SIP data sets are inverted for each frequency independently. For completeness, a short introduction to the inversion algorithm is presented in the next chapter of this study, also with an evaluation of the forward modeling, for completeness. However, the reader is referred to the work of Kemna (2000) for a detailed description on the inversion procedure.

3. DATA ERROR QUANTIFICATION IN SPECTRAL INDUCED POLARIZATION IMAGING[1]

3.1. Abstract

Induced polarization (IP) imaging is being increasingly used in near-surface geophysical studies, particularly for hydrogeologic and environmental applications. However, the analysis of IP data error has received little attention, even though the importance of an adequate error parameterization has been demonstrated for electrical resistivity imaging. Based on the analysis of data sets measured in the frequency range from 1 Hz to 1 kHz, we proposed a model for the quantification of phase data errors in IP measurements. The analyzed data sets were collected on an experimental tank containing targets of different polarizability. Our study is based on the common practice that the discrepancy of measurements taken in normal and reciprocal configuration can be considered as a measure of data error. Statistical analysis of the discrepancies between normal and reciprocal measurements revealed that the phase error decreases with increasing resistance (i.e., signal strength). We proposed an inverse power-law model to quantify the phase error as a function of the measured resistances. We found that the adequate implementation of the proposed error model in an inversion scheme leads to improved IP imaging results in laboratory experiments. Application to a data set collected at the field-scale also demonstrated the superiority of the new model over previous assumptions.

3.2. Introduction

Induced polarization (IP) imaging has emerged as a promising method for hydrogeological and environmental studies. In recent years, several laboratory studies have demonstrated the capability of the IP method to gain valuable information about textural and hydraulic properties of the subsurface (e.g., Binley et al., 2005; Zisser et al, 2010). At the field scale, it has been demonstrated that IP imaging can lead to improved lithological characterization (e.g., Kemna et al., 2004; Hördt et al., 2009; Slater et al., 2010) and detection of contaminants (e.g., Kemna et al., 2004). It has also been used for the monitoring of geochemical and biogeochemical processes (e.g., Slater and Binley, 2006; Williams et al., 2009). This is due to the fact that IP measurements provide information not only about conduction (resistivity method), but also about the capacitive properties of the subsurface. Moreover, measurements collected at different frequencies (referred to as spectral induced polarization, SIP), might also provide information about geometrical properties of the pore space (e.g., Pelton et al., 1978; Wong, 1979; Binley et al., 2010; Revil and Florsch, 2010). However, applications of SIP imaging at the field scale are still rare because of the limitations and difficulties associated with data acquisition, and the lack of studies regarding the parameterization of data error in inversion schemes.

[1] Flores Orozco, A., Zimmermann, E., and Kemna, A. 2010. Data error quantification in spectral induced polarization imaging: Geophysics, 77(3), E227-E237.

Every measurement is subject to systematic and random errors. In the case of electrical methods, the former are commonly associated with problems during data acquisition such as poor galvanic contact, malfunction of the measuring device, and some sources of anthropogenic noise. There are particular effects that need to be considered as sources of systematic errors for SIP measurements: polarization of the electrodes used for current injection (Dahlin et al., 2002; LaBrecque and Daily, 2008), primarily for measurements at lower frequencies (< 10 Hz); and electromagnetic coupling (capacitive and inductive effects), which is more significant for measurements at higher frequencies (> 10 Hz), associated with the wires connecting the electrodes and the measuring device (e.g., Pelton et al., 1978). However, this study does not address systematic errors, as it is assumed that they need to be avoided or corrected before the inversion.

Random errors cannot be predicted as they arise primarily from fluctuations in the contact between the electrodes with the ground/air, and in the injected current and its pathways (e.g., Binley et al., 1995; LaBrecque et al, 1996; Slater et al., 2000). Previous studies have demonstrated that adequate estimation of random errors in tomographic data sets plays an important role regarding the quality of the resultant electrical images (e.g., Binley et al., 1995; LaBrecque et al., 1996). Even though the advantage of a proper error description in the inversion has been demonstrated for resistance data sets (e.g., Binley et al., 1995; LaBrecque et al., 1996), there have not yet been any studies investigating this issue for IP or SIP. So far, a constant error of the phase of the measured impedance has been assumed (Kemna, 2000), ignoring a possible dependence of the phase error on resistance (reflecting voltage signal strength for constant current) or the phase value itself.

The objective of this study is to improve SIP imaging by establishing an appropriate error model for the inversion of phase data based on a thorough analysis of tomographic impedance data sets measured in the laboratory under controlled conditions. Taking into account the fact that the numerical modeling of typical noise characteristics is practically impossible due to its complexity and the various possible sources, our analysis is based on performed (real) measurements and not on synthetic data.

The first section of the study addresses how data error is incorporated in the complex resistivity inversion scheme and which error models have been used so far for the description of resistance and phase errors. The second section presents the experimental setup and measurement scheme, a thorough analysis of the (spectral) raw data, a new phase error model, and the imaging results obtained. The third section shows the application of the proposed phase error model to single-frequency field data, followed by discussion and conclusions.

3.3. Data error treatment in complex resistivity imaging

3.3.1. Complex resistivity inversion scheme

The complex resistivity images presented in this work were computed using the smoothness-constraint inversion code by Kemna (2000). Based on a finite-element discretization, the code

calculates the distribution of complex resistivity, $\rho = |\rho| e^{i\phi}$ (with magnitude ($|\rho|$) and phase (ϕ), and $i = \sqrt{-1}$), in a 2D image plane from a given data set of transfer impedances Z_j ($j = 1, \ldots, n$; with n being the number of measurements) measured at some frequency f. The underlying forward model solves either the Helmholtz equation in the wavenumber domain for a 2.5D modeling problem, or the Poisson equation in real space for a purely 2D modeling problem.

The inversion algorithm iteratively minimizes an objective function composed of the measures of data misfit and first-order model roughness, with both terms being balanced by a regularization parameter. The iteration process is stopped when the RMS data-misfit value,

$$RMS = \sqrt{\frac{1}{n}\sum_{j=1}^{n}\frac{|d_j - f_j(\mathbf{m})|^2}{|\varepsilon_j|^2}} \tag{3.1}$$

reaches the value of one for the smoothest possible model. In equation 3.1, **m** represents the model vector (here log-transformed complex resistivity), $f_j(\mathbf{m})$ the operator of the forward model, d_j the j-th datum (here log-transformed complex impedance) with error ε_j. In the inversion algorithm, it is assumed that the data errors are uncorrelated and normally distributed. The complex data error ϕ_j can be considered as a confidence region ellipse in the complex plane around the data point d_j, expressed as

$$\varepsilon_j = s(\ln|Z_j|) + i\, s(\phi_j)\,, \tag{3.2}$$

where $s(\ln|Z_j|)$ and $s(\phi_j)$ represent the standard deviations of the log magnitude ($\ln|Z_j|$) and phase (ϕ_j), respectively, of the impedance Z_j (note that $d_j = \ln Z_j = \ln|Z_j| + i\phi_j$). In the complex error, $s(\ln|Z_j|)$ typically dominates $s(\phi_j)$ and thus controls the inversion behavior (and stopping criterion) of the complex-valued inversion scheme. In order to take the phase error into account quantitatively, additional, real-valued inversion iterations are run only for the phase data, once the complex inversion has reached an RMS of one. The iterative inversion process for the phase is stopped when the corresponding RMS (for the phase inversions) value,

$$RMS_{\text{phase}} = \sqrt{\frac{1}{n}\sum_{j=1}^{n}\left(\frac{\text{Im}(d_j) - \text{Im}(f_j(\mathbf{m}))}{s(\phi_j)}\right)^2}\,, \tag{3.3}$$

reaches the value of one for the smoothest possible model. For further details on the inversion algorithm, as well as the underlying finite-element forward modeling, we refer to Kemna (2000).

3.3.2. Parameterization of resistance error

The final result of the inversion strongly depends on the data error and its parameterization. However, it is practically impossible to know the exact variance and distribution of the random errors in the data. It is therefore necessary to make use of approximations to characterize the data error for the inversion (LaBrecque et al., 1996).

LaBrecque et al. (1996) proposed a linear relationship between the measured resistances (denoted as $R = |Z|$ in the following) and their associated error, $s(R)$. This model can be written (e.g., Slater et al., 2000) as

$$s(R) = a + bR, \tag{3.4}$$

where a is the absolute resistance error at small resistance values ($R \to 0: \; s(R) = a$), and b defines the relative (percentage) resistance error for larger resistance values ($R \to \infty: \; s(R) = bR$). The parameters a and b can be estimated from the standard deviation of the difference (ΔR) between normal (R_n) and reciprocal (R_r) measurements in the data set (LaBrecque et al., 1996). Reciprocal measurements are those collected when current and potential dipoles are interchanged from the "normal" configuration.

3.3.3. Parameterization of phase error

In contrast to resistivity imaging, only a few studies have dealt with the analysis of the error present in impedance phase measurements. In the first reported work (Ramirez et al., 1999), the authors based their study on the analysis of reciprocal measurements, analogous to LaBrecque et al. (1996). They performed measurements in a tank with different targets and presented plots of the calculated absolute value of the discrepancy in the phase ($|\Delta\phi|$), given by the difference between normal (ϕ_n) and reciprocal (ϕ_r) phase measurements, against the corresponding average value. Based on the observed distribution of the phase discrepancy, they defined a constant value to describe the error in the phase data, which encompasses the majority of the measurements. In their study, the authors also reported a noticeable increase in the phase discrepancy for data collected at high frequencies, indicating a frequency dependence of the phase error.

The second approach, by Slater and Binley (2006), is based on a statistical analysis of the difference between normal and reciprocal measurements ($\Delta\phi$, not $|\Delta\phi|$). Slater and Binley (2006) calculated the standard deviation of the entire data set and used this value to define a constant phase error ($s(\phi)$) in the inversion. The images presented show negligible artifacts and a good correlation with the expected models. However, the data in their study were originally collected in the time domain and the measured chargeabilities were, as a first approximation, linearly converted to phase values for the inversion in the frequency domain. Therefore the presented plots of normal-reciprocal discrepancies in the IP data may only provide limited insight into the error characteristics of true phase measurements.

3.4. Analysis of spectral data from a laboratory experiment

3.4.1. Experimental setup and measurement scheme

In order to study the characteristics of random error in SIP phase measurements, we collected several tomographic data sets on a physical tank model. The Plexiglas tank has a length of 1 m, a width of 0.5 m, and a height of 0.02 m, and was uniformly filled with well-characterized quartz sand and tap water (as saturating electrolyte). Two filters made of porous polyethylene (with a pore diameter of approximately 200 μm) were installed (0.1 m away from the edges, as depicted in Figure 3.1) in order to allow dynamic flow experiments in the tank with a homogeneous flow field. However, the measurements presented here were collected under static (no-flow) conditions.

Altogether 80 pin electrodes, made of copper with a diameter of 4 mm, were installed along the long walls of the tank (40 on each side) at a constant spacing of 2.5 cm (Figure 3.1). The electrodes were mounted into the walls of the tank as depicted in Figure 3.1 to reduce the contact of the electrodes inside the tank and to fulfill the assumption of point electrodes as required in the inversion. Taking into account the geometry of our electrodes, we estimated an error below 5 % for the "worst" case of injecting current at a single electrode and measuring the potential magnitude at an adjacent electrode (note that there is no such error for the phase of the potential), based on the analytical solution provided in Militzer and Weber (1985). This systematic error rapidly decreases for larger distances from the current electrode.

Three different targets were placed inside the saturated-sand background in order to build a model with some degree of complexity. Moreover, different materials were selected as targets to enhance different polarization mechanisms, i.e., massive copper associated with electrode polarization at the metal-electrolyte interface and pure clay associated with so-called membrane polarization at the clay mineral-electrolyte interface. Generally, electrode polarization has a larger magnitude than membrane polarization (e.g., Pelton et al., 1978; Slater et al., 2006). More explicitly, the targets were: 1) a 0.1 m diameter copper cylinder, 2) a 0.1 m diameter clay cylinder, and 3) a 0.075 m thick clay "layer".

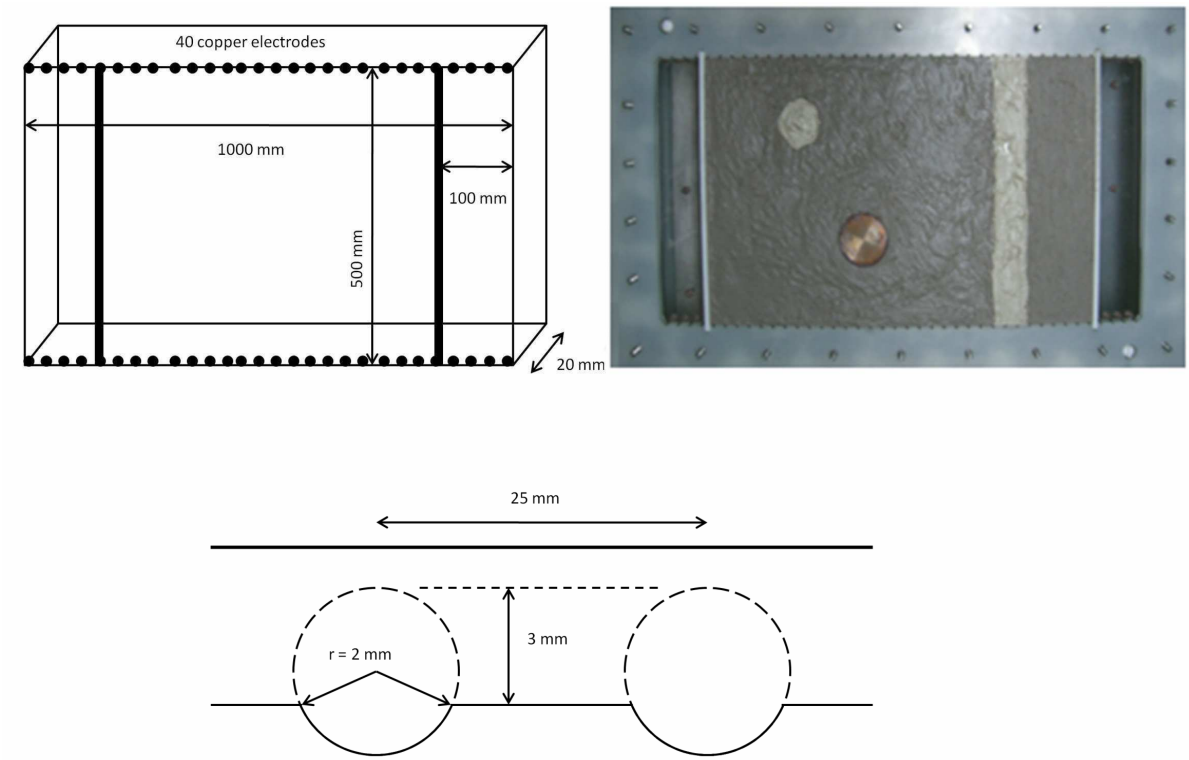

Figure 3.1: Top left: Schematic representation of the 2D tank with 80 electrodes. Top right: Photo of the tank with the targets (anomalies) inside: two cylindrical bodies (10 cm radius) made of clay and copper, and a 5 cm clay "layer". Quartz sand was used to fill the rest of the tank between the filters, and tap water was used as electrolyte. Bottom: Schematic representation of the electrodes (dashed circles) and their emplacement in the insulating walls of the tank (represented by solid lines), in order to reduce the effective width of the electrodes (solid arcs). Less than one third of the total electrode area was used to perform measurements, validating the ideal-line-electrode assumption in the numerical modeling.

Our laboratory study was designed as a 2D experiment in order to better evaluate the imaging result, to simplify the measuring protocols and to reduce data acquisition times (critical for SIP measurements at low frequencies). However, the presented data analysis approach is analogously applicable to 3D data sets. In order to satisfy the assumption of a 2D case, we avoided changes in the third dimension (the height of the tank). It was achieved in the following way: 1) the tank contained targets, filters and filling materials that extended uniformly along the tank height; 2) current injection and measurements of electrical potential were performed on line electrodes extending along the entire height of the tank, afterwards the collected resistance values of the electrical impedance were normalized by this height. From symmetry, the deployment of line electrodes results in electrical fields that vary only in two dimensions, and therefore can be modeled with our 2D inversion approach. To illustrate the accuracy of the 2D forward modeling underlying the inversion algorithm for the given measurement geometry, Figure 3.2 shows a comparison between the numerical and analytical solution for an exemplary injection dipole assuming a constant resistivity inside the tank. The potential distribution reflects the no-flow boundary conditions imposed everywhere on the tank boundary. In the analytical solution, the no-flow conditions at the four edges were accounted for by computing the superposed potential for 800 fictitious "mirror" sources (see for example Weidelt and Weller, 1997, for the computation of the analytical solution for a point source on the boundary of a confined body).

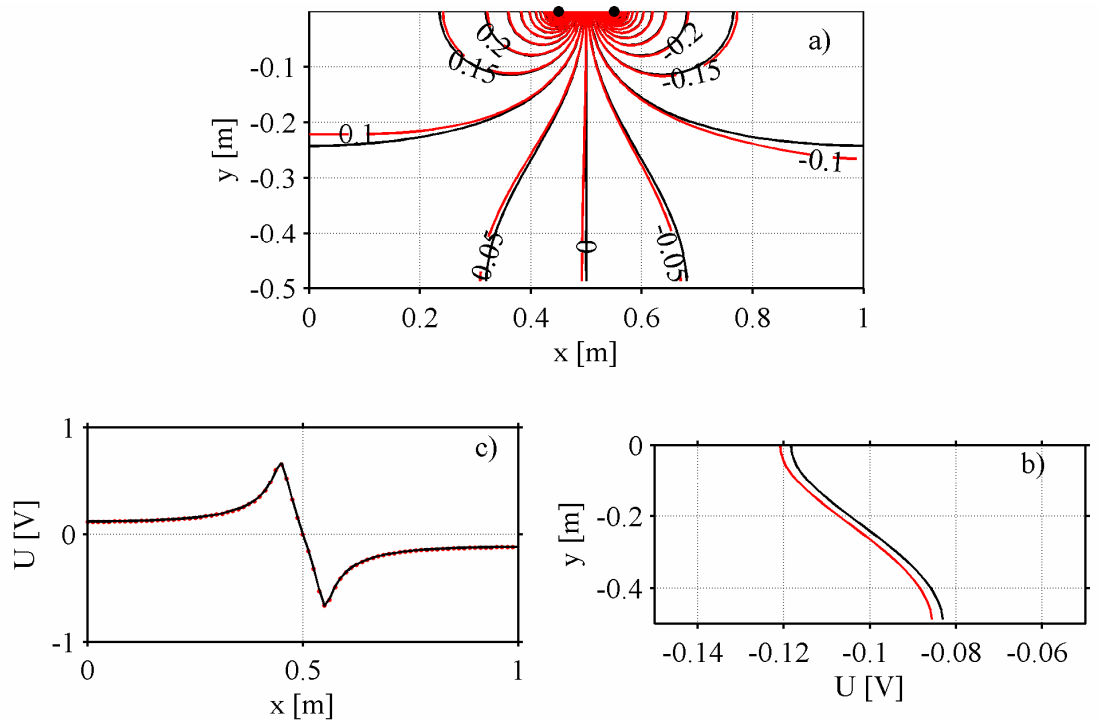

Figure 3.2: 2D modeled numerical (red lines) and analytical (black lines) distribution of the electrical potential inside the tank due to an electric current dipole (indicated by the solid circles). The potential (*U*) values of plotted equipotential lines are given in V, for a current of 1 A and a background resistivity of 1 Ωm (Fig. 2a). The potential distributions along the right (x = 1 m) and close to the top (y = -0.125 m) boundaries are also presented (Figures. 3.2b and 3.2c, respectively). The analytical solution was computed by superposition of the potential of 800 fictitious "mirror" sources to account for the no-flow boundary conditions along the four edges of the tank.

An impedance spectrometer with high phase accuracy, described in detail in Zimmermann et al. (2008), was used to perform the measurements. The equipment has 32 channels for current injection and 92 channels to collect electrical impedance data in the frequency domain. To avoid cross-talking between the cables and to reduce electromagnetic coupling, coaxial cables were used to connect the electrodes in the tank with the equipment. The electronic component (to inject the current or to perform potential measurements) was placed at the end of each cable, connected directly to the electrodes (1 cm distance between electrode and electronic component). The tank and the measuring equipment were separated from the other electrical devices to avoid electromagnetic contamination of the data.

The resolution of the imaging results depends on the measurement configuration. This issue has been addressed in numerous studies for both synthetic and field data (e.g., Xu and Noel, 1993; Bing and Greenhalgh, 2000; Slater et al., 2000; Stummer et al., 2004). In the present study, two different measuring configurations were employed. In the first configuration, (hereafter referred to as cross dipoles), the current dipole was placed on one side of the tank and the voltage dipole on the other (as depicted in Figure 3.3). The measurements were performed using standard skip-1 ("1" denoting the number of electrodes that are "skipped" by each dipole) and skip-2 dipole-dipole schemes. This resulted in a total of 2600 measurements (1300 normal, 1300 reciprocal).

In the second configuration (hereafter referred to as opposite dipoles), the current and voltage dipoles were opposite each other in the tank, i.e., current source (C+) and positive potential (P+) were located on one side, and current sink (C-) and negative potential (P-) on the other, as depicted in Figure 3.3. The total number of measurements here was 950 (475 normal, 475 reciprocal).

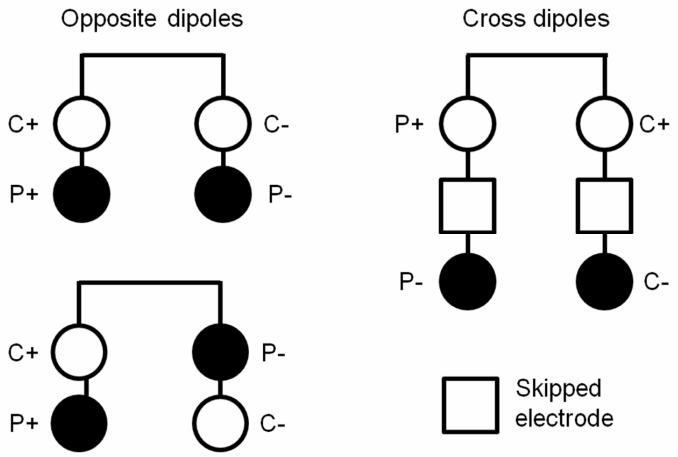

Figure 3.3: Measurement configurations used to collect data for the 2D tank experiment. Left: "Opposite dipoles" configuration. Right: "Cross dipoles" configuration. Current electrodes (C+, C-) are indicated by open circles and potential electrodes (P+, P-) by solid circles.

The selected configurations minimized the risk of systematic errors due to polarization of the electrodes and provided a wide range in the measured resistance values, corresponding to a wide range in the signal-to-noise ratio, which allows the proper investigation of the relationship between phase error and resistance value.

In addition to the collection of normal and reciprocal data, i.e., exchanging C+ with P+ and C- with P-, the measurement system employed repeats each measurement with swapped current injection polarity, i.e., internally exchanges C+ with C-. Zimmermann et al. (2008) showed that averaging the corresponding measurements eliminates the negative effect of parasitic currents. Data were collected at frequencies between 1 Hz and 1 kHz. At lower frequencies, overall data acquisition time becomes relatively long; while at higher frequencies systematic errors due to electromagnetic coupling start to occur (Zimmermann et al., 2008).

3.4.2. Data analysis and new phase error model

As in previous studies (Binley et al., 1995; LaBrecque et al., 1996; Slater and Binley, 2006), we analyzed the discrepancy between normal and reciprocal measurements, assuming that this represents a practical measure of data error. The plots of the normal-reciprocal discrepancies in the resistance (ΔR) against the corresponding resistance value (R) (Figure 3.4, left column) behave as described by the model proposed by LaBrecque et al. (1996) (equation 3.4); note that in Figure 3.4, ΔR is plotted against log$R$ to better resolve the distribution of data points). No significant change is observed in the resistance behavior for the different frequencies (Figure 3.4, left column). For the phase measurements, the data

collected with the opposite dipoles configurations show a high signal-to-noise ratio, characterized by a low value in the normal-reciprocal discrepancy of the phase. In contrast, the measurements performed with the cross dipoles configuration exhibit larger phase values and larger normal-reciprocal phase discrepancies (Figure 3.4, middle and right-hand columns).

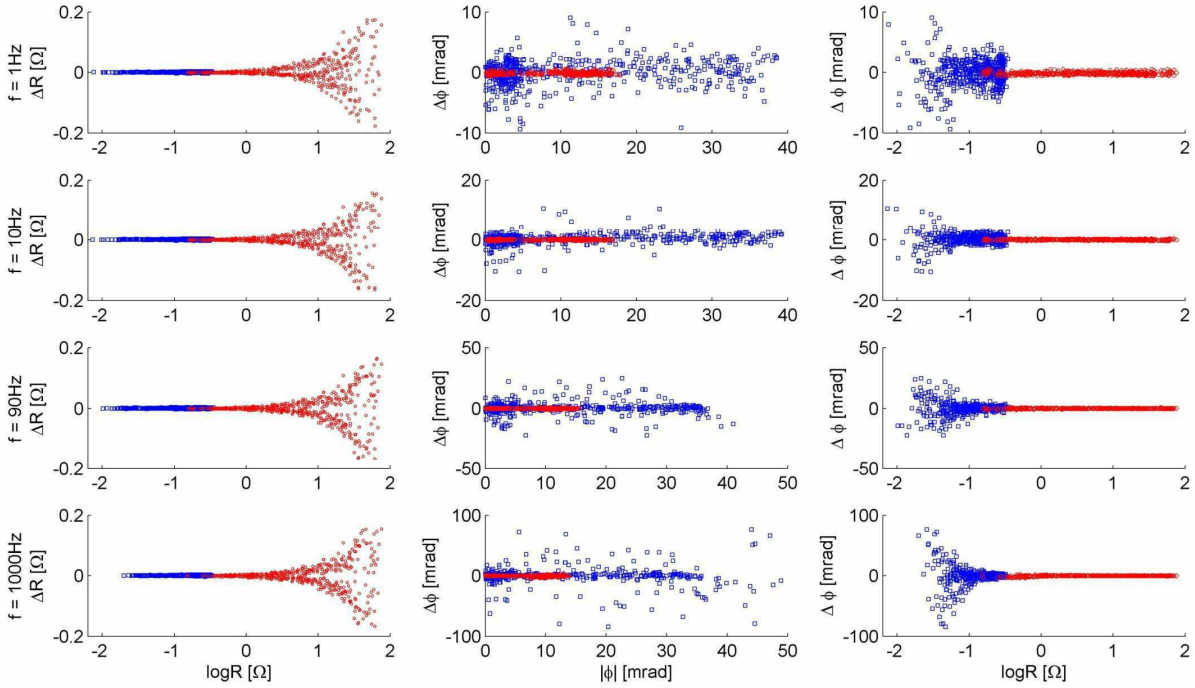

Figure 3.4: Raw tank data collected at different frequencies for both measurement schemes (blue squares: opposite dipoles; red circles: cross dipoles). Left-hand column: Normal-reciprocal resistance discrepancy versus log resistance. Middle column: Normal-reciprocal phase discrepancy versus absolute phase. Right-hand column: Normal-reciprocal phase discrepancy versus log resistance.

Our first approach to describe the error in the phase measurements was based on a relationship between the normal-reciprocal phase discrepancy ($\Delta\phi$) and the absolute value of the phase ($|\phi|$), similar to the study of Ramirez et al. (1999). However, as shown in the middle column of Figure 3.4, the plots exhibit a scattered distribution. Therefore it does not seem appropriate to characterize the phase discrepancy as a function of the phase value. Also the absolute phase discrepancy ($|\Delta\phi|$) as a function of the absolute phase value was studied with no better results (plots not shown).

Given the expected correlation between resistance and signal strength, and signal strength and phase error, we then analyzed the distribution of the phase discrepancy against the corresponding resistance value. Here, a systematic trend is noticeable (Figure 3.4, right-hand column): higher phase discrepancies are associated with lower resistances and vice versa. If only the phase data recorded at high resistance values were considered, the error for the phase could be described fairly well by a constant value (Figure 3.4, right column), in accordance with previous approaches (Kemna, 2000; Slater and Binley, 2006). However, rejecting the data with low resistance values would reduce the data set by more than 65 % leading to a loss of resolution of the inverted phase image. Therefore, and in order to account for the large

dynamics in the resistance data, it is reasonable to consider the error in the phase measurements as a function of resistance.

For SIP measurements, it is essential to take into consideration the distribution of the phase discrepancies at different frequencies. Here, the plots of the phase discrepancy as a function of resistance display a consistent behavior for all frequencies, as shown in Figure 3.4. Based on the observed distribution of the phase discrepancies, we propose an inverse power-law relationship between the error in the phase ($s(\phi)$) and the corresponding resistance (R):

$$s(\phi) = a\, R^{b}\ , \tag{3.5}$$

with $b < 0$. For $b \to 0$, the proposed model reduces to the constant-phase error model employed in previous studies (Kemna, 2000; Slater and Binley, 2006).

In order to calculate the a and b parameters of the phase error model in equation 3.5, as well as the a and b parameters of the resistance error model in equation 3.4, we performed a so-called bin analysis. This technique was used by Koestel et al. (2008) to describe the error in ERT data sets. The procedure is based on the partition of the data set into a number of bins with respect to the resistance value. Each bin contains the normal-reciprocal phase and resistance discrepancies, respectively, of those data whose resistances fall into the resistance range of the bin. Once the data are sorted in these bins, the standard deviation of the corresponding discrepancies is calculated. Finally, the assumed error model is fitted to the standard deviations of the different bins as a function of the corresponding mean resistance value. The obtained parameters a and b are then used to describe the phase and resistance errors, respectively, according to the assumed model, in the inversion. This procedure was applied here for each of the data sets collected at the different frequencies.

The bin analysis is based on the assumption that the discrepancy values contained in each bin obey a normal distribution, so that they can be described by its standard deviation. In order to prove whether this assumption is justified we plotted the histograms of the resistance and phase discrepancy values for selected bins, based on different total numbers of bins. Examples of histograms for a selected bin (in this case the fourth bin) for different numbers of bins are shown in Figure 3.5, for different measurement frequencies. It is obvious that the distribution of data points depends on the number of bins defined in the analysis. Sampling with a high number of bins (here 42) leads to gaps in the histograms, due to the relatively small number of data points in the individual bins or even empty bins, which no longer obey a normal distribution. Sampling with a low number of bins (here 8) no longer follows a Gaussian-like behavior and is also insufficient to capture the dynamics in the error.

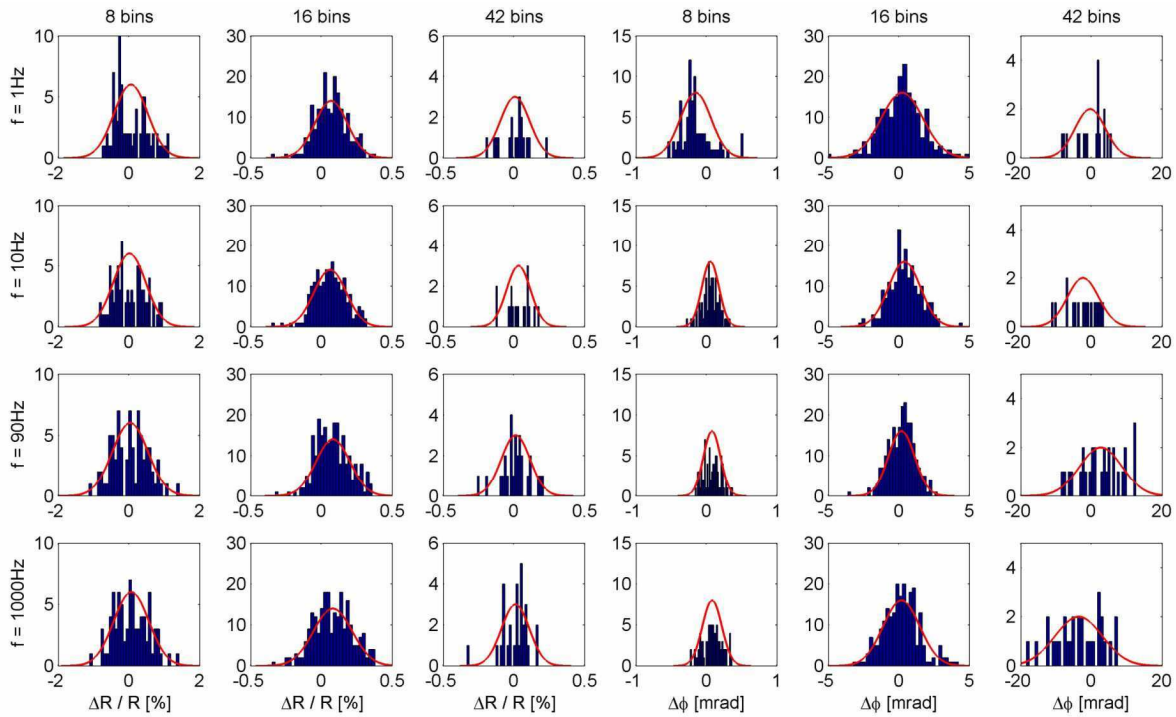

Figure 3.5: Histograms of the normal-reciprocal discrepancies of the resistance and phase tank data in the 4th bin based on different numbers of bins used in the analysis (8, 16, and 42 bins).

Therefore, it is important to select an adequate number of bins for the given number of measurements and range of resistances. To illustrate this issue, we plotted the calculated phase error model (equation 3.5) for different numbers of bins (Figure 3.6). Here we see that at low frequencies, the deviations between the obtained curves are generally relatively small. Larger deviations occur for low resistances and higher frequencies, the latter reflecting the increase of the normal-reciprocal phase discrepancies with frequency (cf. Figure 3.4). However, the error models for a moderate number of bins capture the mean behavior of the curves for all analyzed frequencies, demonstrating the robustness of the approach. Importantly, the phase error model differs significantly from the constant-phase error model ("single-bin" approach) according to Slater and Binley (2006).

For the results presented here, the bin analysis was performed using equally sized bins distributed in a logarithm logarithmic resistance scale. This sampling provided a fairly even distribution of data points over the bins. In the following, 16 bins were used for the analysis. This is the maximum number of bins for which each bin still contains at least 2 % of the total number of measurements.

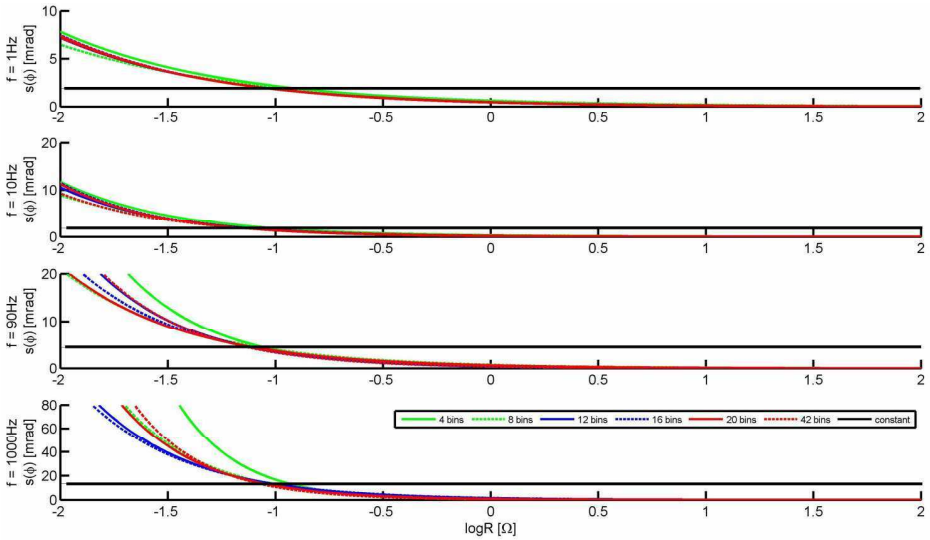

Figure 3.6: Calculated phase error models according to equation 3.5 for the tank data using different numbers of bins in the underlying analysis. For comparison, the constant-phase error model based on a single-bin analysis according to Slater and Binley (2006) is shown.

3.5. Imaging results

In this section, we present the imaging results obtained with the error models in equations 3.4 and 3.5 for the measurements collected in the tank. Figure 3.7 shows the corresponding resistance and phase error models computed for the data sets at different frequencies, in comparison with the models obtained from the single-bin approach by Slater and Binley (2006).

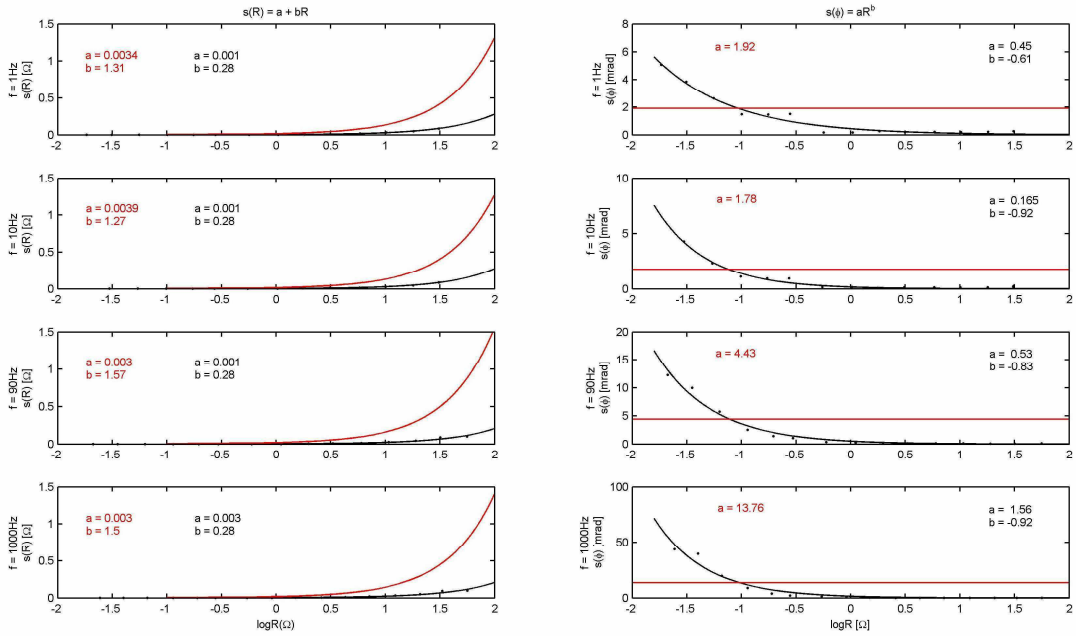

Figure 3.7: Resistance (left) and phase (right) error models for the tank data at different measurement frequencies based on a multi-bin analysis (black curves) and the single-bin approach by Slater and Binley (2006) (red curves). The black dots indicate the obtained standard deviations of the normal-reciprocal data discrepancies in the individual bins. Also shown are the corresponding values of the error model parameters *a* and *b* (for resistance, *a* in Ω and *b* in %; for phase, *a* in mrad and *b* value for *R* in Ω).

For the inversion we used a regular grid of square elements. The size of the elements was given by half of the distance between adjacent electrodes (1.25 cm). Images were also calculated with error parameters determined according to the approach of Slater and Binley (2006) and are shown for comparison. The resistivity magnitude image obtained after the inversion of the 1 Hz tank data is shown in Figure 3.8. It does not make any noticeable difference whether the error parameters are defined based on a single- or a multi-bin analysis, although the parameter values are different (see Figure 3.7). In the image, the lowest resistivity values occur in the areas beyond the filters in the tank, where only tap water is present (resistivity below 15 Ωm); while the highest resistivity values are found in the area between the filters, where the quartz sand is located (resistivity above 30 Ωm). The three targets as well as the filters are reasonably recovered in position and extension (cf. Figure 3.1). Minor artifacts can be identified in the area close to the filter on the left, but these are probably due to air bubbles present during data acquisition. We note that the resistivity images obtained for other measurement frequencies are effectively the same and are thus not shown.

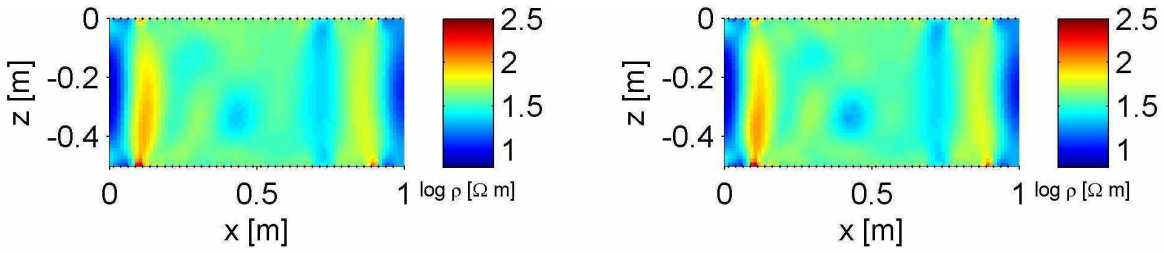

Figure 3.8: Resistivity magnitude image inverted from the 1 Hz tank data using the error model in equation 3.4 with parameters based on the Slater and Binley (2006) approach (left) and a multi-bin analysis according to Koestel et al. (2008) (right).

Figure 3.9 shows the images obtained from the inversion of the phase data at different frequencies. With both error approaches, the copper target is reasonably well recovered (except for the highest frequency) as a high-polarizable anomaly (up to 100 mrad) at the correct location. Below 1 kHz, the phase images calculated with the proposed phase error model clearly show fewer artifacts than those obtained with the constant-phase error model (suggesting an over-fitting of the data for the latter). At 1 kHz, the constant-phase error model yields a very smooth image where no anomalies are visible at all (suggesting an under-fitting of the data), while the new error model produces an image where the target can still be located. The clay targets, on the other hand, are not visible at all in the images based on the constant-phase error description, while at least the "clay layer" target is indicated for the higher frequencies towards the boundaries of the images obtained with the proposed phase error model. However, obviously the clay targets are difficult to detect, because their response is much weaker than that of the copper target and they are hence masked in the imaging. The background material in the tank (sand saturated with tap water) exhibits low polarizability (few milliradians) as expected.

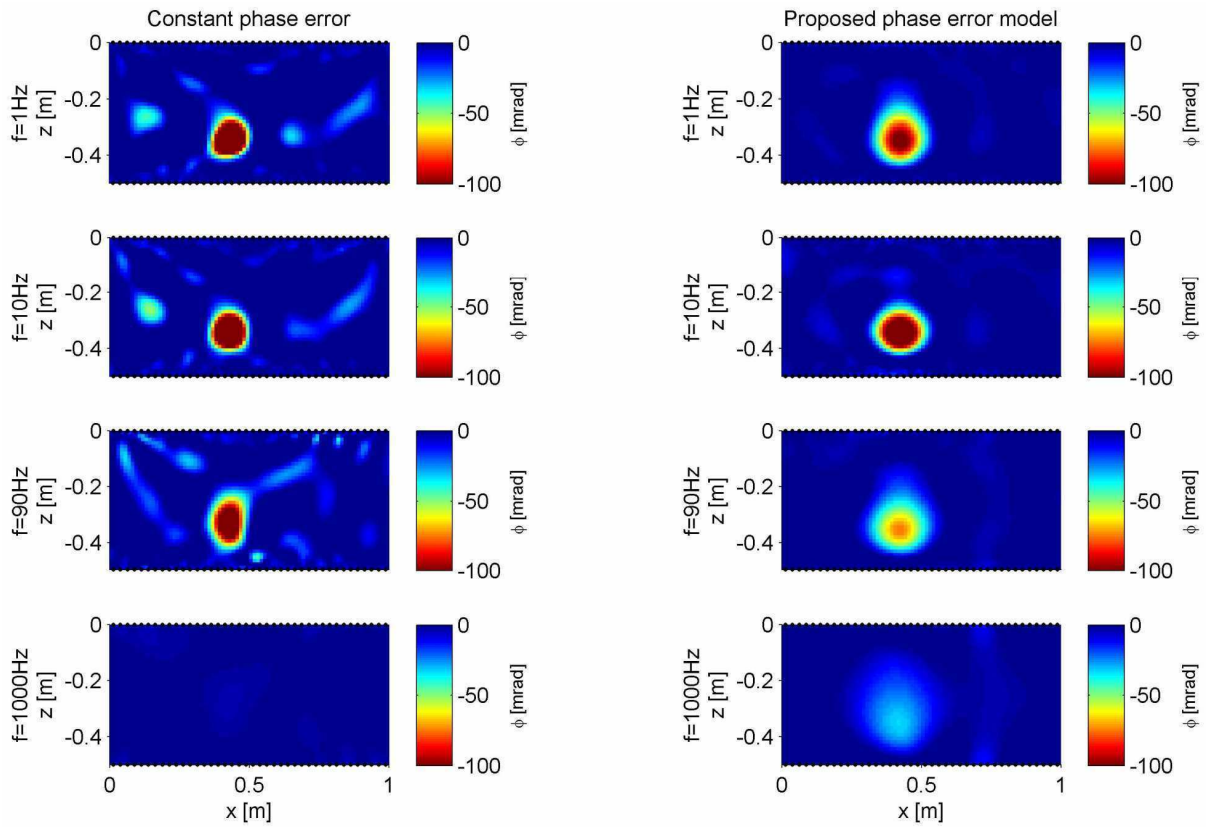

Figure 3.9: Resistivity phase images inverted from the tank data at different measurement frequencies using (left-hand column) the constant-phase error model according to Slater and Binley (2006) and (right-hand column) the proposed error model in equation 3.5 with parameters based on a multi-bin analysis.

To better examine the imaging results in terms of the recovered frequency dependence, pixel values were picked from the phase images at the different frequencies at the locations of the polarizable copper target and the "clay layer" target (Figure 3.10). For both pixels (targets), a systematic spectral behavior is observed, in particular for the spectra based on the proposed phase error model. In the frequency range considered, the reconstructed phase values for the copper target decrease continuously with increasing measuring frequency using the new phase error model, while the values remain relatively constant up to approximately 200 Hz and then decrease steeply with increasing frequency for the constant-phase error model. For the clay target, a spectrum continuously increasing with frequency is obtained with the new error model, while the constant-phase error model produces a spectrum with a phase maximum around 100 Hz. Although the true spectral signature of the targets is not known, with the constant-phase error model spectral responses are recovered which contradict expectations – this is not the case for the results obtained with the proposed error model. Copper in an electrolyte is known to produce a typical Cole-Cole phase response (e.g., Kemna et al., 2000), which obviously does not correspond to the observed flat and then abruptly decreasing phase response using the constant-phase error model. Clay is expected to show a response with increasing phase values up to the kHz range (e.g., Slater et al., 2006), as actually obtained with the new error model, but not consistent with the result using a constant-phase error model. These outcomes clearly demonstrate the sensitivity of imaged spectral characteristics with respect to the phase error description employed in the inversion, and they suggest that the proposed phase error model produces more reliable results.

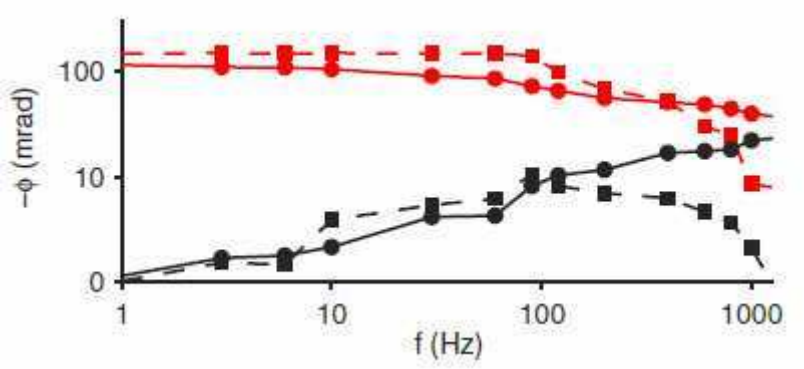

Figure 3.10: Spectral response for selected pixels of the inverted phase images of the tank model (see Figure 3.8) based on the constant-phase error model (squares, dashed curves) and the proposed phase error model (solid circles and solid lines). Selected pixels correspond to the copper target (red) and the "clay layer" target (black).

3.6. Application to single-frequency field data

To validate our approach in a field-scale application, we reprocessed cross-borehole impedance data that were collected at the hydrological test site at Krauthausen, Germany (Kemna et al., 2004b), which is operated by Forschungszentrum Jülich. Several studies have been performed at the site, including electrical surveys, and its hydrogeological characteristics are well known (see Kemna et al., 2002; Hördt et al., 2007; Tillmann et al., 2008; Müller et al., 2010).

3.6.1. Setup

Briefly, the area is defined by a 9 m thick aquifer, the basement of which is located at an approximate depth of 11 m. The aquifer is characterized by layers of gravel and sand corresponding to fluvial Rur sediments, overlain by a loess layer. For the impedance measurements, a total of five boreholes, defining a section of 27.5 m in length, were equipped with copper electrodes. Each borehole contains 13 electrodes between 3 and 9.5 m below ground surface (bgs), with an electrode separation of 0.5 m. Impedance magnitude and phase data were collected with the RESECS instrument by GeoServe at a frequency of 0.125 Hz. Measurements were performed between adjacent wells, using a skip 2 "cross dipoles" measurement protocol. Consistent with the tank measurements, data were collected in both normal and reciprocal configurations, resulting – after rejection of obvious outliers – in a total of 706 magnitude and phase readings for the subsequent error analysis and inversion.

3.6.2. Results

The analysis of the field data revealed qualitatively the same distribution of normal-reciprocal discrepancies as a function of resistance as found for the laboratory data (Figure 3.11): a linear increase of the discrepancy in the resistance with resistance value, and an inverse power-law relationship between discrepancy in the phase and resistance value. Like the laboratory data, the field data were inverted using the resistance error model by LaBrecque et al. (1996), with parameters determined from the two different (single- and multi-bin) approaches and using the two different (constant-phase and power-law) error models for the phase. However, considering the smaller range of resistance values and the smaller number of

measurements compared to the laboratory data sets, the multi-bin analysis was based on only six bins to determine the *a* and *b* parameters of the respective error models.

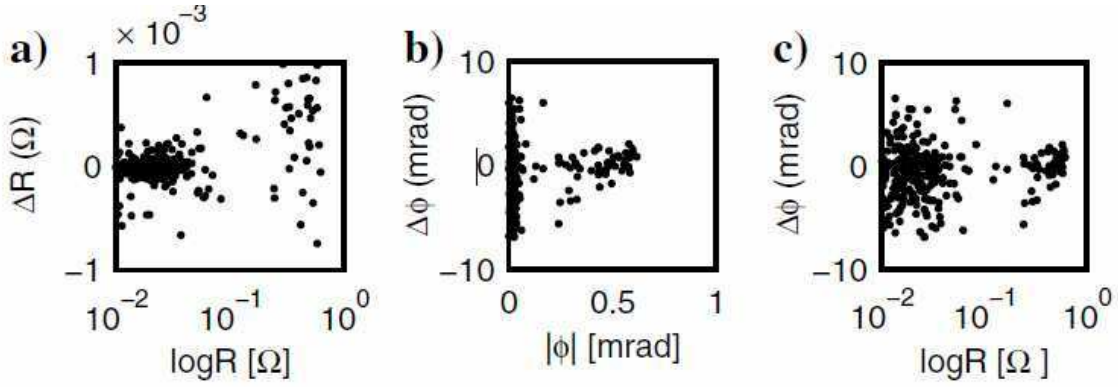

Figure 3.11: Raw field data collected at 0.125 Hz. Left: Normal-reciprocal resistance discrepancy versus log resistance. Middle: Normal-reciprocal phase discrepancy versus absolute phase. Right: Normal-reciprocal phase discrepancy versus log resistance.

The obtained image of resistivity magnitude is again effectively the same for both methods of choosing the parameters of the error model, and hence only the result based on the single-bin analysis (a = 1 Ωm and b = 1.2 %) is shown (Figure 3.12). The image reflects well the known geological situation at the site. It exhibits a unit characterized by relatively low resistivity values (around 50 Ωm) located between 4 m and 6 m bgs, which is embedded in a unit with moderate resistivity values (around 100 Ωm) extending down to 8 m depth. These units coincide with the known series of middle gravel, middle sand, and fine gravel layers. The high-resistive feature (around 250 Ωm) at the bottom of the image plane delineates a gravel unit at approximately 9 m depth, on top of interbedded strata of sand, gravel, and clay characterized by even lower resistivity values.

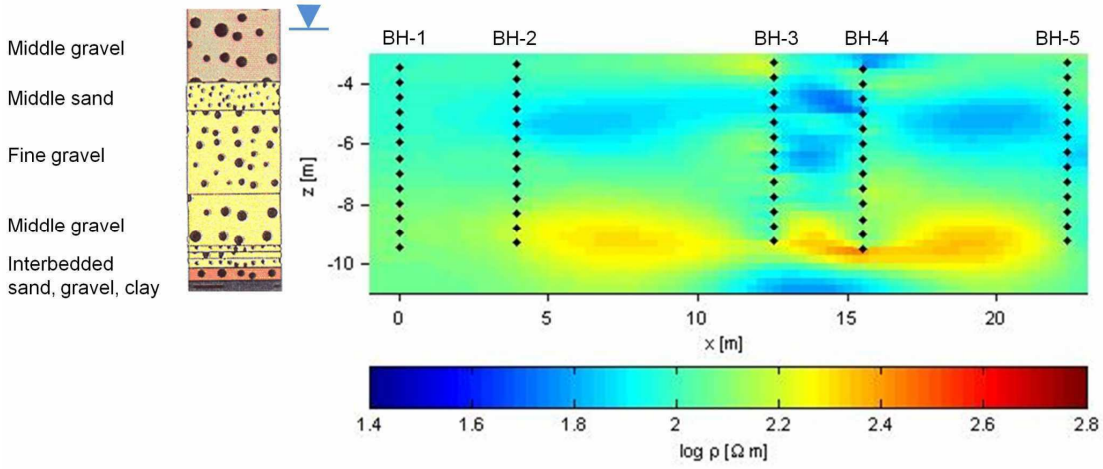

Figure 3.12: Resistivity magnitude image inverted from the field data using the error model in equation 3.4 with parameters based on the Slater and Binley (2006) approach. Solid circles indicate the position of electrodes in the five boreholes. Lithologic column of the Krauthausen site is shown on the left-hand side (after Kemna et al., 2004b).

The phase error models obtained from the single-bin and multi-bin approaches are shown in Figure 3.13. Although the range of resistance values is much smaller than for the tank data (cf. Figures 3.6 and 3.7), a noticeable dependence of the phase error upon resistance is still observed for the multi-bin approach.

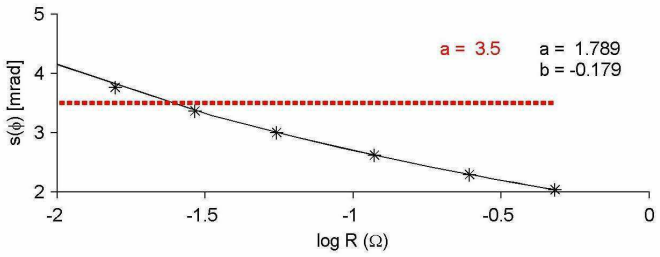

Figure 3.13: Phase error models for the field data based on the multi-bin analysis (black curve) and the single-bin approach (red line) by Slater and Binley (2006). The black dots indicate the standard deviations of the normal-reciprocal data discrepancies obtained in the individual bins. Also shown are the corresponding values of the error model parameters *a* and *b* (*a* in mrad and *b* value for *R* in Ω).

The corresponding phase images are shown in Figure 3.14. Both images are characterized by laterally continuous units. In general, the polarizability is weak and varies only between -2 and -6 mrad. The top layer reveals the highest absolute phase values (around -5 mrad) down to 5 to 6 m bgs, likely to be associated with a non-negligible clay fraction in this region of middle gravel and middle sand (cf. Figure 3.12). Below is a low-polarizable (around -3 mrad), 2 to 3 m thick unit, corresponding to fine gravel, followed again by a subtle polarizability increase with depth in the middle gravel layer and below (cf. Figure 3.12). When comparing the two error model approaches, the low-polarizable unit is shown with better contrast for the new approach. This is obviously a consequence of the overall smaller phase error resulting from the multi-bin analysis (see Figure 3.13), meaning that the data are fitted to a higher degree. Although the difference in the phase imaging results for the two error models is less significant than for the tank data (because the range of measured resistances is much smaller), it nevertheless indicates the superiority of the new approach.

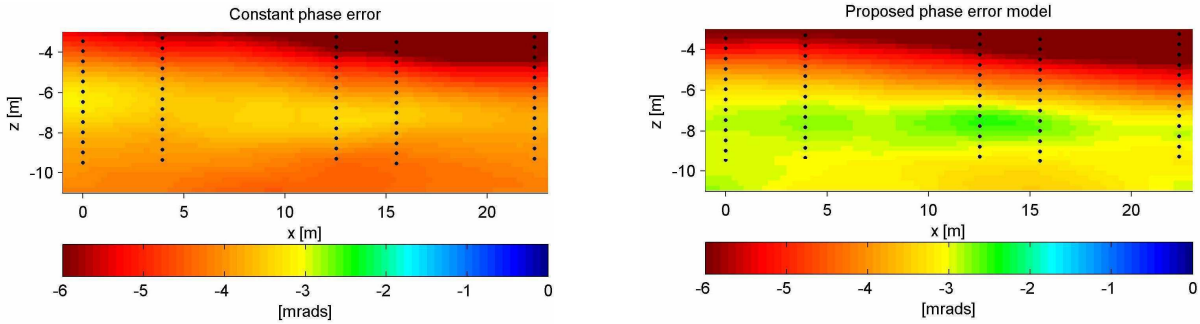

Figure 3.14: Resistivity phase images inverted from the field data using (top) the constant-phase error model according to Slater and Binley (2006) and (bottom) the proposed error model in equation 3.5 with parameters based on a multi-bin analysis. Solid circles indicate the positions of the electrodes in the five boreholes.

3.7. Discussion

For tomographic data sets, high resistances are associated with high signal-to-noise ratios (if the current is fairly constant). Thus it is reasonable to describe the error present in electrical impedance data sets as a function of resistance. Analogous to the case of impedance magnitude, in the previous sections we demonstrated the significant correlation between measured resistance and the phase error. Taking the observed dependency into account in the inversion by means of an appropriate error model helps to avoid the over-fitting of phase data corresponding to low resistances and the under-fitting of phase data corresponding to high resistances – as is the case for the assumption of a constant (i.e., independent of resistance) phase error (cf. Figure 3.6). The adequate parameterization of the error is particularly important for SIP data sets, independent of measurement frequency. Although the overall error level typically increases with measurement frequency (see Figure 3.6), the problem of over- or under-fitting remains the same. Accordingly, we find a rather erratic behavior of the recovered spectral response using a constant phase error, while the images computed with the proposed error model provide a signature in agreement with expectations (Figure 3.10).

For the laboratory experiment, the true dimensions of the copper target might be viewed as being better resolved in the lower-frequency phase images obtained with a constant phase error than in those obtained with the proposed error model (see Figure 3.9). However, this improved resolution is obtained at the cost of considerable artifacts in the images (and is a typical inversion phenomenon in the case of over-fitting), which could easily lead to misinterpretations in the case of unknown targets. For the field study, we found an enhanced contrast (i.e., better resolution) in the phase images calculated with the proposed error model, without the occurrence of noticeable artifacts. This indicates that the proposed error model provides a fair compromise between image resolution and image reliability, in harmony with the philosophy of a smoothness-constraint inversion approach.

It is critical that the selected number of bins and their distribution ensure a homogeneous distribution of the data over the bins, in order to allow for a proper statistical analysis in each bin. In an initial data analysis step, obvious outliers, which may influence the chosen bin size and distribution, should be removed. Furthermore, the data points contained in each bin should exhibit a Gaussian distribution, in order to fulfill the assumption of a random error used in the inversion algorithm. The definition of an adequate number of bins may be particularly challenging for field data, where the total number of measurements may be considerably smaller than in our laboratory experiments. In addition, depending on the measuring protocol employed, only a relatively narrow range of resistances may be covered, incapable of revealing the systematic dependence of phase error upon resistance. For a reliable determination of the parameters of the proposed error model, the resistance range in a data set should be as large as possible, obviously favoring dipole-dipole protocols or combinations thereof. However, even for the considered field data set, where resistances only varied over half an order of magnitude (see Figure 3.13), the proposed error model yields a phase image with improved contrast.

The inversion scheme used in this study is implemented in terms of the logarithm of impedance, mapping logarithm of resistance and phase into real and imaginary components of the data. An alternative approach is to directly invert the real (Z') and imaginary (Z'') components of impedance (e.g., Zimmermann et al., 2008, Commer et al., 2011). Accordingly, data error analysis and parameterization may also be performed in terms of real and imaginary components. However, both quantities scale with resistance, as they are given by

$$Z' = R\cos\phi, \tag{3.6}$$

$$Z'' = R\sin\phi, \tag{3.7}$$

and thus it is plausible to again assume a systematic dependence of their errors upon resistance (note that for the typically low phase values in geophysical applications $Z' \approx R$ and $Z'' \approx R\phi$). Analogous to Figure 3.4, Figure 3.15 shows the distribution of the misfit between normal and reciprocal measurements collected on the experimental tank in terms of real and imaginary components (Z', Z''). Here, the discrepancy (between normal and reciprocal measurements) of the real and imaginary components plotted as a function of the real component ($\Delta Z'$, $\Delta Z''$ vs. Z') exhibits a linear behavior, similar to the model of LaBrecque et al. (1996) (ΔR vs. R) from equation 3.4. Based on this, we suggest that the model proposed by LaBrecque et al. (1996) may be adopted to describe the error for both real and imaginary components:

$$\Delta Z' = K_1 + K_2 Z', \tag{3.8}$$

$$\Delta Z'' = K_3 + K_4 Z', \tag{3.9}$$

where K_1, K_3 represent the absolute errors for the real and imaginary components, respectively, and K_2 and K_4 the respective relative errors. However, a further validation of this approach is beyond the scope of this study. Similar to the analysis of the magnitude and phase data, other relationships, for example the normal-reciprocal discrepancy in the imaginary component as a function of the absolute value of the imaginary component, did not provide any clear trend.

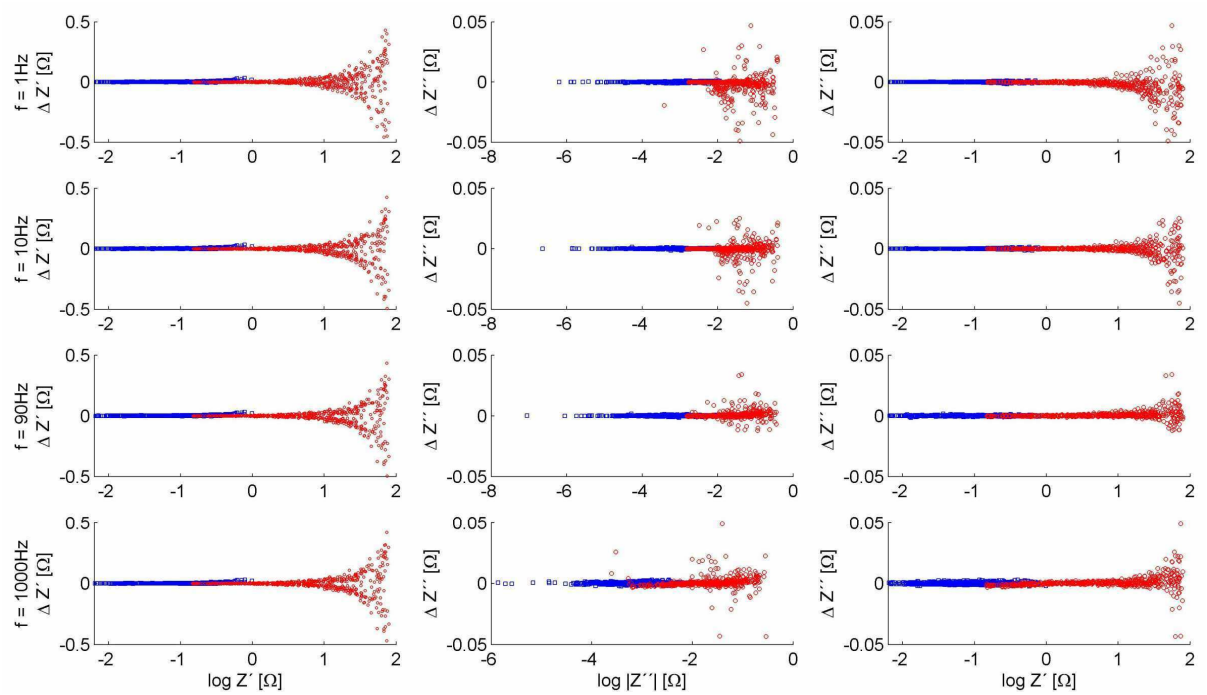

Figure 3.15: Raw tank data collected at different frequencies for both measurement schemes (blue squares: opposite dipoles; red circles: cross dipoles). Left-hand column: Normal-reciprocal discrepancy in Z' versus log Z' Middle column: Normal-reciprocal discrepancy in Z' versus log$|Z''|$. Right-hand column: Normal-reciprocal discrepancy in Z'' versus log Z'. Z' and Z'' denote, respectively, real and imaginary components of resistance.

3.8. Conclusions

In this paper, we propose a new model to quantify the phase error in impedance data sets, as well as a methodology to compute the underlying parameters of the proposed error model. The analysis of impedance data sets collected in the laboratory and the field revealed a significant correlation between the discrepancy between normal and reciprocal phase measurements, on the one hand, and the corresponding mean resistance value, on the other hand. The observed behavior of decreasing phase discrepancy with increasing resistance is consistent for measurements collected at different frequencies, over a wide frequency range. Other dependences of the phase discrepancy, such as its dependence on the absolute phase value, were also studied, but did not show a similarly systematic behavior.

Based on the observed behavior of the phase discrepancy, we propose an inverse power-law relationship to describe the phase error as a function of resistance. Inversion of the considered data sets was performed with two error parameterization approaches, i.e., a constant phase error and a new power-law model. The images computed with the power-law model demonstrated the advantage of the new parameterization as they showed fewer artifacts and respectively higher contrast than those obtained with the assumption of a constant phase error. We attribute this to an underestimation of the error – and correspondingly an over-fitting – of phase data associated with low resistances on the one hand, and an overestimation of the error – and correspondingly an under-fitting – of phase data associated with high resistances on the other hand, when using the constant-error approach. The power-law model takes the observed variation in the phase error into account properly and provides improved

images with a satisfying compromise between resolution and reliability (absence of artifacts). The latter aspect is particularly important if spectral characteristics are to be deduced from multi-frequency phase images, because spatial imaging artifacts may lead to significant distortions of spectral signatures, making a reliable interpretation impossible.

The quantification of phase data errors is critical for obtaining reliable phase images, and the proposed error model might represent an adequate parameterization of universal applicability. We consider an appropriate error description essential for quantitative IP/SIP imaging as it is increasingly becoming of interest, for instance, for hydrogeophysical and biogeophysical investigations. As far as monitoring applications are concerned, however, further studies are required concerning the most appropriate phase error model in a time-lapse inversion scheme.

4. DELINEATION OF SUBSURFACE HYDROCARBON CONTAMINATION AT A FORMER HYDROGENATION PLANT USING SPECTRAL INDUCED POLARIZATION IMAGING[2]

4.1. Abstract

Broadband spectral induced polarization (SIP) measurements were conducted at a former hydrogenation plant in Zeitz (NE Germany) to investigate the potential of SIP imaging to delineate areas with different BTEX (benzene, toluene, ethylbenzene, and xylene) concentrations. Conductivity images reveal a poor correlation with the distribution of contaminants; whereas phase images exhibit two main anomalies: low phase shift values (< 5 mrad) for locations with high BTEX concentrations, including the occurrence of free-phase product (BTEX concentrations >1.7 g/l), and higher phase values for lower BTEX concentrations. Moreover, the spectral response of the areas with high BTEX concentration and free-phase products reveals a flattened spectrum in the low frequencies (< 40 Hz), while areas with lower BTEX concentrations exhibit a response characterized by a frequency peak. The SIP response was modelled using a Debye decomposition to compute images of the median relaxation-time. Consistent with laboratory studies, we observed an increase in the relaxation-time associated with an increase in BTEX concentrations. Measurements were also collected in the time-domain (TDIP), revealing imaging results consistent with those obtained for frequency-domain (SIP) measurements. Results presented here demonstrate the potential of the SIP imaging method to discriminate source and plume of dissolved contaminants at BTEX contaminated sites.

4.2. Introduction

Non-aqueous phase liquids (NAPLs) released into the subsurface (for instances, petroleum contaminants) commonly persist as a separate phase due to their low solubility (e.g., Soga et al., 2004). At sites contaminated with NAPL, two main zones of interest may be described: the source zone and the plume of dissolved contaminants (e.g., Sauck, 2000; Falta et al., 2005; Atekwana and Atekwana, 2010). The source zone is defined as the volume of the aquifer that has had contact with the contaminant (i.e., NAPL) during its release and acts as a continuous source of groundwater contamination. The source zone is commonly characterized by a fraction of contaminant trapped in the pore space which does not drain under the effect of gravity (residual phase), and by NAPLs which can be transported under hydraulic gradient (free-phase) (Newell, 1994; Sauck, 2000; Soga et al., 2004; Atekwana and Atekwana, 2010). Meanwhile, the plume zone mainly contains the dissolved, adsorbed, or volatilized constituents transported away from the source, although free-phase products might also be

[2] Flores Orozco, A., Kemna, A., Oberdörster, C., Zschomack, L., Leven, C., Dietrich, P., Weiss, H. 2012. Delineation of subsurface hydrocarbon contamination at a former hydrogenation plant using spectral induced polarization imaging: Journal of Contaminant Hydrology, 136-137, 131-144.

present, depending on the volume of NAPL spillage (Atekwana and Atekwana, 2010). An adequate discrimination of source zone and plume is critical, for instances, to prevent further migration of contaminants and to select an adequate remediation technique (Atekwana and Atekwana, 2010; Bayer and Finkel, 2006; Schädler et al., 2010; 2012). Current practice in the characterization of contaminated sites typically relies on the extensive use of invasive drilling-based methods, mostly using traditional soil and/or groundwater sampling. Although they give a direct measurement of contamination, such drilling-based methods often do not provide the required spatial resolution to, for example, characterize the extension and geometry of contaminant source-areas and plume of dissolved contaminants. Furthermore, the relatively high costs of the commonly applied drilling-based methods can often render site investigations prohibitively expensive (Dietrich and Leven, 2006; Schädler et al., 2012). This is especially true for large and extended areas with a complex and highly toxic subsurface contamination – commonly referred to as "megasites" (Rein et al., 2011). At such sites, complete information on the contamination situation is very often lacking and with drilling-based methods alone, a cost-efficient and reliable characterization is not possible. However, detailed subsurface information is required to effectively support decision on remediation activities.

In recent years, other, more cost-efficient, methods have been developed for the characterization of contaminated sites capable of providing information which is poorly accessible with drilling-based methods. Examples include approaches such as integral pumping tests (Jarsjö et al., 2005; Beland-Pelletier et al., 2011). This method is based on the measurements of concentration time series collected during pumping tests from which contaminant mass fluxes out of a contaminant zone can be estimated. Due to its large integration volume, the spatial resolution is limited; however, an approximate location of a source zone area upstream of a pumping well transect can often be estimated. A much higher degree of spatial resolution can be achieved by direct push-based soundings (Dietrich and Leven, 2006; McCall et al., 2002). This method allows the measurement of the distribution of hydrogeological, geotechnical and geophysical properties along a vertical profile by advancing small probes into the subsurface (Schulmeister et al., 2003; Lessoff et al., 2010). It is also applicable for the highly resolved characterization of contamination patterns and for delineation of contaminant source areas and plumes by direct sampling (Rein et al., 2011) or by indirect methods, for example, by screening for volatile organic compounds (Bronders et al., 2009). Though the minimally-invasive direct push technology is comparably time and cost efficient, a large number of soundings is often necessary to reliably characterize contaminated sites. Furthermore, the gathered information will not be spatially continuous.

Geophysical methods are well suited for collecting spatially continuous data on the subsurface state (Rubin and Hubbard, 2005; Binley and Kemna, 2005; Atekwana and Atekwana, 2010). From these, electrical methods have long been used and are today routinely applied in industrial practice, for example, for the characterization of the geological setting, buried structures and landfills (e.g., Binley and Kemna, 2005; Revil et al., 2012). From these methods, induced polarization (IP) imaging – an extension of electrical resistivity tomography – has emerged in recent years as a promising tool particularly for environmental applications (e.g., Kemna et al., 2004) to gain spatial information with the required resolution for an

improved lithological characterization of contaminated sites (Slater et al., 2010) and the monitoring of remediation techniques (Slater and Binley, 2006; Williams et al., 2009). Measurements performed in a spectral manner (spectral induced polarization, SIP), i.e., with multiple measurement frequencies (Kemna et al., 2000), exploit the frequency dependence of subsurface properties and can be used, for instance, for biogeochemical state characterization (Abdel Aal et al., 2006, 2010; Ntarlagiannis et al., 2005; Williams et al., 2005) and in an imaging framework at the field scale (Williams et al., 2009; Flores Orozco et al., 2011).

4.2.1. Induced Polarization Imaging

4.2.1.1. Measurement principles

The IP imaging technique is also referred to as complex conductivity imaging, complex resistivity imaging or electrical impedance tomography. The method is based on four-electrode measurements, where two electrodes are used to inject current and two to measure the resulting voltage. IP measurements might be performed in the frequency domain and in the time domain. When performed in the frequency-domain, IP measurements are comprised of amplitude ratio and phase shift between the periodic voltage and current signals. In multi-frequency measurements, commonly referred to as spectral IP (SIP), the frequency dependence of the electrical impedance is measured for a range of low-frequency current injections (typically between 100 mHz and 1000 Hz). IP measurements collected in the time domain (TDIP) are typically performed by measuring the transient decay of the voltage after current shut-off, typically in form of the integral of the decay curve over a predefined time window (so-called integral chargeability). A detailed review of the IP measurement principles can be found in, for example, Sumner (1976); Ward (1990); Binley and Kemna (2005); and Kemna et al. (2012).

Modern field instruments can collect hundreds of potential measurements, deploying tens of electrodes, simultaneously. Multi-electrode surveys (commonly referred to as tomographic surveys), in combination with appropriate inversion techniques, permit to obtain IP images of the subsurface with high spatial resolution (Kemna, 2000; Daily et al., 2004; Binley and Kemna, 2005), providing information that cannot be achieved solely with conventional sampling in boreholes.

Inverted images of IP measurements show the distribution of the complex conductivity in the subsurface. Complex conductivity might be expressed in terms of magnitude ($|\sigma|$) and phase (ϕ), or in terms of real (σ') and imaginary (σ'') components. The real part accounts for energy loss (conduction); whereas the imaginary component is an energy storage (polarization) term (Lesmes and Frye, 2001; Lesmes and Morgan, 2001). Complex conductivity can also be written as a complex resistivity (ρ, with $\sigma=1/\rho$) with real (ρ') and imaginary (ρ'') components:

$$\frac{1}{\rho} = \sigma = |\sigma| e^{i\phi} = \sigma' + i\sigma'', \tag{4.1}$$

where $i = \sqrt{-1}$, and

$$\phi = \arctan\left(\frac{\sigma''}{\sigma'}\right) = -\arctan\left(\frac{\rho''}{\rho'}\right), \tag{4.2}$$

Complex conductivity measurements might be performed at different acquisition frequencies, to gain information about the frequency-dependence of the complex conductivity. Given its relatively simple parameterization, commonly the phenomenological Cole-Cole model (Cole and Cole, 1941) is used to describe the frequency dependence (spectral behaviour) of the complex conductivity (e.g., Pelton et al., 1978). In terms of the complex conductivity, the Cole-Cole model can be written in the form:

$$\sigma(\omega) = \sigma_0\left[1 + m\left(\frac{(i\omega\tau)^c}{1 + (i\omega\tau)^c(1-m)}\right)\right], \tag{4.3}$$

where ω is the angular frequency, σ_0 is the direct-current conductivity (DC conductivity), m is the chargeability (amplitude of polarization), c is the frequency exponent (related to the shape of the spectrum, i.e., the degree of dispersion), and τ is the time constant. The latter is related to the position of the maximum phase shift in the spectrum and is inversely proportional to the characteristic frequency, at which the maximum phase shift is observed ($\tau \sim 1/(2\pi f_c)$), as described for example in Wong (1979).

Recent laboratory studies have demonstrated a better agreement between fitted and measured spectra on the basis of the so-called Debye decomposition (Morgan and Lesmes, 1994), especially if the spectra do not exhibit a typical Cole-Cole shape (Morgan and Lesmes, 1994; Nordsiek and Weller, 2008; Zisser et al., 2010). The Debye decomposition is based on the superposition of the responses of a large number of Debye relaxation terms (the Debye model corresponds to $c = 1$ in the Cole-Cole model in Equation 4.3):

$$\sigma(\omega) = \sigma_0\left[1 + \sum_{k=1}^{n} m_k\left(\frac{i\omega\tau_k}{1 + (i\omega\tau_k)(1-m_k)}\right)\right], \tag{4.4}$$

where n is the number of independent Debye relaxation terms.

4.2.1.2. Environmental applications of induced polarization

The IP method was initially used in the prospection of metallic and certain sulphide ores (e.g., Pelton et al., 1978), due to the strong polarization effects enhanced in the presence of metallic (semi-conductive) minerals – the so-called electrode polarization mechanism (Wong, 1979). However, in recent years the IP method has emerged as a promising tool for environmental applications, even in the absence of metallic minerals, due to its sensitivity to textural and chemical properties of the pore space (e.g., Lesmes and Frye, 2001; Leroy et al., 2008). For rocks and sediments with negligible amount of metallic minerals, two main mechanisms cause the polarization in the low-frequency band (< 100 Hz). Electrochemical polarization, taking place in the vicinity of grain-fluid interfaces, due to the polarization of the electrical double layer surrounding mineral particles (Leroy et al., 2008); and the Maxwell-Wagner polarization, which occurs in mixtures composed of segregated constituents (i.e., phases) with different dielectric permittivity and electrical conductivity, leading to an accumulation of

charge at the boundaries between phases (e.g., Chen and Or, 2006), typically dominating at high frequencies (>10 Hz) (Revil and Florsch, 2010). The so-called membrane polarization also needs to be considered, which is caused by clay particles constituting ion-selective zones (Marshall and Madden, 1959; Titov et al., 2002; Ghorbani et al., 2008).

Measurements conducted in the laboratory have demonstrated, a correlation between the polarization response (σ'' and ϕ) and pore fluid chemistry (Lesmes and Frye, 2001), grain size (Vanhala, 1997; Slater and Lesmes, 2002), and the specific surface area normalized to the pore volume (Börner and Schön, 1995; Weller et al., 2010). Studies have also been conducted in the laboratory (Olhoeft 1985; Vanhala et al., 1992; Börner et al., 1993; Vanhala, 1997) and a few at the field scale (Weller and Börner, 1996; Kemna et al., 1999) to investigate the polarization response of petroleum hydrocarbon contaminated sediments, aiming at the application of the method for the characterization of hydrocarbon contaminant plumes (Atekwana and Atekwana, 2010).

Early SIP studies on, for example, toluene contaminated sediments revealed a shift in characteristic frequency towards lower frequencies (<10 Hz) and an increase in polarization for higher frequencies (>10 Hz), suggesting electrochemical reactions between the contaminant and the grains (Olhoeft 1985; Vanhala et al, 1992). However, later studies (Börner et al., 1993; Vanhala, 1997) revealed a decrease in polarization effect for measurements collected in samples with organic contaminants (e.g., Benzene and oil mixtures). Here, the authors suggested that the hydrocarbon coating the grains impels the formation of the electrical double layer, necessary to build up polarization. A recent study performed on sand samples with different clay content has also shown that the polarization response decreases with increasing the concentration of toluene (Ustra et. al., 2012).

Laboratory studies have revealed the important role of microbial activity underlying the electrical response in aged hydrocarbons. Atekwana et al. (2004) demonstrated that organic and inorganic acids produced by bacteria accelerate the weathering and etching of minerals, suggesting an increase in electrical conductivity (σ'). In their study, the authors also highlight the advantages of deploying indirect methods (e.g., electrical measurements) in order to gain information from highly contaminated sediments, where traditional water sampling might be challenging. Also at the laboratory scale, SIP measurements have revealed an increase in the polarization response (σ'' and ϕ) for samples collected from a BTEX contaminated site (Abdel Aal et al., 2006). However, the authors suggest the microbial colonization of mineral surfaces and their release of ions into solution as the mechanisms underlying the SIP response and not the changes in the mineral surface due to the weathering or etching. Furthermore, they conclude that the enhanced SIP response might occur due to pore constrictions as a consequence of ion-selective biological membranes (Abdel Aal et al., 2006). Cassiani et al. (2009) reported an increase in time constant (τ) values for SIP measurements collected in samples with increasing saturation of non-aqueous phase liquids (octanol), concluding that changes in SIP responses are related to pore obstruction by electrically non-conductive liquids and not exclusively due to electrochemical effects at the grain-electrolyte interface.

Interpretation of field scale IP results is typically challenging, due to the numerous mechanisms potentially underlying the IP response. An example demonstrating the

advantages of IP imaging for improved lithological characterization, compared to pure resistivity imaging, as well as the delineation of hydrocarbon (kerosene) contamination is the study by Kemna et al. (2004), deploying a cross-borehole measurement setup at a site formerly acting as jet fuel depot. Kemna et al. (1999) also performed cross-borehole SIP imaging at this site, where they found an increase of the inferred Cole-Cole time constant in the kerosene-contaminated region. A critical issue for collecting tomographic SIP data over a broad frequency range is the long data acquisition time associated with low-frequency measurements, whereas measurements at higher frequencies are subject to electromagnetic coupling effects (e.g., Pelton et al., 1978; Kemna, 2000). In spite of these limitations SIP imaging was successfully used also by Williams et al. (2009) to delineate changes in the subsurface accompanying the bioremediation of a uranium-contaminated site. Furthermore, a strong correlation could be revealed between SIP parameters (ϕ and σ'') and changes in the geochemical composition of groundwater for different redox status due to bio-stimulation of subsurface microbial activity (Flores Orozco et al., 2011).

Although mostly qualitative, the above-mentioned studies illustrate the potential of the IP method to gain valuable information for the characterization of contaminants at the field scale. Furthermore, several recent studies have focused on the development of mechanistic models describing the processes underlying the electrochemical SIP response (Leroy et al., 2008; Revil and Florsch, 2010), suggesting the possibility of retrieving quantitative hydrogeological information from SIP measurements. Schmutz et al. (2010) proposed a model which relates the IP relaxation time (τ) to the mean grain diameter of oil-bearing sand. The model correctly predicts an increase in the phase angle and relaxation time of the SIP response of bacteria-free samples with increasing oil saturation for different grain sizes.

Although promising results have been obtained in laboratory studies, to date there is no published study regarding the application of the SIP method for the characterization of hydrocarbon contaminated sites at the field scale. To overcome this, and investigate the validation of the polarization response observed in laboratory experiments, this study presents imaging results of SIP measurements collected at a site where high concentrations of BTEX contaminants were reported. Measurements were collected in a wide frequency bandwidth to investigate the frequency dependence of the electrical impedance. Debye decomposition was performed to the SIP imaging results to explore the correlation between spectral parameters (i.e., DC conductivity, total chargeability, median relaxation time) and the distribution of BTEX contaminants. Moreover, in this study we present a quantitative comparison of the imaging results obtained for time-domain TDIP and frequency-domain SIP measurements. The aim of such comparison is to evaluate the performance of both methods for the characterization of contaminated sites. Imaging results are also presented for data collected before and after the removal of anthropogenic structures associated with the hydrogenation plant, with the purpose to assess the impact of overlapping IP responses of anthropogenic structures in the resulting images.

4.3. Material and Methods

4.3.1. Site description

The study area is located near Zeitz, Germany, on the grounds of a former hydrogenation plant. An extended description of the site is presented in other works (Wachter et al., 2004; Schirmer et al., 2006; Dietze and Dietrich, 2011). The site is characterized by heterogeneous sedimentary deposits. As presented in the schematic lithologic column in Figure 4.1, three main units can be distinguished in the study area. In general, a layer consisting mainly of backfill material with silt and sand with some gravel material extends to ~2 m below ground surface (bgs). Beneath this layer are fluvial quaternary gravels, tertiary gravels, and sands forming an unconfined aquifer. An impermeable layer of clay and lignite underlies these sediments at a depth of approximately 11 m. The average depth to groundwater in the study area is approx. 8 m with a groundwater flow direction towards north-northeast. Hydraulic conductivity of the considered aquifer ranges between approximately $5 \cdot 10^{-4}$ and $5 \cdot 10^{-6}$ m/s.

During the operational time of the hydrogenation plant between 1963 and 1990, numerous tank and pipeline leakages as well as negligent handling of chemicals led to a severe contamination of soil and groundwater. Major contaminants at the site are compounds of the BTEX group (benzene, toluene, ethylbenzene, and xylene), with mainly benzene (partly still present as free-phase product).

As part of ongoing remediation activities at the site, contaminated soil will be removed and substituted by uncontaminated material. In the first stage of this remediation, in 2010 a trench was excavated in order to permit the collection of geophysical data. The trench had an extension of ~200 m, a width of ~2 m, and a depth of ~2.5 m, aiming at the removal of underground utilities, such as pipes, foundations, and wires.

4.3.2. Groundwater sampling

During 2008, a field survey was performed to gather more detailed information about the contaminant sources and their distribution in the aquifer. For this purpose, groundwater samples were taken from temporary direct push Geoprobe® sampling wells (with a screen length of 1.1 m) utilizing an inertial foot valve pump, and from PVC monitoring wells with a screen length of 2 m. In some of the wells, benzene concentrations were estimated above the solubility of 1.7 g/l, indicating the presence of free-phase product in the sample. A map illustrating the interpolated concentration of BTEX measured in groundwater samples collected between 8 and 10 m bgs is presented in Figure 4.1. The contamination pattern is clearly dominated by a zone of free-phase product (concentration values above 1.7 g/l), which coincides with the location of a former loading point and tank farm and is one of the major BTEX sources in the study area. Although different sampling techniques and well types were used, the measured contaminant concentrations are consistent. It was also found that the contaminant distribution is stable over time (Wachter et al., 2004; Schirmer et al., 2006; Dietze and Dietrich, 2011).

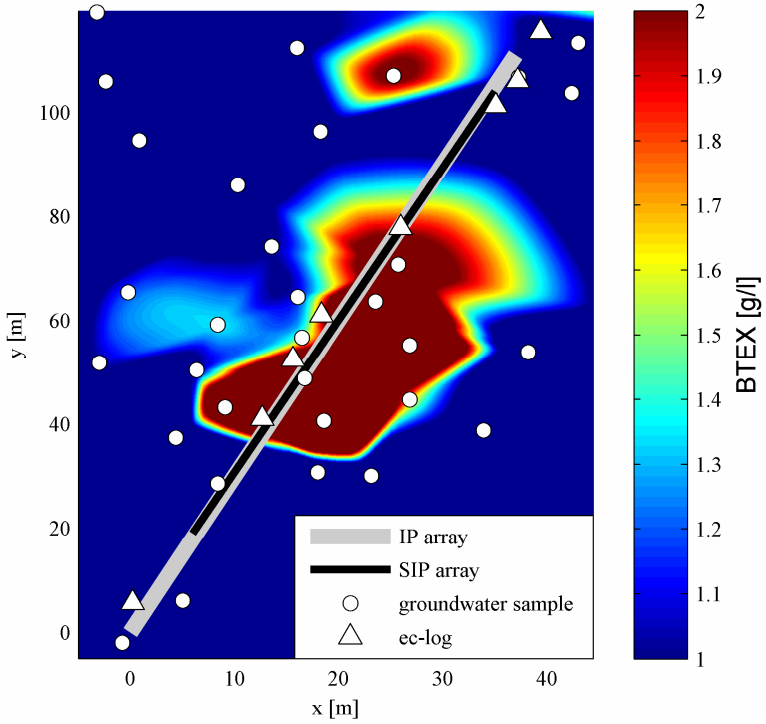

Figure 4.1: Schematic plan view of the investigated site in Zeitz (left). The solid lines indicate the location of the arrays for the collection of time-domain (TDIP) (gray line) and frequency-domain (SIP) (black line) measurements. Open triangles show the positions where ec-logs were collected in 2010. The arrow indicates the direction of groundwater (towards north). The colour plot shows the interpolated BTEX concentrations based on measurements in groundwater samples collected between 8 and 10 m bgs (open circles) in 2008. Data of contaminant distribution were provided by the Landesamt für Altlastenfreistellung (LAF) of the state of Saxonia-Anhalt and the Mitteldeutsche Sanierungs- und Entsorgungsgesellschaft mbH (MDSE), Bitterfeld. A schematic lithologic column of the site is presented (right) for completeness.

4.3.3. Direct-push survey

In 2010, after the installation of the trench, electrical conductivity logging (hereafter referred to as ec-logs) was performed in the course of a direct-push (DP) survey. The ec-logs were obtained by vertically near-continuous measurements of electrical conductivity using a probe comprising four electrodes with 0.25 m spacing (for a complete description of the method see, Schulmeister et al., 2003; Dietrich and Leven, 2006). A Wenner-α configuration was measured every 1.5 cm while the probe was pushed into the ground at eight different locations (as indicated in Figure 4.1), with a maximum depth of 12 m bgs.

4.3.4. Electrical imaging

Tomographic IP data were collected in the time- and in the frequency-domain (hereafter referred to as TDIP and SIP, respectively) along one profile. Measurements were collected at the same location before (December 2009) and after (March 2010) the excavation of the trench – i.e., on the ground surface and inside the trench – in order to evaluate the impact of buried remains of the hydrogenation plant (hereafter referred to as anthropogenic structures) on the electrical images. The location of the profile was selected in order to laterally cross areas with different BTEX concentrations, as depicted in Figure 4.1. Measurements were

collected deploying stainless steel electrodes with an electrode separation of 2.5 m and using a dipole-dipole "skip-3" measuring protocol (i.e., for a length of 10 m for current and potential dipoles). The measurement protocol was carefully designed to minimize unwanted electromagnetic coupling effects in the data, avoiding potential measurements with electrodes located inside the current dipole (as suggested in Pelton et al., 1978), to prevent measurements using polarized electrodes due to previous current injection (LaBrecque and Daily, 2008), and to increase the signal-to-noise ratio for deep measurements (for an intended exploration depth of 12 m, considering a water table depth of approximately 8 m). Measurements were collected as normal and reciprocal pairs for estimation of the data error, where reciprocal measurements consist of those readings where current and potential dipoles are interchanged compared to the normal measurements. TDIP measurements were collected using 48 electrodes, using a square-wave current injection with 50% duty cycle and a pulse length of 2 s, with integral chargeability measurements performed during voltage decay between 240 and 1840 ms after current shut-off. SIP measurements were carried out in the frequency range from 0.07 to 1000 Hz with 37 electrodes, with the first electrode of the SIP measurements corresponding to the ninth electrode of the TDIP measurements, resulting in an overlap of 90 m, as depicted in Figure 4.1.

The electrical images presented here were generated with CRTomo, a smoothness-constraint inversion algorithm by Kemna (2000). Based on a finite-element discretization, the code computes the distribution of complex conductivity in a 2D image plane from a given data set of transfer impedances, Z_j ($j = 1, \ldots, n$; with n being the number of measurements), measured at a distinct frequency f. In the inversion, log-transformed impedances are used as data and log-transformed complex conductivities (of lumped finite-element cells) as parameters to account for the large range of impedance values in typical data sets and of conductivity values for earth materials, respectively. Details on the inversion algorithm, as well as on the underlying forward modelling, are given in Kemna (2000). For the inversion of TDIP measurements, chargeability values were linearly converted to frequency-domain phase values (at the fundamental frequency of 0.125 Hz) using the approach of Kemna et al. (1997), which assumes a constant-phase response. Although the inversion of chargeability measurements can also be performed (e.g., Loke et al., 2003; Fiandaca et al., 2012), the conversion to phase values was done in this study to better compare the imaging result (i.e., phase response) of TDIP and SIP measurements. The inversion of the SIP data was performed by successively applying CRTomo to the data at each frequency. For the Debye decomposition, we used a similar approach to the one proposed by Zisser et al. (2010), which is described in detail in Oberdörster et al. (in preparation).

Quantitative imaging requires an adequate description of data errors to avoid over- and under-fitting of the data within the inversion (see, LaBrecque et al., 1996). Over-fitting occurs due to an underestimation of the data error, leading to the presence of artefacts in the images; whereas under-fitting is a consequence of an overestimation of the data error, resulting in images with poor contrast (i.e., loss of resolution). For the images presented here, estimation of the data error was performed on the basis of the analysis of the misfit between normal and reciprocal measurements. For the resistance (voltage-to-current ratios) data, the data error, $s(R)$, was estimated by a linear model in terms of the measured resistance values (R). Such

model can be written as $s(R) = a + b\,R$, after LaBrecque et al. (1996). For the phase data, a model based on a power-law function of resistance (i.e., voltage signal strength if the current strength does not vary significantly) was applied to describe the error, $s(\phi)$, i.e., $s(\phi) = c\,R^d$ (Flores Orozco et al., 2012). The four fitting parameters (a, b, c and d) of the error models were determined by means of statistical analyses of the discrepancy between normal and reciprocal readings in a set of resistance ranges; we refer to Flores Orozco et al. (2012) for more details on the procedure. Outliers in the data were removed from the data prior to the inversion and were defined as those measurements associated with low current injections (< 10 mA) and large discrepancies between normal and reciprocal phase readings (normal-reciprocal misfit of each configuration exceeding two times the normal-reciprocal standard deviation of the entire data set).

4.4. Results

4.4.1. Conductivity images

Images of the electrical conductivity ($|\sigma|$) for TDIP (time-domain) measurements collected before and after excavation of the trench are presented in Figure 4.2. Note that $\sigma' \approx |\sigma|$ for the typically low phase values in geophysical applications. Overlapping pixels in the conductivity images for data collected after the installation of the trench represent the conductivity measurements from ec-logs collected at eight locations (ZZ1 to ZZ8, from left to right along the direction of the profile). A plot of the distribution of BTEX concentrations is also provided for comparison. Plots in Figure 4.2 show consistent results between the conductivity images and the ec-logs measurements. However, some discrepancies are noticeable (for example, at ZZ 6, at 85 m along the profile direction) in the unsaturated area. Although this discrepancy may be related to the smoothing effect in the inversion, another possible explanation might be related to problems in the contact between the electrodes and the ground during the acquisition of the ec-logs. We observed a poor galvanic contact between the electrodes mounted in the direct push probe and the ground, particularly for the measurements in the unsaturated gravels. This can explain the discrepancies between the ec-logs and the conductivity images in the unsaturated area and the consistent results in the saturated area. Figure 4.2 also reveals consistency in the main features in the images obtained before and after removal of the utilities (i.e., excavation of the trench) and with the lithology of the site (Figure 4.1). The lower conductivity values observed (~8 m bgs) in the image of the data collected before the excavation of the trench are likely due to the presence of anthropogenic structures distorting the images at shallow depths (i.e., close to the underground utilities). Importantly, neither the ec-logs nor the conductivity images show a significant response with respect to BTEX concentrations. However, some indication might be obtained from the lateral variations observed between ca. 40 and 70 m (along profile direction), where an anomaly with higher conductivity values (> 20 mS/m) is revealed, consistent with the highest BTEX concentrations measured. However, the associated variations in conductivity values are less than one order of magnitude and could be, in principle, also explained by lithological changes. The conductivity images computed from the SIP (frequency-domain) data reveal structures and values consistent with those presented in Figure 4.2 and are therefore not shown.

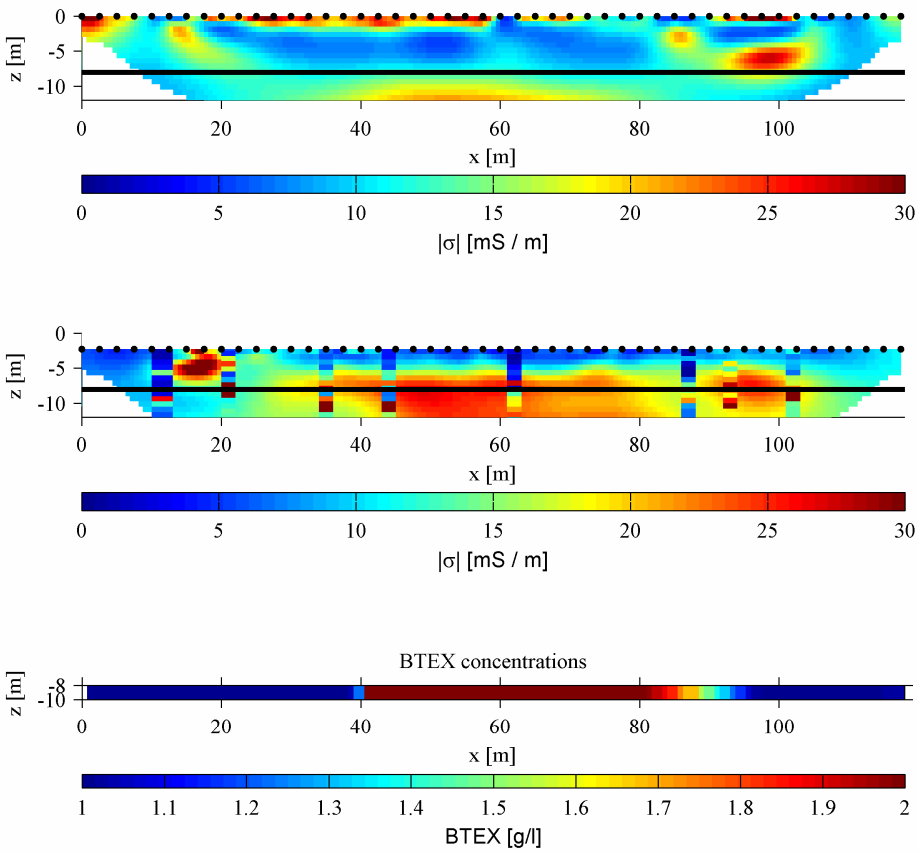

Figure 4.2: Conductivity images computed from TDIP data collected before (top row) and after (middle row) excavation of the trench. The position of the groundwater level is indicated by the solid black line; the position of the electrodes is indicated by the black dots at the top of each image. A plot of the BTEX concentrations measured in groundwater samples collected between 8 and 10 m depth is shown for comparison (bottom row). The conductivity values derived from the ec-logs are represented in the pixels overlapping the conductivity images.

4.4.2. Phase images

The images of phase shift (hereafter referred to as phase images) for the TDIP measurements are presented in Figure 4.3. Here consistency is also exhibited between images computed for data collected before and after the excavation of the trench. Both images show three main features, which extend approximately between 5 and 12 m depth. In the first 40 m (along profile direction) the images show high phase values (> 15 mrad), corresponding with an area characterized by low BTEX concentrations (< 1 g/l). A second anomaly, characterized by the lowest phase values (< 10 mrad), extends from ~40 to 80 m (along profile direction), coinciding with the area where highest BTEX concentrations were observed (> 1.7 g/l and free-phase product). A third anomaly is revealed between ~80 and 110 m (along the profile direction), characterized by high phase values (> 15 mrad), corresponding again to low BTEX concentrations (< 1.7 g/l). This anomaly extends from the unsaturated to the saturated zone for data collected before the excavation of the trench; whereas the image computed for measurements collected after excavation of the trench shows this anomaly only for depths below the groundwater table. We explain the discrepancies in the conductivity and phase images for data collected before and after excavation of the trench by the presence of anthropogenic structures distorting the images, particularly for shallow depths (~5 m depth). Taking this into consideration, we will focus our interpretation of IP signatures on the images

computed for data collected once that the anthropogenic structures had been removed.

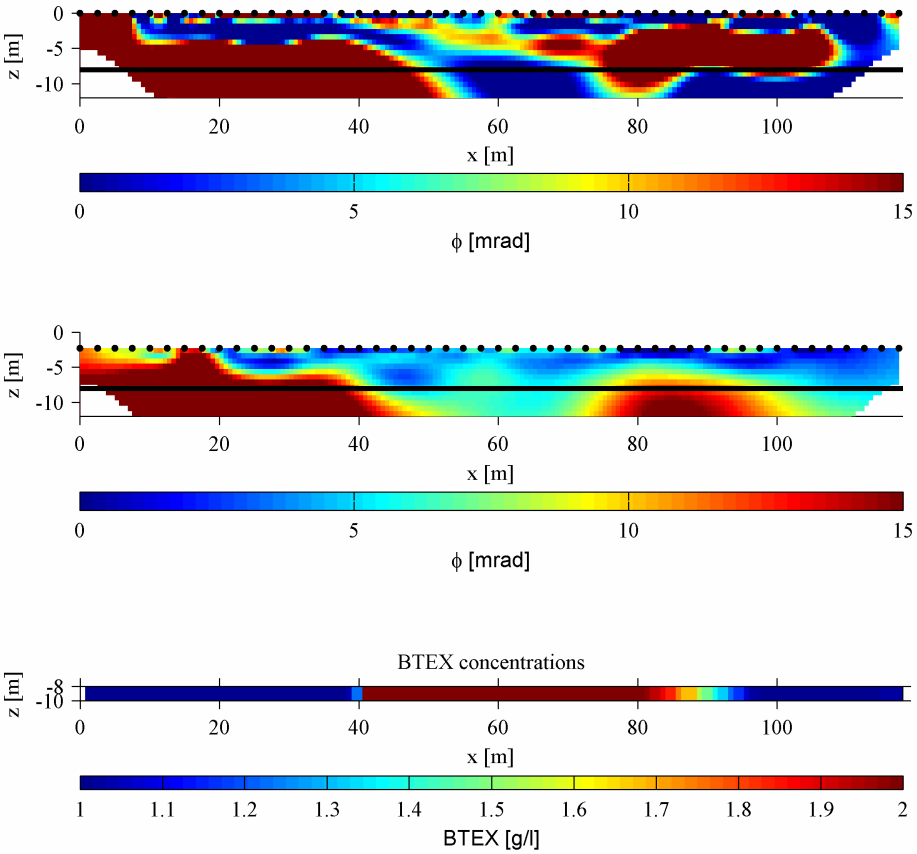

Figure 4.3: Phase images computed from TDIP data collected before (top row) and after (middle row) excavation of the trench. The position of the groundwater level is indicated by the solid black line; the position of the electrodes is indicated by the black dots at the top of each image. A plot of the BTEX concentrations measured in groundwater samples collected between 8 and 10 m depth is shown for comparison (bottom row).

Phase images computed from the SIP data collected inside the trench at selected frequencies are presented in Figure 4.4. The images are consistent with the corresponding image obtained from the TDIP (converted time-domain) data collected inside the trench, with three anomalies in the saturated zone: high phase values (> 15 mrad) for the first 30 m (along profile direction), for locations with low BTEX concentrations (< 1.7 g/l), followed by an anomaly (between ~40 and 80 m along profile direction) characterized by absolute phase values (~5 mrad) coinciding with the location where high BTEX concentrations were measured (>1.7 g/l and large volumes of free-phase product). The last 30 m (along profile direction) show again an increase in the phase values (values ~10 mrad) for BTEX concentrations below saturation concentration (< 1.7 g/l).

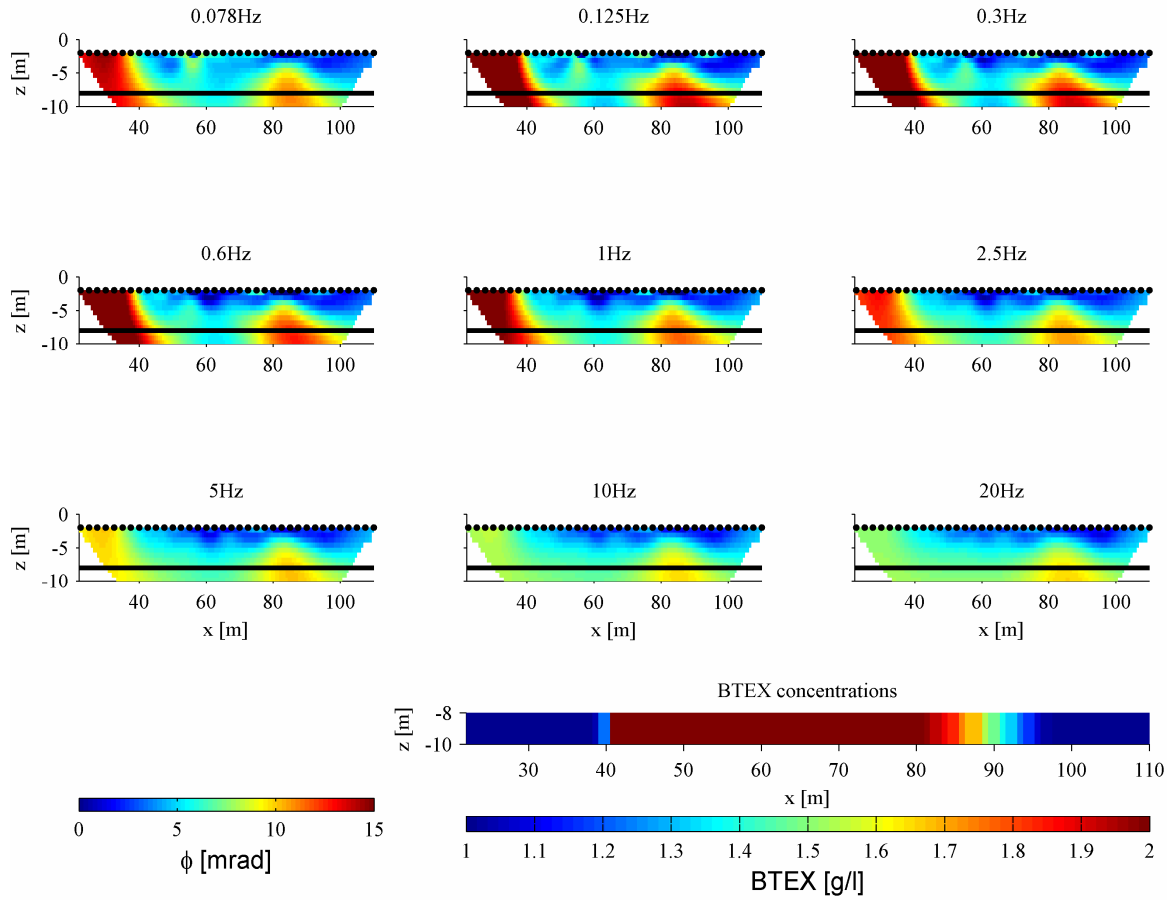

Figure 4.4: Phase images at selected frequencies computed from SIP data collected inside the trench. The position of the groundwater level is indicated by the solid black line; the position of the electrodes is indicated by the black dots at the top of each image. A plot of the BTEX concentrations measured in groundwater samples collected between 8 and 10 m depth is shown for comparison (on the bottom right-hand side).

Considering that phase values (ϕ) are given by polarization-to-conduction ratios (Equation 4.2), it is also important to look at imaginary component of the complex conductivity, which is a measure of polarization only. In order to also highlight the frequency dependence of the complex conductivity in the SIP images, Figure 4.5 shows the spectra of selected pixels, in terms of real (σ'), phase (ϕ) and imaginary (σ'') components of complex conductivity, extracted from SIP images between 8 and 10 m depth and at five different locations (30, 50, 60, 67 and 90 m along profile direction), where contrasting BTEX concentrations were measured. Plots in Figure 4.5 reveal an ambiguous relationship between σ' values and BTEX concentrations, with only modest variations in σ' values (< 10 mS/m) and negligible changes for measurements collected at different frequencies. In contrast, the spectral responses of σ'' and ϕ show a strong dependence on the measuring frequency and a significant contrast in the values of the pixels extracted for different BTEX concentrations. The pixel values extracted from areas with the highest BTEX concentrations (> 1.7 g/l and likely abundant free-phase product) exhibit a relatively flat spectrum, without a frequency peak (for frequencies below 10 Hz); whereas a typical Cole-Cole response (characterized by a frequency peak) is exhibited by the pixels extracted from areas with lower BTEX concentrations (< 1.7 g/l).

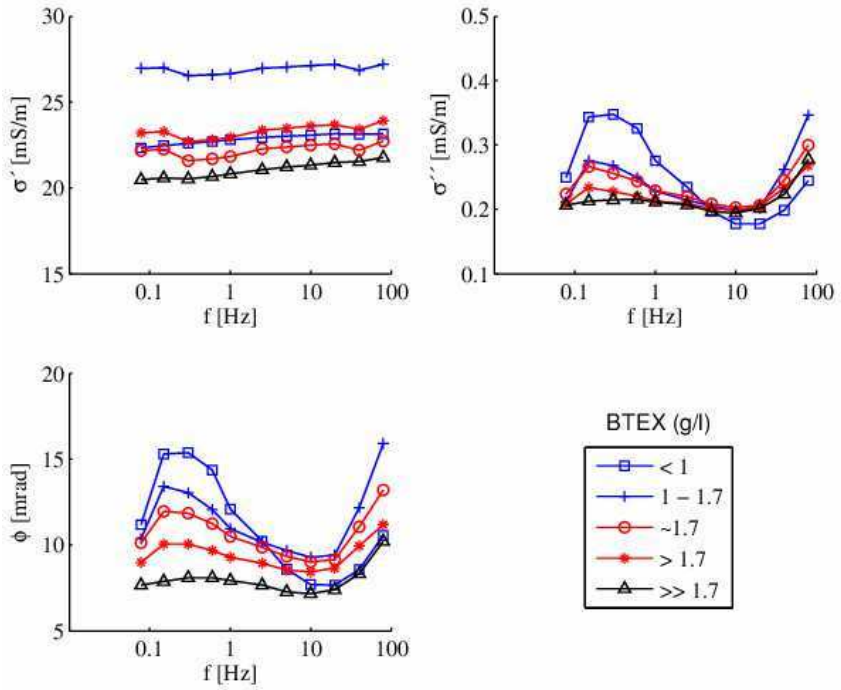

Figure 4.5: Spectral response for selected pixels at different locations (30, 50, 60, 80, and 90 m along profile direction), characterized by different BTEX concentrations. Pixel values represent the mean value of model parameters extracted from the SIP images between 8 and 10 m depth and with a width of 2 m.

To investigate the distribution of the spectral parameters, Debye decomposition (according to Equation 4.4), with 700 terms distributed in the range of 10^{-4} to 10^{4} s (as suggested by Nordsiek and Weller, 2008), was performed for each pixel of the conductivity and phase images. In this study we present three parameters obtained from the Debye decomposition: the DC-conductivity (σ_0), the total chargeability (m_{tot}), and the median relaxation time of the distribution (τ_{50}), which is given by the cumulative relaxation time at which 50% of the total chargeability has been reached (as described in Zisser et al., 2010). The total chargeability (m_{tot}) can be written as

$$m_{tot} = \sum_{k=1}^{n} m_k \qquad (4.5)$$

Plots in Figure 4.5 show an increase in the phase values at high frequencies (> 40 Hz), likely due to electromagnetic coupling in the data. Taking this into account, and to restrict our study to the low-frequency (electrochemical) response, corresponding to the low-frequency peak (i.e., phase maximum) observed in Figure 4.5, spectral parameters (σ_0, m_{tot} and τ_{50}) were computed from the τ distribution accounting only for Debye terms corresponding to frequencies below 40 Hz. For the data presented here, the fitted Debye decomposition response and the inverted complex conductivity values exhibit a smaller deviation than the misfit between normal and reciprocal measurements of the data set.

Figure 4.6 shows the computed images for the spectral parameters (σ_0, m_{tot}, and τ_{50}), as well as a graphical representation of the measured BTEX concentrations (~ between 8 and 10 m depth). A slight decrease in the σ_0 values between ~50 and ~80 m (along the profile direction) in the saturated zone, corresponding to the observed lateral change to high BTEX

concentrations (> 1.7 g/l). Moreover, Figure 4.6 reveals a better correspondence between variations in the BTEX concentrations on the one hand and the distribution of m_{tot} and τ_{50} values on the other hand. In particular, high τ_{50} and low m_{tot} values can be distinguished between ~50 and 80 m (along profile direction), corresponding to the location where high BTEX concentrations (> 1.7 g/l) and occurrence of free-phase product were observed. Plots in Figure 4.6 also indicate lateral variations (between 80 and 110 m along profile direction) to higher m_{tot} and lower τ_{50} values for areas characterized by BTEX concentrations below saturation concentration (< 1.7 g/l).

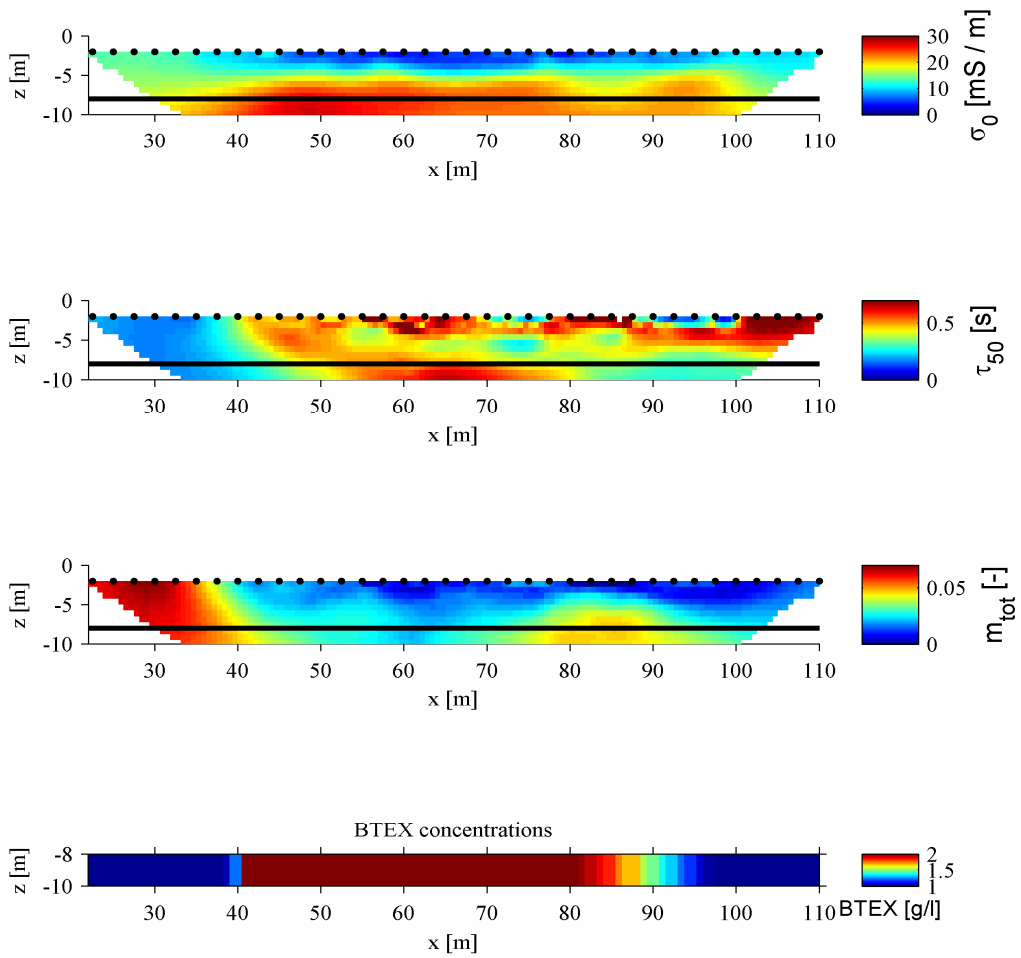

Figure 4.6: Images of spectral parameters (σ_0, τ_{50}, m_{tot}) computed by means of the Debye decomposition. The position of the groundwater level is indicated by the solid black line; the position of the electrodes is indicated by the black dots at the top of each image. A plot of the BTEX concentrations measured in groundwater samples collected between 8 and 10 m depth is shown for comparison (bottom).

4.5. Discussion

Our results demonstrate that changes in ϕ and σ'' associated with variations in the BTEX concentrations are significantly larger (for both time-domain and frequency-domain surveys) than those in conductivity values (σ). Furthermore, images of the phase response (ϕ) (Figures 4.3 and 4.4) and of the spectral parameters (m_{tot} and τ_{50}) (Figure 4.6) exhibit anomalies in the saturated area (between 8 and 10 m bgs) correlated with variations in BTEX concentrations. To better highlight the advantages of complex conductivity imaging in the characterization of

BTEX contaminated sites, we present in Figure 4.7 plots of pixel values extracted from the electrical images (cf. Figures 4.2, 4.3, 4.4, and 4.6) against their related BTEX concentration. SIP values are shown only for data at 0.125 Hz because they exhibited the highest phase response, although similar behaviour is observed for other frequencies (for frequencies below 40 Hz). Extracted pixel values represent the computed median for model parameters sampled every 2 m (with a width of 1 m) over the entire length of the SIP array (between 30 and 100 m along profile direction) and between 8 and 10 m depth.

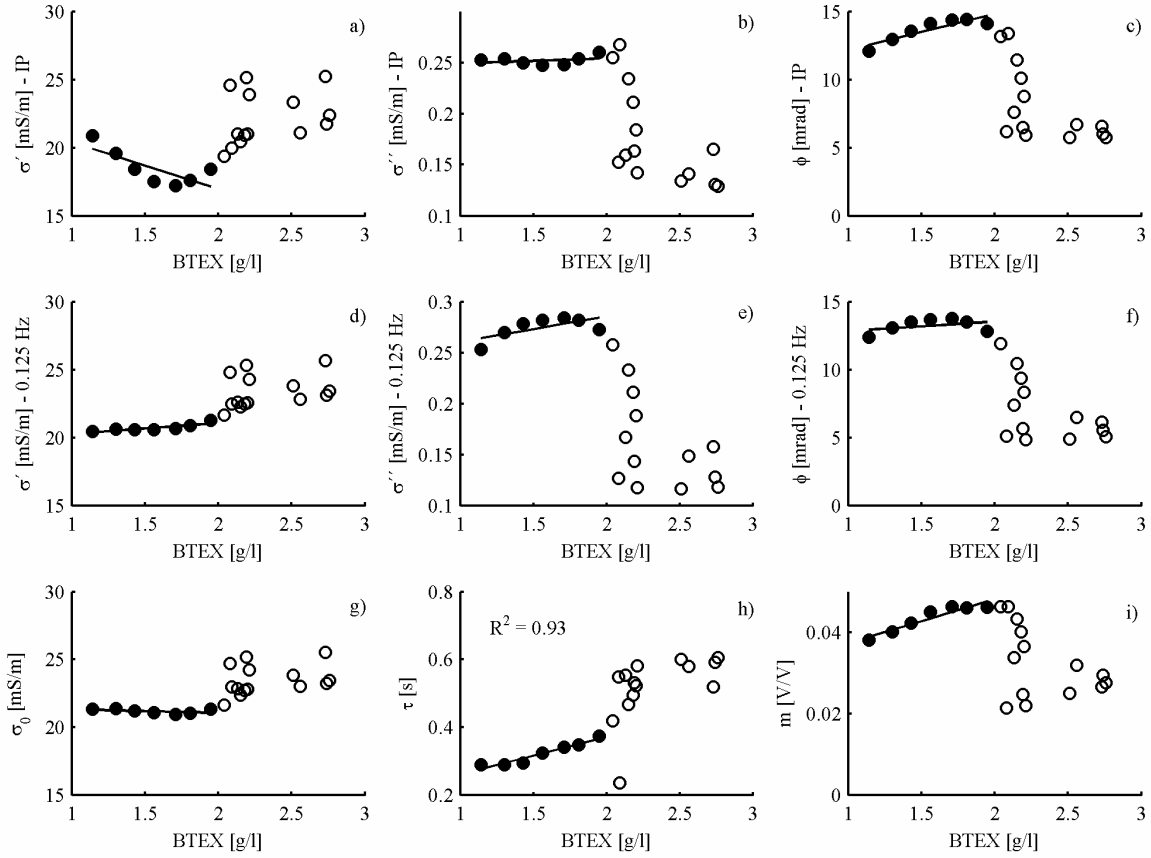

Figure 4.7: Electrical parameters plotted against the measured BTEX concentrations. Top row: Real component, imaginary component, and phase (from left to right) of the complex conductivity extracted from the converted time-domain images. Middle row: Real component, imaginary component, and phase of the complex conductivity extracted from the frequency-domain images at 0.125 Hz. Bottom row: Spectral parameters (σ_0, τ_{50}, and m_{tot}) as obtained from the Debye decomposition of the inverted values for each pixel of the spectral images (cf. Figure 4.6). Solid circles represent BTEX concentrations below saturation concentration (~1.7 g/l), with higher BTEX concentrations indicated with the open circles.

Figure 4.7 shows an ambiguous correspondence between BTEX concentrations and the real component of complex conductivity (σ') for BTEX concentrations below saturation concentration (1.7 g/l), independently of whether the data was extracted from images computed for time-domain data (Figures 4.7a), frequency-domain data (Figure 4.7g) or from the Debye decomposition (Figure 4.7d). However, these three plots show a significant increase in the conductivity (σ') values for increasing BTEX concentrations above BTEX saturation concentration.

Previous studies have demonstrated that hydrocarbon impacted sediments show a decrease in the electrical conductivity (De Ryck et al., 1993). Thus, an increase in BTEX contaminants, displacing pore water, is expected to be associated with a decrease in σ' values. This is in accordance with results presented in recent studies (Schmutz et al., 2010), which also reported a slight decrease in the σ' values for increased oil saturation (up to 40% oil saturation) in measurements collected in sand samples, although the samples were prepared with fresh oil. Nevertheless, studies on aged hydrocarbon have revealed an increase in the measured electrical conductivity associated with the development of porosity and mineral weathering due to carbonic and organic acids released by bacteria (Sauck, 2000; Atekwana et al., 2004). Previous studies at the site have demonstrated ongoing natural attenuation of BTEX contaminants under aerobic (Alfreider and Vogt, 2007) and anaerobic conditions (through sulphate reduction and methane oxidation), especially at the fridge of the plume (Vieth et al., 2005; Gödeke et al., 2006; Schirmer et al., 2006; Fischer et al., 2006). Correspondingly, the increase in electrical conductivity (σ') at high BTEX concentrations (> 1.7 g/l), as observed in Figures 4.7a, 4.7d, and 4.7g, can be explain as the development of porosity due to organic and carbonic acids released by (aerobic) bacteria in the vadose zone leaching to the saturated zone, as suggested in previous studies for sites contaminated with BTEX (e.g., Sauck, 2000). However, more studies are required to validate this hypothesis and fully understand the mechanisms underlying the observed conductivity response, particularly considering the high contaminant concentrations at the site.

Figure 4.7 shows a slight increase in the polarization values (σ'') with increasing BTEX concentrations (below 1.7 g/l) for data extracted from time-domain and frequency-domain images (Figures 4.7b and 4.7e respectively), and a similar trend for the phase angle values (Figures 4.7c and 7f). Furthermore, Figure 4.7 reveals an abrupt decrease of σ'' and ϕ values for BTEX concentrations above ~1.7 g/l. The same behaviour is also observed for the total chargeability (m_{tot}), as obtained from the Debye decomposition. We explain the observed decrease in the polarization response (σ'', m_{tot} and ϕ) due to the occurrence of free-phase product displacing pore water, necessary for the formation of the electrical double layer, where polarization takes place. Laboratory measurements performed on sediments with low clay content have also reported a decrease in the polarization response for increasing (non-miscible) oil saturation, as reported in the studies of Cassiani et al. (2009) and Schmutz et al. (2010). Moreover, the change in the polarization response for BTEX concentrations below and above saturation concentration (and presumably the occurrence of free-phase products) was also reported by Titov et al. (2004) for measurements conducted on samples with different saturation of non-aqueous phase liquids (kerosene).

Previous studies have reported an increase in σ'' and ϕ for measurements carried out on samples collected in an area contaminated with BTEX ongoing microbial natural remediation (e.g., Abdel Aal et al., 2006; Atekwana and Atekwana, 2010). Abdel Aal et al. (2006) suggest that bacterial cells attached to the mineral surface, and processes occurring along the microbial membranes, are the mechanisms underlying the increase in the σ'' and ϕ values. However, recent bio-stimulation experiments have revealed only a modest phase response (< 2 mrad) due to the accumulation of microbial cells or the formation of biofilms, both in laboratory studies (Williams et al., 2005; Ntarlagiannis et al., 2005) and at the field scale

(Williams et al., 2009; Flores Orozco et al., 2011; Chen et al., 2012). Although natural attenuation has been reported for the site, as mentioned before, the plots presented in Figure 4.7 also suggest that the polarization response in our study is mainly controlled by the presence of free-phase products (BTEX concentrations > 1.7 g/l), without any measurable polarization response due to microbial activity or the accumulation of microbial cells.

Figure 4.7h shows a linear relationship between BTEX concentrations below 1.7 g/l and the median relaxation-time (τ_{50}) values, with τ_{50} values increasing for increasing BTEX concentrations, with a high coefficient of determination ($R^2 > 0.9$). Moreover, higher BTEX concentrations (>> 1.7 g/l, and probably increasing concentrations of free-phase products) also reveal an increase in τ_{50} values. This finding is in agreement with the SIP cross-borehole imaging results of Kemna et al. (1999), who found an increase of the relaxation time (τ) in a kerosene-contaminated region of a sand-gravel unit, as well as with laboratory results of Cassiani et al. (2009), who reported an increase in the relaxation time (τ) with increasing the saturation of non-aqueous phase liquids for sand samples. Considering that τ is related to a characteristic length scale at which the polarization is taking place (e.g., Revil and Florsch, 2010), and given the strong correlation observed between τ and BTEX concentrations, we assume that the obstruction of the pores, due to presence of the free-phase product, is responsible for the observed τ response, as also suggested by Cassiani et al. (2009). Our results agree with polarization models proposed in terms of the length of constricted pores (Titov et al., 2004) or in terms of grain size (Schmutz et al., 2010) predicting an increase in τ for increasing NAPL concentrations (for example, kerosene and oil), considering that the smaller the pores are, the larger the polarization is, due to a larger pore volume occupied by the electrical double layer coating grain minerals (Titov et al., 2002).

In addition to the correlations observed in Figure 4.7, phase images for both time-domain (Figure 4.3) and frequency-domain (Figure 4.4) measurements, and also for the total chargeability (Figure 4.6), reveal an anomaly characterized by low phase response (~5 mrad) between ~35 and 70 m (along profile direction), coincident with the location of the highest BTEX concentrations measured (> 1.7 g/l). Pixels extracted from this location reveal a flat spectral response (no phase maximum) in the low frequencies (<10 Hz), as presented in Figure 4.5. Such SIP response may reflect the breakdown of the relaxation process associated with the phase peak for high volume fraction of free-phase product in the pore space replacing the aqueous phase. This anomaly is also consistent with the location of a source zone, as mentioned in previous studies (Schirmer et al., 2006; Alfreider and Vogt, 2007). Hence, we suggest that imaging of the induced polarization response (TDIP and SIP) might provide the possibility to delineate the source zone, or the presence of free-phase products, characterized by a very low polarization response. However, SIP measurements (in a broad frequency range) permit an improved characterization, regarding the spectral response observed. Our results suggest that high BTEX contaminants (and presumably occurrence of free-phase products) are going to be related to a flat phase spectrum ($c \sim 0$), high relaxation time values (τ_{50}), and a low polarization response (ϕ, σ'', and m_{tot} values).

4.6. Conclusions

In this study, IP images have been presented and compared for measurements collected in the time- and frequency-domain in an area of a former hydrogenation plant where high BTEX concentrations (> 1 g/l) are reported. The results presented here demonstrate that IP imaging provides information not accessible with solely resistivity measurements (ec-logs, resistivity images) for the characterization of BTEX contaminated sites.

The images reveal consistency with the BTEX distribution as independently derived from analysed samples. Furthermore, the results are consistent for IP measurements performed in both, time-domain and frequency-domain. Here, we observed a moderate increase in the polarization effects (σ'' and ϕ) for increasing BTEX concentrations below the saturation concentration (< 1.7 g/l). However, the polarization response (σ'' and ϕ) shows a decrease for BTEX concentrations above the saturation concentration (>1.7 g/l), consistent with recent laboratory studies, likely due to the occurrence of free-phase product displacing pore water, where the polarization takes place (as illustrated in Figure 4.8). The same behaviour is observed for the total chargeability (m_{tot}) as obtained from the Debye decomposition of the SIP response. In addition, the median relaxation time (τ_{50}) as obtained from Debye decomposition reveals a strong positive correlation with BTEX concentrations. Such correlation is consistent with the predicted response of models accounting for an increase in the relaxation time due to the presence of NAPL contaminants displacing pore water, resulting in narrow pores occupied mostly by the electrical double layer where the polarization can take place (Titov et al., 2004; Schmutz et al., 2010). Although not directly addressed in this study, our results suggest the possibility to gain information of locations where groundwater sampling is not possible, for instance, in unsaturated areas or at locations with high concentrations of free-phase products. However, further studies are required to evaluate this.

Our study demonstrates the field-scale applicability of the induced polarization (for both TDIP and SIP) imaging method for the characterization of BTEX contaminated sites, even in the presence of anthropogenic structures in the shallow subsurface. The analysis of the spectral response in SIP measurements might provide complementary information for the discrimination of source zone and plume. However, we are aware that the correlation observed between BTEX concentration and electrical parameters (particularly median relaxation-time, τ_{50}) might be site-specific and that the characterization of a different site necessarily requires certain calibration. Results presented in this study suggest that IP images can help to map and characterize contaminant sources zones and thus optimize drillings, installation of monitoring wells, or direct-push investigation points for site assessment and remediation.

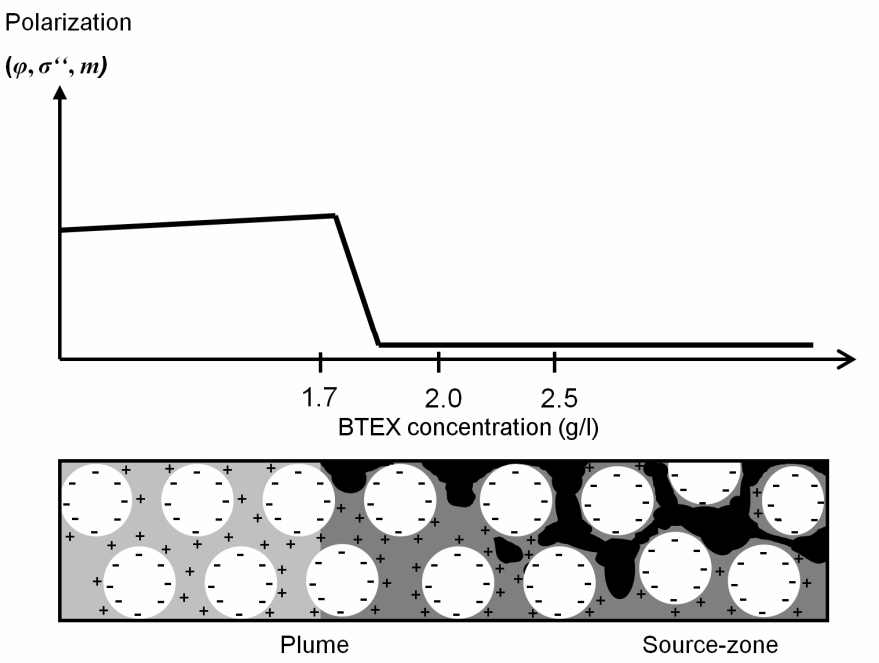

Figure 4.8: Summary of the SIP response observed (top) as a function of BTEX concentrations: a minimal increase in the polarization effect by increasing BTEX concentrations, for BTEX concentrations below the saturation concentrations (~1.7 g/l), followed by an abrupt decrease in the polarization effect for higher BTEX concentrations. The decrease in the polarization response is most probably related to the occurrence of free-phase products displacing pore water necessary for the formation of the electrical double layer where the polarization takes place. The distribution of the different contaminant phases are illustrated in the schematic diagram (bottom), where white circles represent the aquifer sediments (i.e., gravel and sands) with '-' symbols representing the fixed charge at the surface of grains; the '+' symbols account for the ions in groundwater during the application of an external electric field. Gray tones represent different BTEX concentrations dissolved in groundwater and the black areas stand for free-phase product.

5. USING COMPLEX RESISTIVITY IMAGING TO INFER BIOGEOCHEMICAL PROCESSES ASSOCIATED WITH BIOREMEDIATION OF A URANIUM-CONTAMINATED AQUIFER[3]

5.1. Abstract

Experiments at the Department of Energy's Rifle Integrated Field Research Challenge (IFRC) site near Rifle, Colorado (USA) have demonstrated the ability to remove uranium from groundwater by stimulating the growth and activity of *Geobacter* species through acetate amendment. Prolonging the activity of these strains in order to optimize uranium bioremediation has prompted the development of minimally-invasive and spatially-extensive monitoring methods diagnostic of their in situ activity and the end products of their metabolism. Here we demonstrate the use of complex resistivity imaging for monitoring biogeochemical changes accompanying stimulation of indigenous aquifer microorganisms during and after a prolonged period (100+ days) of acetate injection. A thorough raw-data statistical analysis of discrepancies between normal and reciprocal measurements and incorporation of a new power-law phase-error model in the inversion were used to significantly improve the quality of the resistivity phase images over those obtained during previous monitoring experiments at the Rifle IRFC site**.** The imaging results reveal spatiotemporal changes in the phase response of aquifer sediments, which correlate with increases in Fe(II) and precipitation of metal sulfides (e.g., FeS) following the iterative stimulation of iron and sulfate reducing microorganism. Only modest changes in resistivity magnitude were observed over the monitoring period. The largest phase anomalies (>40 mrad) were observed hundreds of days after halting acetate injection, in conjunction with accumulation of Fe(II) in the presence of residual FeS minerals, reflecting preservation of geochemically reduced conditions in the aquifer – a prerequisite for ensuring the long-term stability of immobilized, redox-sensitive contaminants, such as uranium.

5.2. Introduction

A variety of industrial processes have left many sites around the world contaminated with radioactive wastes, such as uranium. Groundwater contamination is of particular concern because oxidized uranium is generally soluble in groundwater, and therefore mobile within the subsurface (Anderson et al., 2003). Thus, different techniques have

[3] Flores Orozco, A., Williams, K.H., Long, P.E., Hubbard, S.S. and Kemna, A. 2011. Using complex resistivity imaging to infer biogeochemical processes associated with bioremediation of an uranium-contaminated aquifer. J. Geophys. Res. 116, G03001.

been applied to effectively remove uranium from groundwater, such as pump and treat or permeable reactive barriers (e.g., Morrison et al., 2006). Unfortunately, such techniques have typically failed to ensure prolonged removal of uranium to levels mandated by regulatory agencies, thus leading to research into new remediation methods. Considering the redox behavior of uranium, bioremediation has emerged as an attractive alternative to lower the concentration of aqueous uranium in groundwater to acceptable levels. The governing idea is to promote the in situ immobilization of uranium through stimulation of indigenous microorganisms capable of reducing the soluble, oxidized form of uranium [U(VI)] to an insoluble form [U(IV)] (Lovley et al., 1991; Gorby and Lovley, 1992). Previous field studies have demonstrated the ability to remove aqueous uranium from groundwater by stimulating iron and sulfate reducing bacteria through injection of organic carbon (e.g., Anderson et al., 2003; Vrionis et al., 2005). However, development of monitoring techniques with sufficient spatial and temporal resolution is still required to assess remediation efficacy at locations not directly sampled by groundwater monitoring wells and over long timescales.

Complex resistivity imaging has been demonstrated to provide valuable information for improved subsurface hydrological and environmental characterization (Kemna et al., 2004; Hördt et al., 2007). This is due to the fact that the electrical induced polarization (IP), measured with the method in terms of resistivity phase, contains important information about the geometry of the pore space, the characteristics of the mineral surface, and the ability to transfer electrical charge across the fluid-mineral interface (e.g., Lesmes and Frye 2001; Binley et al., 2005). Hence, complex resistivity imaging appears to be a suitable technique for monitoring changes in subsurface properties that accompany microbial activity, including the accumulation of reactive aqueous end products and the precipitation of metallic minerals.

As an example, consider the metabolic end products associated with the activity of iron and sulfate reducing microorganisms. Enzymatic reduction of ferric minerals by iron reducing bacteria (FeRB) leads to an increases in both aqueous and sorbed Fe(II), as well as changes in the mineralogy of the mineral phases (e.g., conversion of ferrihydrite to goethite and magnetite) (Lovley et al., 2004). The increase in aqueous sulfide ($\sum H_2S$) that accompanies the activity of sulfate reducing bacteria (SRB) leads to the precipitation of iron sulfides due to elevated concentrations of Fe(II) produced through both enzymatic and abiotic pathways (i.e., reduction of ferric minerals by $\sum H_2S$) (Yao and Millero, 1996). Geophysical exploration of metallic ore deposits has deployed induced polarization and electrical resistivity methods for decades (e.g., Marshall and Madden, 1959; Pelton and Smith, 1976), with particularly strong IP responses reported for massive and disseminated metal sulfides (e.g., Pelton et al., 1978; Wong 1979).

In recent years, laboratory measurements of the spectral induced polarization (SIP) response of biostimulated sediments have been used to delineate changes in physical and chemical properties following enhanced microbial activity (Ntarlagiannis et al., 2005a; Williams et al., 2005; Personna et al., 2008). At the field scale, anomalous IP signatures were found to correlate with the accumulation of iron sulfides following a

biostimulation experiment (Williams et al., 2009). While encouraging, these initial field results were based on data obtained at relatively sparse time intervals and with results reported for only two measurement frequencies (0.125 and 1 Hz). As such, better constrained SIP monitoring experiments are needed to (a) provide appropriate comparisons with laboratory SIP experiments and (b) quantify the effect of microbial activity on the measured signatures (i.e., computed images) at multiple stages during and after the remediation process.

In this study, we present time-lapse complex resistivity imaging results computed for data collected at regular intervals over a two-year period during and after acetate amendment. A thorough data analysis and an improved model to quantify the data error in the underlying inversion were applied to enhance the quality of the computed images. Based on our approach, we suggest that complex resistivity images can provide information – in quasi-real time – about aquifer redox status at different stages during the remediation processes. This is crucial to determine when further biostimulation (i.e., resumed injection of organic carbon) is required in order to maintain conditions favorable for the immobilization of redox sensitive contaminants, such as uranium. Although not directly studied here, the proposed complex resistivity monitoring approach is generally extendable to remediation approaches targeting contaminants other than uranium, such as metals and organic pollutants.

5.3. Material and Methods

5.3.1. Complex resistivity method

This section provides a short description of the complex resistivity method (for a more detailed review see, for example, Sumner, 1976; Telford et al., 1990) and the petrophysical controls on the measurements. The complex resistivity method is based on frequency-domain transfer impedance measurements, where each measurement involves four electrodes (two to inject current and two to measure the resultant voltage) and comprises magnitude (i.e., resistance) and phase (i.e., phase shift between current and voltage signals). Modern measuring devices can collect thousands of measurements in a few hours from electrodes located on the surface or in boreholes.

By means of an inversion algorithm (see, e.g., Binley and Kemna, 2005), a set of measured impedances can be converted into a distribution of complex resistivity values representing the subsurface. Multi-frequency or spectral IP involves impedance measurements over a wide range of frequencies (typically 0.01 to 1000 Hz) to gain information about the frequency dependence of complex resistivity. The complex resistivity ($\rho(\omega)$) can be expressed by its magnitude ($|\rho(\omega)|$) and phase ($\phi(\omega)$), by its real ($\rho'(\omega)$) and imaginary ($\rho''(\omega)$) components, and also in terms of complex conductivity ($\sigma(\omega)$):

$$\rho(\omega) = \rho'(\omega) + i\,\rho''(\omega) = |\rho(\omega)|\, e^{i\,\phi(\omega)} = 1/\sigma(\omega)\,, \qquad (5.1)$$

with $i^2 = -1$ and ω denoting the excitation frequency. The real part accounts for ohmic

conduction (associated with energy loss), whereas the imaginary component is related to polarization (i.e., energy storage) as result of accumulation of charge and charge transfer reactions taking place along the fluid-mineral interface.

The magnitude of the complex resistivity (commonly simply referred to as resistivity) of sediments without electronically conductive minerals is mainly controlled by the properties of the pore-filling electrolyte (i.e., electrical conductivity of the fluid), porosity, and by the connectivity of the pore space, with well-established petrophysical relationships enabling derivation of properties of interest (e.g., porosity and saturation) using resistivity data (Archie, 1942). In contrast, the mechanisms underlying the resistivity phase response of sediments are less well understood and conclusive interpretation of IP data remains challenging, as does quantitative estimation of hydrologic and biogeochemical parameters derived from IP data-sets (e.g., Merriam, 2007; Slater, 2007; Williams et al., 2009). Nonetheless, recently developed mechanistic models describing the physicochemical properties of soils and sediments (in metal-free and bacteria-free porous media) that underlie the SIP response suggest an ever-improving ability to derive quantitative estimates from SIP data-sets (e.g., Leroy et al., 2008; Revil and Florsch, 2010). Additionally, stochastic estimation methods using SIP data and petrophysical relationships offer an approach for quantifying parameters of interest and their associated uncertainties, such as metal sulfide content and particle size distributions of pore clogging mineralization (Chen et al., 2009).

Strong resistivity phase responses are related to the presence of metallic minerals in contact with an electrolyte (e.g., Marshall and Madden, 1959; Pelton et al., 1978). In the presence of metallic minerals (i.e., electronic conductors), the application of an external electrical field induces a change in the charge transfer mechanism from electrolytic (i.e., ionic transport in the pore fluid) to electronic (i.e., electron transfer within the metallic mineral) through electron transfer reactions at the fluid-mineral interface, associated with a phase shift between the applied current and the measured voltage. This mechanism is referred to as electrode polarization (for a complete description, see, e.g., Sumner, 1976; Angoran and Madden, 1977; Wong, 1979; Merriam, 2007; Revil and Cosenza, 2010), and it is strongly related to the surface area and particle diameter of the (semi)conductive mineral grain (Wong, 1979; Slater et al., 2005), as well as the electrolyte composition and aggregation state of the minerals (Angoran and Madden, 1977; Williams et al., 2005; 2009).

Based on the strong phase response for metallic minerals, several studies have described the use of IP measurements for the detection and prospecting of buried ore mineralization, specifically metal sulfides (e.g., van Voorhis et al., 1973; Pelton and Smith, 1976; Wong, 1979). Further studies have demonstrated a proportional correlation between the size and volumetric enrichment of the metallic minerals and a characteristic frequency response (described by a characteristic relaxation time) (Pelton et al., 1978; Olhoeft, 1985). Recent laboratory studies have demonstrated a linear correlation between the imaginary component of the complex conductivity and the total metallic surface area of precipitated metallic minerals (Slater et al., 2005; 2007), with other

studies attributing changes in the frequency-dependent responses to variations in the concentration of electroactive ions in the pore fluid (Angoran and Madden 1979; Wong, 1979; Williams et al., 2005) or spatiotemporal changes in location of the mineralization (Ntarlagiannis et al., 2005a). Given the multitude of condition-dependent factors controlling the complex resistivity response, further studies are warranted.

Lesser but measurable complex resistivity phase responses have also been reported for non-metallic minerals, related to polarization mechanisms in the electrical double layer surrounding mineral particles, denoted as electrochemical polarization (described in, e.g., Lesmes and Morgan, 2001; Leroy et al., 2008). Additionally, a membrane polarization mechanism (e.g., Marshall and Madden, 1959; Titov et al., 2002) can also exist when surface charge at the grain interface establishes a potential throughout the pore constituting ion-selective zones.

Additional factors may influence complex resistivity signatures associated with microbial activity. Formation of microbially-mediated minerals leads to an increase in total specific surface area, and, hence, enhancement of phase responses. The effect is enhanced if the precipitated minerals exhibit polarization properties (i.e. metallic minerals, such as FeS, which facilitate the change in charge transfer process) (Ntarlagiannis et al., 2005a; Slater et al., 2005; Williams et al., 2005). The stimulated growth of microbial cells is also related to an increase of surface area, suggesting a measurable increase of the phase response (e.g., Abdel Aal et al., 2004; 2010; Davis et al., 2006); however, related studies have demonstrated that the polarization values generated at the microbial cell-fluid interface are significantly lower (<2 mrad) than the response generated by precipitated metallic minerals (~15 mrad) (Ntarlagiannis et al., 2005b; Williams et al., 2009). Reversible reactions may also impact the complex resistivity signatures (e.g., Slater et al., 2007), including changes in the geochemical composition of the groundwater and solid phase constituents. Particularly, the cessation of active biostimulation and organic carbon amendment delivery may lead to re-oxidation of reduced mineral phases (e.g., FeS) that in turn can generate a variety of (semi)conductive iron oxide minerals (e.g., ferrihydrite, lepidocrocite, goethite, etc.). Such a process can lead to additional changes in the surface area of pore-filling mineralization and further modify spatiotemporal complex resistivity signals.

5.3.2. Site description

The Rifle IFRC site is located near Rifle, Colorado (USA), on the grounds of a former uranium processing facility. An extended description of the site is given in many other works (e.g., Anderson et al., 2003; Vrionis et al, 2005; Englert et al., 2009). In general, an artificial clay-rich fill extends from the ground surface to a depth of ~1.75 m below ground surface (bgs). Beneath this fill are unconsolidated fluvial sediments composed of sand, silt, clay, and gravel. While varying seasonally by ca. 1 m, the average depth to groundwater in the vicinity of the complex resistivity study area is 3.5 m bgs and flow direction is toward the southwest. Reported iron bearing minerals in the unconfined aquifer consist of goethite, chlorite, magnetite, hematite, and pyrite (Qafoku et al.,

2009). The low permeability Wasatch formation (composed of Eocene gravels, silts, and clays) underlies these sediments at a depth of ca. 6.5 m bgs and constitutes a lower boundary to groundwater flow.

5.3.3. Experimental set-up

As described by Williams et al. (2011), biostimulation via acetate injection was performed to reduce and immobilize U(VI) in the unconfined aquifer. Site groundwater was amended with bromide and acetate and introduced to the aquifer using ten injection boreholes (Figure 5.1). Fifteen monitoring wells were used to collect groundwater samples for geochemical analysis throughout the experiment, including three up-gradient and twelve down-gradient from the area of injection (Figure 5.1). The first experiment was initiated in August of 2007, during which acetate and bromide were injected over 31 days, with a target in situ aquifer concentration of 5 mM acetate and 2 mM bromide. An extended biostimulation experiment was performed in 2008. For the second experiment, the first 15-day injection period targeted an in situ acetate concentration of 5 mM, followed by 8 days where acetate-free groundwater was injected. A second period of 5 mM acetate injection occurred over the next 15 days, followed by an increase to 15 mM on day 38 due to the complete consumption of acetate as a result of extensive sulfate reduction. Injection of elevated acetate (15 mM) continued through day 110, after which time injection ceased.

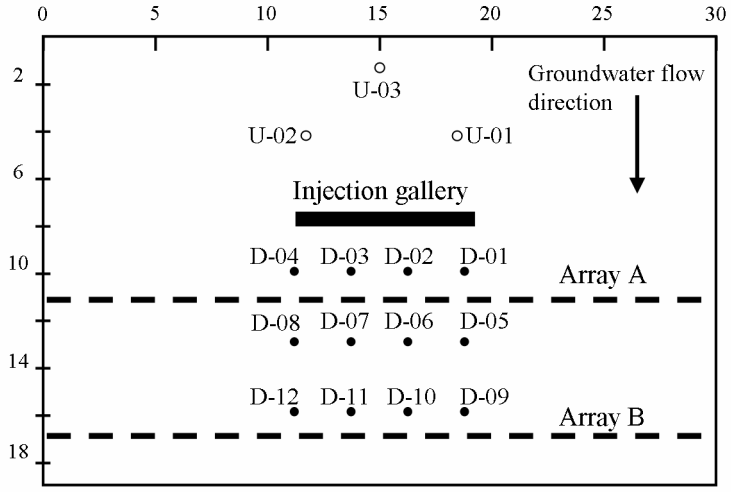

Figure 5.1: Schematic representation of the experimental set-up. Monitoring wells up-gradient (o) and down-gradient (●) of the injection gallery (solid black rectangle) are referred to the direction of the groundwater flow (solid arrow). The dashed lines represent the location and extent of the array A and B. All the dimensions are given in meters.

Complex resistivity measurements were collected periodically during both experiments (2007 and 2008) along two arrays (array A and B), which were oriented perpendicular to groundwater flow and were located approximately 3 and 6 m down-gradient from the injection gallery (Figure 5.1). Each array consisted of 30 electrodes with 1 m spacing for a total individual profile length of 29 m. The two arrays were parallel and centered with respect to the injection gallery (Figure 5.1). For the 2007 experiment, measurements were obtained before injection began and then every 12 days during the

injection interval; a final data-set was collected 8 weeks after the injection ceased. For the 2008 experiment, the measurements were collected every 3 days during the injection cycle and every 2 and 6 months afterwards over the course of a year. Measurements in 2007 were collected at 1 and 4 Hz, similar to Williams et al. (2009); while the data collected in 2008 were acquired over the 0.25 to 64 Hz frequency range, attempting to record a wider spectral response. A summary of the different acetate injections, their duration and details on the acquisition of complex resistivity measurements is presented in Table 5.1.

Year	2007	2008	2008	2008	2008	2008	2008-2009
No. of injection	1	2	3	4	5		-----
Duration [days]	31	15	8	15	6	66	-----
Acetate [mM]	5	5	-----	5	15		-----
Bromide [mM]	2	2	-----	2	2		-----
Meas. Freq. [Hz]	1, 2, 4	0.25 - 4	0.25 - 4	0.25 - 4	0.25 - 4		0.25 - 4
Acquisition period [days]	12	3	3	3	2	30	180

Table 5.1. Timeline of the different amendment injections and details on the acquisition of complex resistivity measurements.

Non-polarizing metal-metal salt ($Cu/CuSO_4$) electrodes were deployed in order to minimize unwanted effects due to polarization of the electrodes, which are particularly critical for measurements made at low frequency (<10 Hz), as noted in previous studies (e.g., LaBrecque and Daily, 2008). The measurements in this study were carried out using a dipole-dipole configuration with a skip-3 protocol (i.e., each dipole skipping 3 electrodes, resulting in a dipole length of 4 m for the current and potential dipoles). This measurement protocol has been used in a previous study (Williams et al., 2009) showing a good resolution for depths up to 7 m, and reasonable acquisition times. The selection of an appropriate measuring protocol plays a significant role regarding the resolution of the images and it has been the issue of several works (e.g., *Bing and* Greenhalgh, 2000; Stummer et al., 2004). It is also important to remark that measurements of complex resistivity performed at low frequencies (< 1 Hz) require large acquisition times (up to several hours). Regarding all this, the aim is to find the best compromise between high signal-to-noise ratio (favored by large dipole lengths), high resolution (favored by small dipole lengths) and short acquisition times (determined by the number of independent measurements). At the same time it is also important to avoid measurements where the potential electrodes are placed inside the current dipole and those with a large separation between dipoles (restricting the depth of penetration of our measurements) in order to reduce inductive coupling (e.g., Pelton et al., 19878).

5.3.4. Inversion approach

Our investigation is based on complex resistivity images obtained using the smoothness-constraint inversion code by Kemna (2000). The algorithm calculates the complex resistivity distribution on a 2D grid of lumped finite-element cells from a given data-set of transfer impedances (Z_i, i = 1, …, N; with N being the number of measurements), at a given frequency. Within the inversion, log-transformed impedances are used as data and log-transformed complex resistivities as parameters. Through using log-transformed values, it is possible to account for the typical large range in the resistance values of data-sets and of electrical resistivity values in the subsurface, respectively. The inversion algorithm iteratively minimizes an objective function, $\Psi(\mathbf{m})$, which is composed of the measures of data misfit and model roughness, with both terms being balanced by a real-valued regularization parameter, λ:

$$\Psi(\mathbf{m}) = \left\| \mathbf{W}_\mathrm{d} \left[\mathbf{d} - \mathbf{f}(\mathbf{m}) \right] \right\|^2 + \lambda \left\| \mathbf{W}_\mathrm{m} \mathbf{m} \right\|^2 , \tag{5.2}$$

In equation 5.2, $\mathbf{d}$ is the complex-valued data vector ($d_i = \ln Z_i$), $\mathbf{m}$ is the complex-valued model vector ($m_j = \ln \rho_j$; j = 1… M; with M being the number of parameter cells), $\mathbf{f}(\mathbf{m})$ is the complex-valued operator of the forward model, $\mathbf{W}_\mathrm{m}$ is a real-valued matrix evaluating the first-order roughness of $\mathbf{m}$, and $\mathbf{W}_\mathrm{d}$ is a complex-valued data weighting matrix. Assuming uncorrelated and normally distributed data errors, $\mathbf{W}_\mathrm{d}$ is diagonal and given by

$$\mathbf{W}_\mathrm{d} = \mathrm{diag}\left\{ \frac{1}{\varepsilon_1}, ..., \frac{1}{\varepsilon_N} \right\} , \tag{5.3}$$

with

$$\varepsilon_i = s(\ln|Z_i|) + \mathrm{i}\, s(\phi_i) , \tag{5.4}$$

where $s(\ln|Z_i|)$ and $s(\phi_i)$ represent the real-valued data error (standard deviation) of the log magnitude (i.e., resistance), $|Z_i|$, and the phase, ϕ_i, respectively, of the impedance $Z_i = |Z_i| \, \mathrm{e}^{\mathrm{i}\varphi_i}$. Note that $d_i = \ln|Z_i| + \mathrm{i}\, \phi_i$, and that Equation 5.4 describes an error ellipse in the complex plane around d_i. The iteration process is stopped when the RMS data misfit,

$$RMS = \sqrt{\frac{1}{N} \sum_{i=1}^{N} \frac{\left| d_i - f_i(\mathbf{m}) \right|^2}{\left| \varepsilon_i \right|^2}} , \tag{5.5}$$

reaches a value of one for a maximum possible value of λ, yielding the smoothest model subject to fitting the complex data within the error ellipse defined by ε_i. Once the complex data misfit has reached an RMS value of one, it is possible to run additional inversion iterations purely for the phase (i.e., keeping the already inverted magnitude image fixed) in order to improve the phase image. This is critical, given that the log resistance error is typically one order of magnitude larger than the phase error (Kemna,

2000). Kemna (2000) refers to this step as “final phase improvement”, because it yields an image with “improved” quality for the phase. Note that in the final-phase-improvement step the same inversion framework is used as outlined above, but with all data and model quantities referring only to the phase. More details on the inversion scheme and the underlying modeling algorithm are given in Kemna (2000).

5.3.5. Data error parameterization

The quantification of the data error plays a significant role in the quality of the final images and thus in their interpretation. Images with low contrast (i.e., resolution) may result from an overestimation of the data error (i.e., under-fitting in the inversion), whereas under-estimating the data error leads to over-fitting in the inversion and artifacts in the images (e.g., LaBrecque et. al., 1996).

Although it is impossible to know the exact variance and distribution of the error in the data, approaches have been developed to provide estimates. For tomographic data-sets, analysis of the misfit between normal and reciprocal measurements has commonly been used to estimate the error present in the data (e.g., LaBrecque et al., 1996; Slater and Binley, 2006). In order to perform reciprocal measurements, it is necessary to reacquire the data for each quadrupole after interchanging the current and potential electrodes. This procedure permits one to account for random errors in the data associated with fluctuations in injected current, changes in the contact resistance between the electrodes and the ground surface, and other unsystematic errors (Binley et al., 1995). Systematic errors are those which show a correlation within the data-set (e.g., malfunction of a particular electrode or measuring channel, or poor galvanic contact). Systematic errors should be corrected, if possible, or deleted from the data-set prior to the inversion. Particular sources of systematic errors for IP measurements include polarization of the electrodes (e.g., Dahlin et al., 2002) and electromagnetic coupling (e.g., Pelton et al., 1978).

In this study we estimate the error for resistance measurements based on the model proposed by LaBrecque et al. (1996), which has been used in various studies (e.g., Kemna et al., 2002; Köstel et al., 2008; Oberdörster et al., 2010). This model is based on a linear relationship between the measured resistance, R ($R = |Z|$), and its error, $s(R)$, written as

$$s(R) = a + bR \ , \tag{5.6}$$

with appropriately chosen parameters a, $b > 0$. For impedance phase (ϕ) measurements, the assumption of a constant error value has been commonly used (e.g., Kemna et al., 2004; Williams et al., 2009). In this study, we applied a recently developed error model to quantify the phase error, $s(\phi)$, as a power-law function of resistance, that is governed by the voltage signal strength for constant currents, written as

$$s(\phi) = aR^b \ , \tag{5.7}$$

with appropriately chosen parameters $a > 0$ and $b < 0$ (different from those in Equation 5.6). Usage of the power-law error model (Equation 5.7) in the inversion provides images with fewer artifacts and larger contrast relative to those computed using previous approaches (Flores Orozco et al., *submitted to Geophysics*, 2010).

Measurements of contact resistances were performed before each data acquisition with observed values in the order of ~500 Ω; the current injection was performed with a constant voltage of 55 V, resulting in injected currents of 100-200 mA. Outliers were defined as (a) those measurements performed with injected currents below 10 mA, and (b) measurements with a difference between normal and reciprocal values exceeding two times the standard deviation (of the normal-reciprocal misfit) of the entire data-set. After removal of outliers, average values of normal and reciprocal measurements were used for the inversion, consisting of approximately 390 data points per data-set. Error parameters (a and b in Equations 5.6 and 5.7) were quantified by means of statistical analyses in a set of resistance ranges as described in Flores Orozco et al. (*submitted to Geophysics*). Independent error parameters were computed for each data-set collected at different times and frequencies.

5.4. Results

The images of resistivity magnitude ($|\rho|$) and phase (ϕ) (subsequently referred as resistivity and phase, respectively, for the sake of simplicity) computed for baseline data collected along arrays A and B are presented in Figure 5.2. For the resistivity images, the inversion algorithm solves for the same model for both frequencies deployed; for conciseness we present only the image computed for the data collected at 1 Hz. The structures visible in the images of arrays A and B are consistent with the stratigraphy of the site (as presented in the lithologic column in Figure 5.2 for comparison), which consists of three principal units. The thin, shallowest layer, which is characterized by low resistivity values (~10 Ωm), corresponds to the clay-rich fill material that covers most of the Rifle IFRC site. The middle unit is comprised of fluvial sediments and is characterized by more resistive sand, silts, and gravels (values between 100-400 Ωm), with a thickness of ~4.5 m. Lateral variations observed in this resistive unit are interpreted to be due to heterogeneities in the alluvial sediments of the aquifer, as evidenced by a wide range of grain sizes (<1 mm to >10 cm) recovered during drilling. The relatively low resistivity values (~100 Ωm) observed near the center of the images (between 10 and 20 m along the direction of the array) correlate with the presence of more clay-rich sediments, as documented during geological logging of the recovered sediments. The lower unit corresponds to the silt-rich and less resistive Wasatch formation (< 70 Ωm).

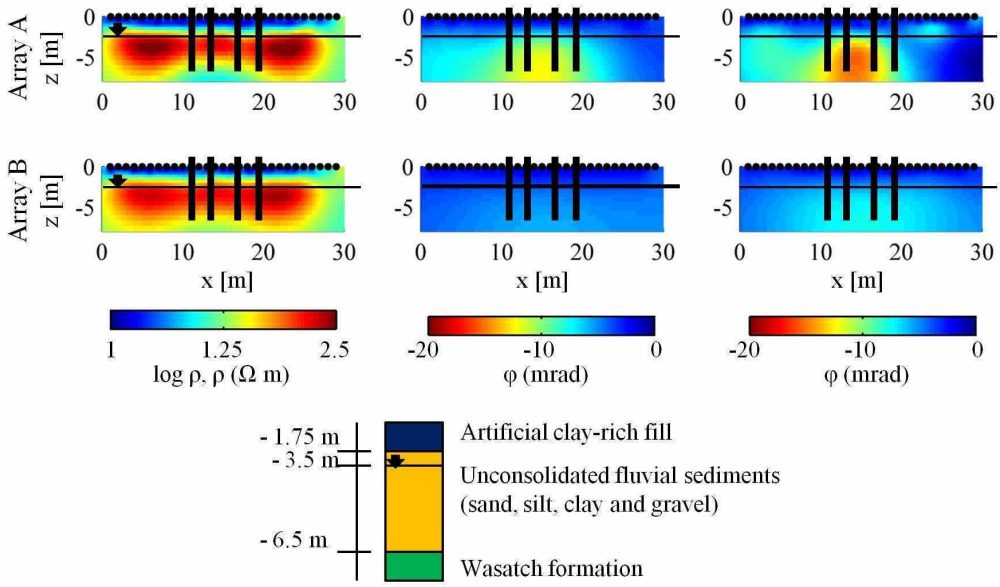

Figure 5.2: Complex resistivity images of the baseline data collected for array A and array B. Left: resistivity images for data collected at 1 Hz. Middle and right: phase images computed for data collected at 1 and 4 Hz, respectively. The depth of the water table is marked for each image (solid line), as well as the position of the electrodes at the surface (black points). Black lines in the top images indicate the location of observation wells D-04, D-03, D-02, and D-01 for Array A; and D-12, D-11, D-10 and D-09 for Array B (from left to right). On the bottom a representative lithologic column of the site is given for comparison.

For array A, the presence of heterogeneities near the center of the array is also noticeable in the phase images (Figure 5.2). The phase response at both frequencies (1 Hz and 4 Hz) reveals a significant polarizable anomaly extending between 3 and 7 m bgs in the center of the images (between 10 and 20 m in the direction of the array). The 4 Hz phase image reveals a more polarizable anomaly (~–18 mrad) than the 1 Hz image (~-12 mrad). For array B, the images show a similar resistivity structure but significantly lower absolute phase values (~5 mrad) relative to the array A images.

The consistency between the phase values observed along array A and those reported for previous complex resistivity measurements at the Rifle site collected elsewhere during acetate based biostimulation experiments (Williams et al., 2009) suggests the accumulation of reduced biogeochemical end products, such as Fe(II), FeS, and FeS_2 in the region of strong phase response on array A. Indeed, analysis of recovered material from several holes drilled in the vicinity of the anomaly of array A documented sediments enriched in refractory organic carbon, total reduced inorganic sulfur (e.g., FeS, H_2S, and S^0), framboidal pyrites, and uranium (Qafoku et al., 2009). Recovered sediments during the drilling of observation wells along array B (D-09, D-10, D-11, D-12) contained visibly more oxidized sediments, with a far lower abundance of metal sulfides and sorbed Fe(II), as compared to sediments in the vicinity of array A. Such results may help explain the variation in the baseline phase response observed along arrays A and B. Referred to as zones of natural bioreduction, these regions are

characterized by trapped organic matter that sustains slow but elevated rates of microbial activity that in effect replicate the same suite of biogeochemical reactions that accompany acetate amendment (albeit over much longer timescales). Such reactions include the accumulation of Fe(II) and insoluble sulfide minerals that track slow rates of iron and sulfate reduction, respectively.

The monitoring results presented in this study pertain primarily to data collected along array A, which exhibited a stronger phase response over the 2007 and 2008 injection cycles relative to array B. While possibly a consequence of subsurface heterogeneity described above, the larger temporal phase response observed along array A is likely related to elevated rates of microbial activity and more extensive mineral precipitation occurring in closer proximity to the injection gallery. Although larger in magnitude, variations in the phase response observed along array A were largely consistent with those observed along array B.

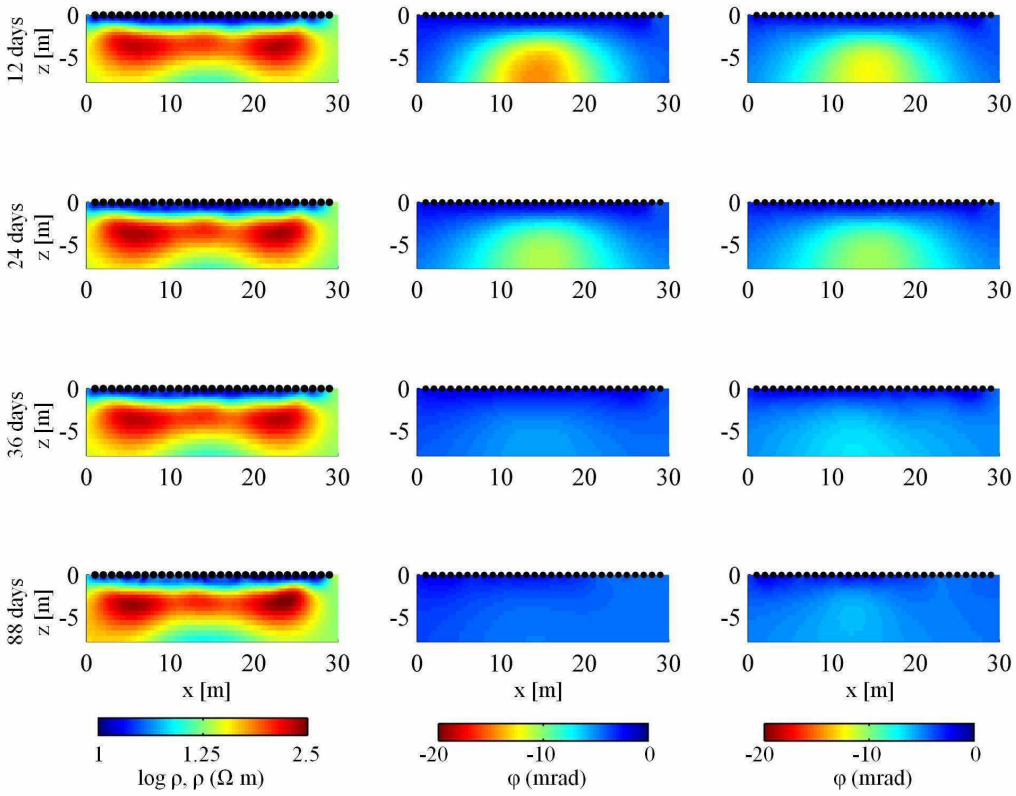

Figure 5.3: Complex resistivity images for the measurements collected along array A in 2007 after an injection of 5 mM acetate and 2 mM bromide. Elapsed time in days is referenced to the start of acetate injection. Left: resistivity images for data collected at 1 Hz. Middle and right: phase images computed for data collected at 1 and 4 Hz, respectively.

The resistivity and phase images computed for data collected along array A during and after acetate injection in 2007 are presented in Figure 5.3. While negligible change in resistivity was observed over the injection interval, the phase response at two frequencies (1 and 4 Hz) decreased following the short-duration acetate injection. The last time point for which data was collected (88 days after the injection was stopped) reveals the virtual disappearance of the baseline phase anomaly, with the images

revealing low overall absolute phase values (<5 mrad) across the zone of injection.

The second biostimulation experiment began in July 2008, 361 days after the first injection. The resistance values measured exhibited negligible variations throughout the 2008 experiments (for the different frequencies collected), with values consistent with those observed in 2007. In contrast, significant variability in the phase response at different measurement times was observed, particularly for the lowest frequency collected (0.25 Hz), as presented in the histograms of the resistance and phase measured values for selected days post initial 2007 acetate injection (Figure 5.4).

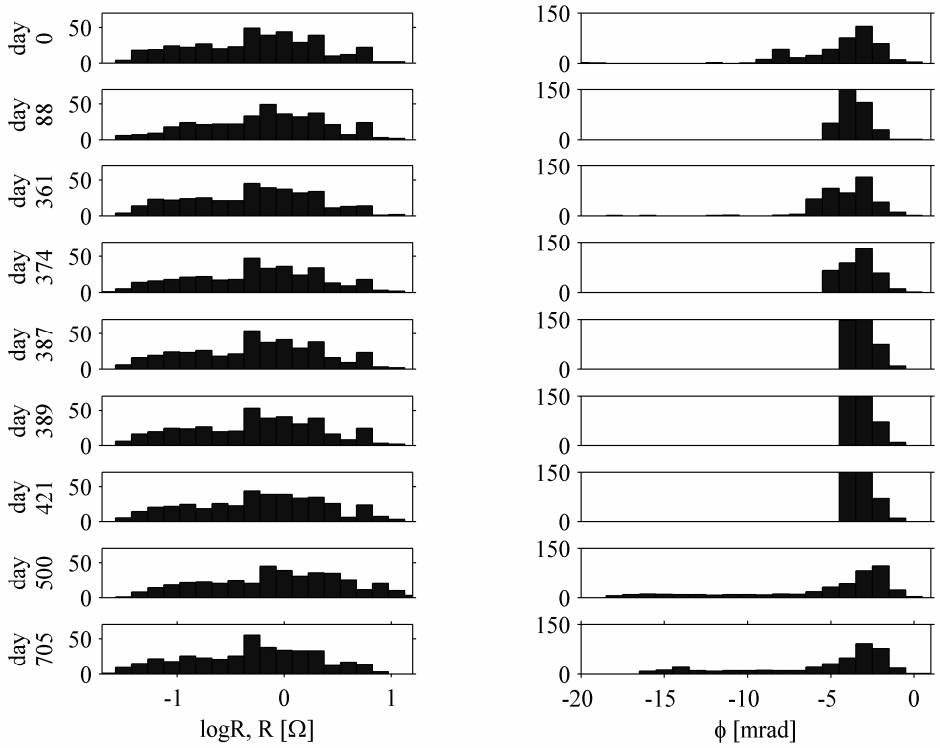

Figure 5.4: Histogram of measured resistances and phase values along array A at 0.25 Hz. Elapsed time in days is referenced to the start of acetate injection in 2007.

The phase images associated with the second biostimulation experiment are shown in Figure 5.5. Here the images at frequencies below 1 Hz show the strongest phase anomalies during the injection period (days 361 to 426), with absolute values above 10 mrads; these values decrease significantly for the images between days 393 and 396. For the images after day 450 – shortly after finishing the last injection – the values begin to increase rapidly. The largest phase anomalies exceeded 40 mrad (in absolute values) and persisted for hundreds of days after acetate injection ceased and long after both acetate and bromide were lost from the system.

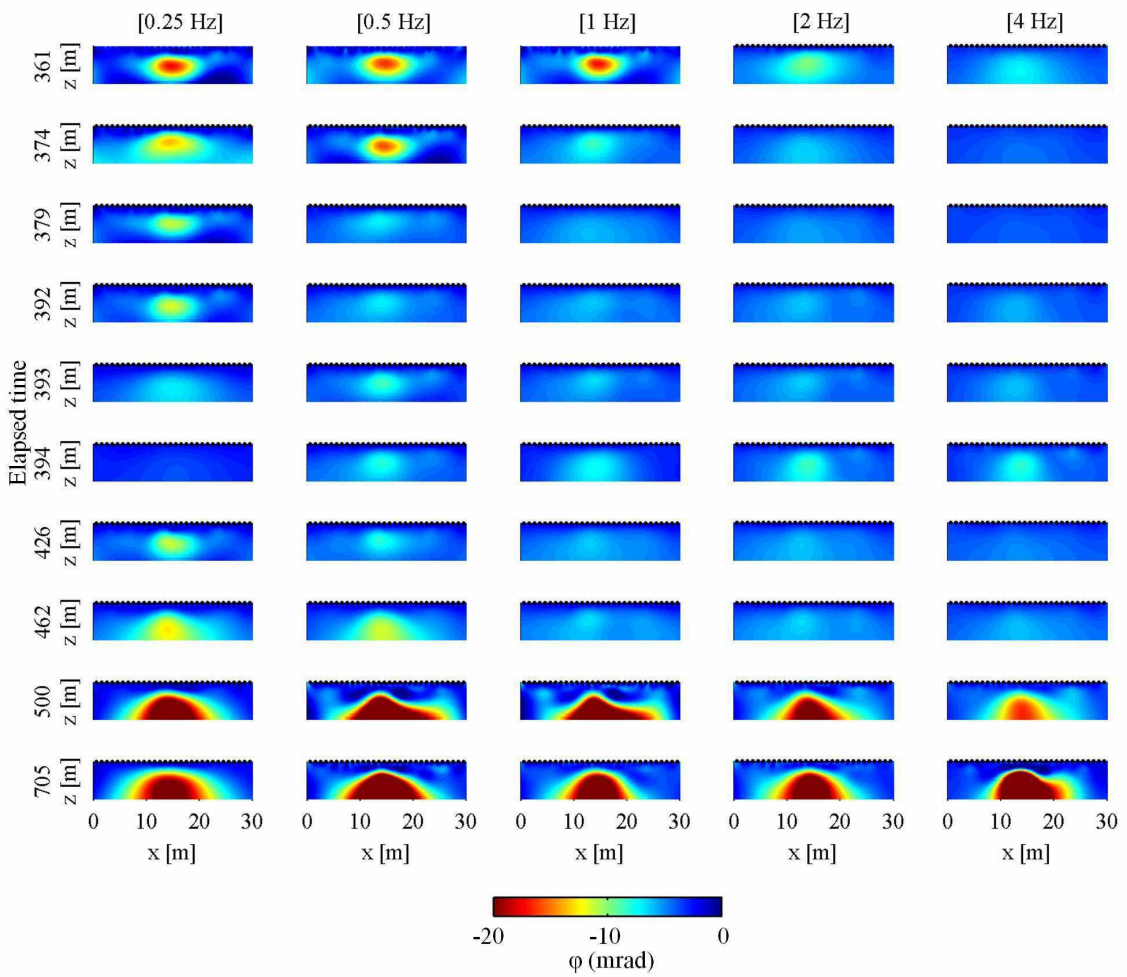

Figure 5.5: Selected phase images for the data collected at different times and frequencies along array A during 2008-2009. Elapsed time in days is referenced to the start of acetate injection in 2007.

For data collected at higher frequencies (>1 Hz), sediments exhibited a less anomalous phase response with time over the injection interval, with anomalies between -6 and -10 mrads. The images show a consistent result as a function of time, with absolute phase values generally decreasing as frequency increases. Similar to the low-frequency data, the strongest phase anomalies were observed after injection ended (day 461), with maximum absolute values 20-30 mrad greater than their pre-injection value. Data collected at higher frequencies are not presented, as analysis of the raw data showed poor data reciprocity and evidence of significant electromagnetic coupling.

To better illustrate the advantages of the phase data error parameterization deployed (Equation 5.7), we also present the images obtained using the assumption of a constant phase error value (Figure 5.6a), as used by Williams et al. (2009). For brevity, we only present the images computed for representative times and for data collected at 0.25 Hz, where more pronounced temporal phase changes were observed. The constant phase data error for each data-set was computed based on the analysis described by Slater and Binley (2006). The images obtained with a constant phase error show similar structures to those obtained with the power-law error model for the corresponding days (Figure

5.5), but they are more impacted by inversion artifacts (particularly for measurements collected before or after acetate injection at frequencies below 4 Hz) or of poor contrast (i.e., poor resolution exhibited in images for data collected during the periods of acetate injection, especially at 4 Hz).

The inversion of tomographic complex resistivity data-sets collected at different frequencies (or time-lapses) has not received enough attention to date; it has been a subject of only a few studies (e.g., Kemna et al., 2000; Hördt et al., 2007; Commer et al., 2011). A recent study demonstrated the advantages of defining individual error parameters (i.e., for each frequency) for tomographic SIP data collected over a wide frequency band (Flores Orozco et al., *submitted to Geophysics*, 2010). For the data collected in the present study, the inversion performed with individual error parameters (computed for each frequency and time-lapse) solved for images exhibiting features consistent for similar conditions at different periods during the experiment (i.e., a consistent phase response was observed in the images for data collected in the course of each amendment injection).

An alternative procedure is to invert all data-sets assuming the same error level (i.e., with identical error parameters). The aim is to avoid the comparison of images with a different level of fitting (i.e., smoothness). Inversion results computed using the highest error parameters found (for each frequency) by means of the power-law error parameterization are presented in Figure 5.6b. These images show similar structures as the images computed by means of individual error model parameters (Figure 5.5), albeit with slightly lower contrast, as expected, due to over-estimation of the error. For completeness, we present in Figure 5.6c the images obtained using a constant phase error defined by the highest value found, which leads to significantly decreased contrast in the images compared to Figure 5.6a.

Other approaches may include merging all data collected (for single or multi-frequencies) and computing the error parameters characterizing the composite data-set; or using the average value of the computed error model parameters of the individual data-sets (for data collected at different times and/or frequencies). Both approaches were tested here resulting in images strongly affected by artifacts (data not shown). The definition of common error parameters applicable to data-sets collected at single or multiple frequencies is challenging, if not impossible, and such a solution may ultimately require a trial and error approach, not suitable for the monitoring purposes of this study. As a result, our interpretation and discussion refers solely to those images obtained by means of individual error parameters, as presented in Figures 5.2, .53, and 5.5.

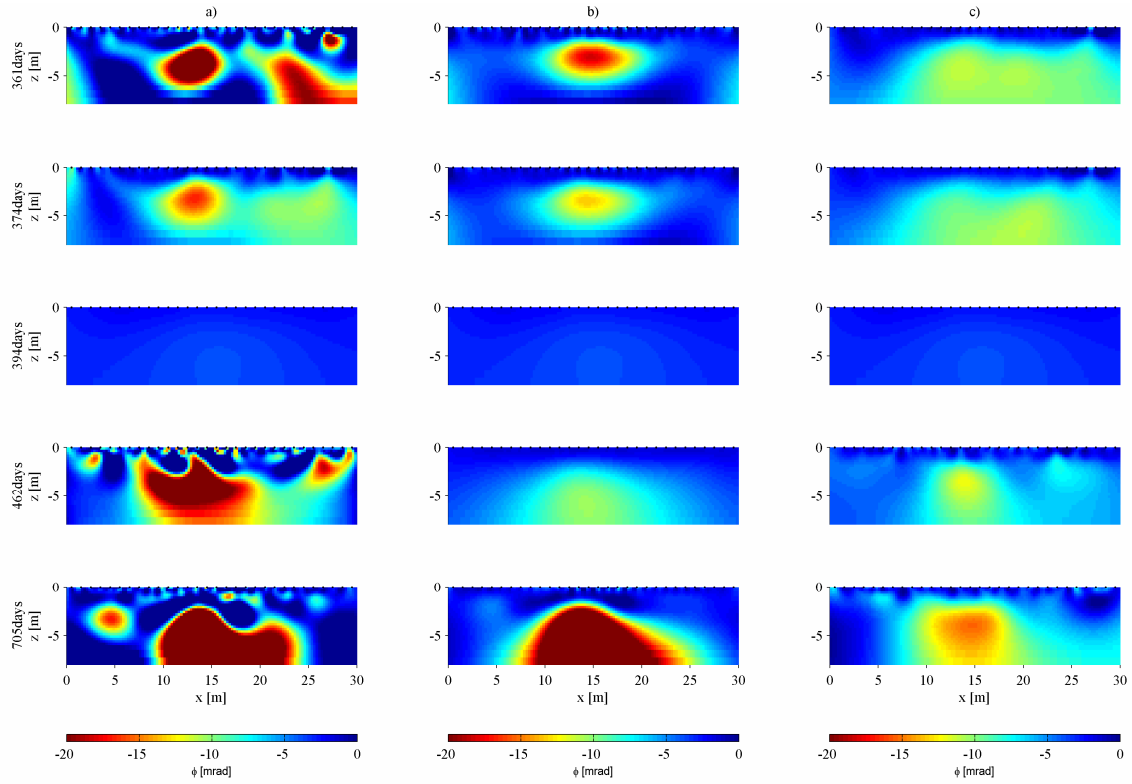

Figure 5.6: Selected phase images inverted by means of different error parameterizations: a) individual error parameters considering a constant phase data error value; b) highest error parameters considering a power-law error model (Equation 5.7); and c) highest value considering a constant error value. Data were collected at 0.25 Hz along array A during 2008-2009. Elapsed time in days is referenced to the start of acetate injection in 2007.

To better highlight the phase response for different times, we plotted it against the elapsed time for the two years of monitoring, starting with the baseline measurements collected before the first acetate injection in 2007 (Figure 5.7). The phase value plotted represents a pixel in the vicinity of the observation well D-01, defined by the value of the model parameters between 4.5 and 5.5 m bgs and 18 and 20 m along the direction of the profile. For comparison, we present in Figure 5.7 the plots of relevant geochemical parameters observed in groundwater samples collected in well D-01.

The observed geochemical and geophysical responses (Figure 5.7) are consistent for all the experiments (i.e., injections) performed in 2007 and 2008, with slight variations between them due to the different concentrations of injected acetate. Considering the response observed in the Figure 5.7, four different periods can be easily distinguished:

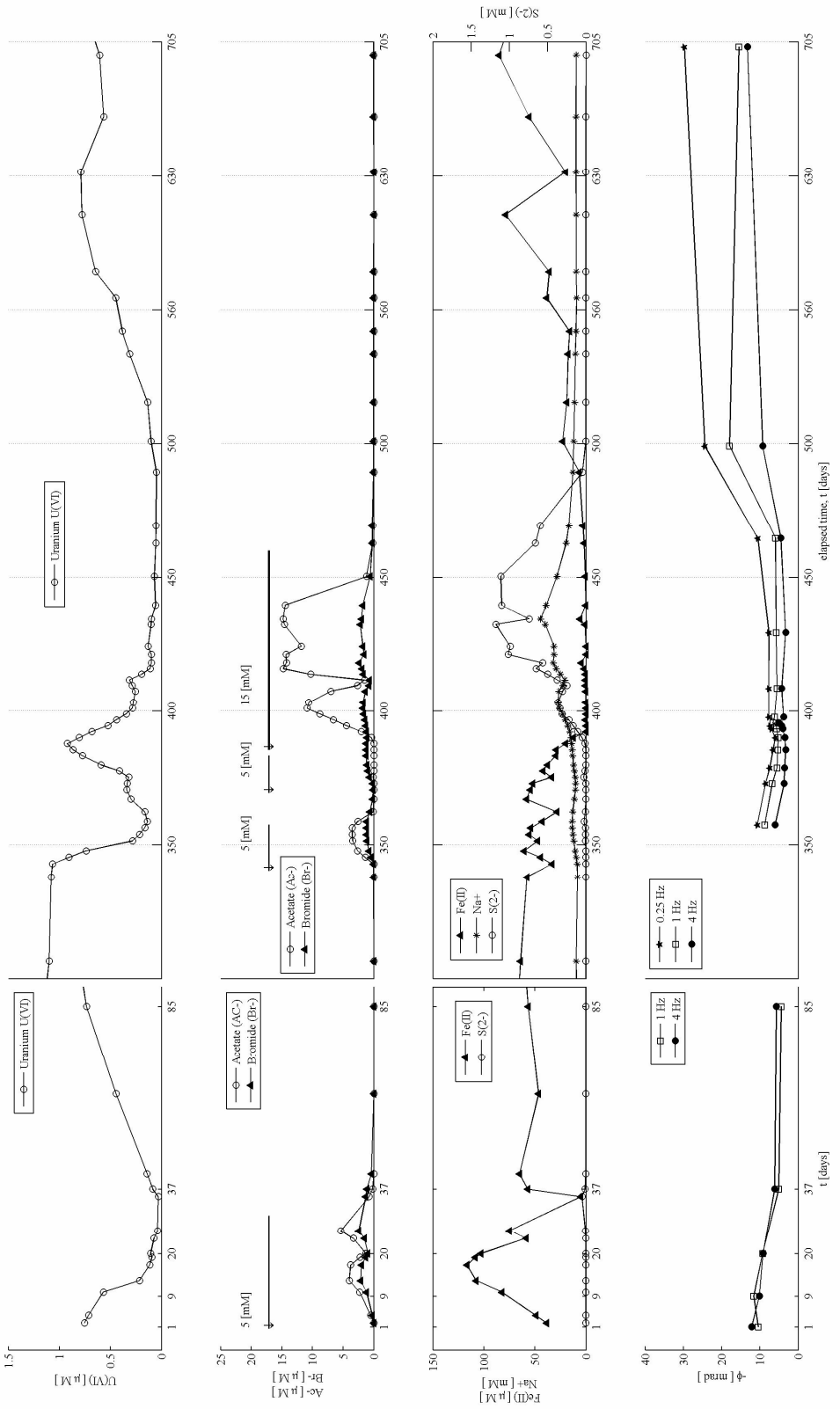

Figure 5.7: Detected concentrations in observation well D-01 of dissolved uranium (U[VI]) (in the first column), acetate (Ac-) and bromide (Br-) (second column), and dissolved Fe(II), S(2-) and Na+ (third column). For comparison the phase values of a selected pixel (in the vicinity of the well D-01) extracted from the inverted images for data collected at different frequencies (fourth column). Elapsed time in days is referenced to the start of acetate injection in 2007.

Period dominated by iron reduction

For all acetate injections performed, a rapid decrease in the concentration of dissolved uranium is observed coincident with a significant decrease in the absolute phase values. As noted, the injection of acetate stimulates the growth of *Geobacter* strains capable of reducing U(VI) to insoluble U(IV) (Anderson et al., 2003; Vrionis et al, 2005; Li et al., 2009). Members of the *Geobacteraceae* grow primarily by enzymatically reducing Fe(III) oxides present in aquifer sediments (Finneran et al., 2002; N'Guessan et al., 2008), resulting in the accumulation of Fe(II) in the vicinity of the mineral grain (Williams et al., 2009):

$$\text{Fe(III)–oxide} + 1e^- \rightarrow \text{Fe(II)}_{aq} \quad (5.8)$$

The increase in Fe(II) just after the amendment injection (e.g., at day 35 and 360 in Figure 5.7) is concurrent with rapid removal of U(VI). Phase images at this time reveal a slight decrease, most probably as a consequence of an increase in the electrical conductivity due to the injection of acetate and bromide.

Periods dominated by sulfate reduction

After day 55, a rapid decrease in dissolved Fe(II) was observed, coinciding with increasing aqueous sulfide ($\sum H_2S$) accompanying the activity of SRB. As the amount or reactivity of available Fe(III) shrinks following prolonged acetate injection, SRB are more readily able to compete for acetate (electron donor):

$$SO_4^{2-} + 8e^- \rightarrow H_2S_{aq} \quad (5.9)$$

The shift to a period dominated by sulfate-reducing conditions can be characterized by less effective removal of U(VI) if acetate levels are lowered to levels insufficient to support continued activity of *Geobacter* strains capable of U(VI)-reduction (Williams et al., 2011).

Precipitation of iron sulfides

During the 2007 experiment, a very short-lived period of sulfate-reduction was observed at later times (day 70). For the 2008 injections, large concentrations of $\sum H_2S$ were observed, which resulted in complete titration of aqueous Fe(II), mainly between days 390 and 490, presumably as iron monosulfides (FeS):

$$\text{Fe(II)}_{aq} + H_2S_{aq} \rightarrow FeS_s \quad (5.10)$$

This period of rapid Fe(II) consumption is characterized by low, but non-zero, absolute phase values (<10 mrad) over all frequencies. The precipitation of new metallic minerals (FeS) within the pore space constitutes an increase in surface area (where induced polarization takes place), thus an increase in the phase response may be expected, as reported for laboratory measurements (e.g., Slater et al., 2005). However, our results reveal a significant decrease in the absolute phase values. We suggest that this decrease could be related to the depletion of electroactive ions (primarily dissolved Fe(II)), the absence of which manifests itself as a lower overall phase response, as suggested by Williams et al. (2009). The importance of electroactive ions in controlling

the polarization magnitude at the metallic interface has been extensively discussed in previous studies (Angoran and Madden, 1977; Wong, 1979; Merriam, 2007).

Post injection

Measurements collected approximately one month after the injection was finished (> 490 days) show a significant increase in the absolute phase values, for all frequencies, with the highest values reported at the lowest frequency (> 40 mrad for data collected at 0.25 Hz). We interpret this large phase response to be a result of further accumulation of metallic sulfides and electroactive ions Fe(II). The high phase values were also observed for measurements collected one year later (day 705) for similar concentrations of dissolved Fe(II) and (presumably) similar enrichments of metallic sulfides (FeS), suggesting that co-occurrence of FeS and Fe(II) engenders the most significant phases anomalies – even in the absence of sustained organic carbon amendment. Such results strongly suggest the value of the complex resistivity monitoring method for tracking the long-term evolution of aquifer redox status following cessation of active biostimulation.

5.5. Discussion

The very different geochemical conditions that accompanied the short- (2007) and long-duration (2008) injection periods yielded characteristic complex resistivity signatures. The low overall concentration of $\sum H_2S$ and minimal decrease in Fe(II) during the 2007 experiment suggest negligible precipitation of metal sulfides, which correlates to minimal changes observed in the phase response. On the opposite, the high concentration of dissolved Fe(II) and $\sum H_2S$ followed by an abrupt decrease of both, e.g., at day 390, suggest the formation of new biominerals (FeS) during the 2008 experiment. While fluctuations in the phase response were observed during the injection period, the large increases in the phase response above pre-injection levels indicate the method's sensitivity to both mineral precipitation reactions and the resultant pore fluid chemistry.

A strong increase in the phase response would be expected accompanying the precipitation of iron sulfides, which are characterized by high surface area and semi-conductive properties. However, the images computed indicate only moderate phase values (absolute values <10 mrad) during the time period when geochemical data suggests that precipitates should be formed, given by low concentrations of Fe(II) and decrease in the concentrations of S(2-). This can be explained by the low concentration of electroactive ions, specifically aqueous and/or sorbed Fe(II). To better highlight this, we present in Figure 5.8 plots of the geoelectrical response against the concentration of the most significant geochemical parameters (i.e., Fe(II) and $\sum H_2S$). Geochemical concentrations were measured in water samples collected in the observation wells along array A (i.e., D-01 to D-04); while the geoelectrical data represent the mean value of a pixel corresponding to the model parameters between 4.5 and 5.5 m bgs and with a width of 1 m (centered at the position of the corresponding observation wells). In the plots of Figure 5.8, it is possible again to see that there is no clear correlation between σ' and changes in the geochemistry of the groundwater. On the opposite, plots of the

phase response (for all frequencies studied) show a strong correlation ($R^2 > 0.94$) where the phase values increase proportionally to the concentration of Fe(II), for concentrations of Fe(II) above a threshold value (50 µM).

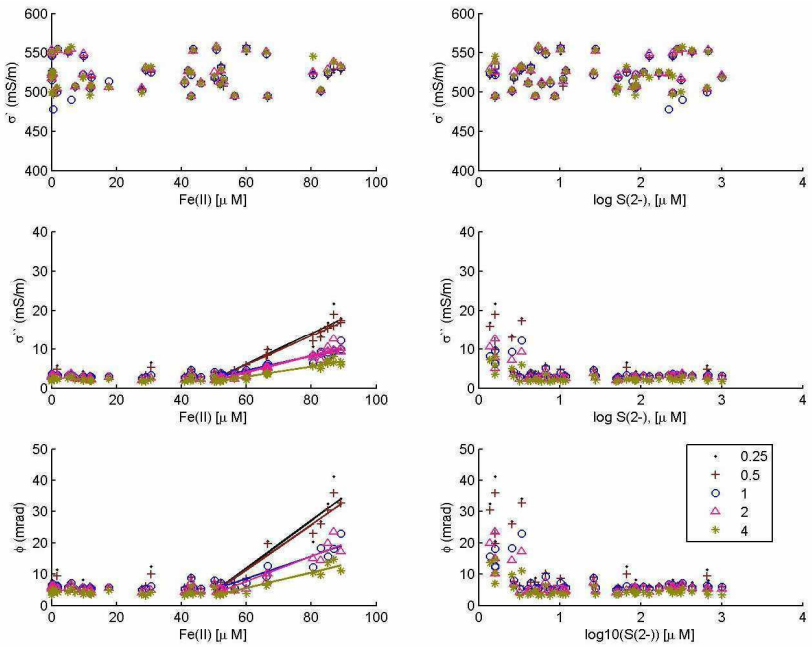

Figure 5.8: Correlation plots between the geoelectrical response and relevant geochemical parameters. Measured concentrations of Fe(II) and S(2-) in the observation wells (D-01, D-03 and D-04) are plotted against the complex conductivity values (real and imaginary components in the first and second plot, respectively, and the phase in the third column). Values of complex conductivity are given by the mean value of a pixel covering the model parameters from 3.5 to 6 m bgs and with an extension of 1 m centered at the position of the corresponding observation wells.

In order to dismiss the effect of changes in the electrical resistivity of the fluid, due to the injections of acetate and bromide, it is important also to look at the imaginary component of the complex conductivity (σ''). Regarding this, plots of Figure 5.8 exhibit also a strong correlation ($R^2 > 0.95$) between σ'' and concentrations of Fe(II), again for Fe(II) concentrations above a threshold value of 50 µM. For the plots corresponding to the concentrations of $\sum H_2S$, it is easy to distinguish a significant decrease in the value of σ'' and phase for concentration of $\sum H_2S$ exceeding 3 µM, independent of the frequency used to perform the measurements. For completeness, the plot of the concentrations of $\sum H_2S$ and Fe(II) is provided in Figure 5.9. As expected, a strong ($R^2 > 0.97$) negative correlation is observed between them, validating the sensitivity of the complex resistivity method to distinguish changes related to variations of the chemical composition of the fluid. The consistent response of the phase and σ'' demonstrates that variations in the subsurface delineated in the phase images are correlated with the induced microbial activities and not with changes in the groundwater conductivity due to the amendment injection.

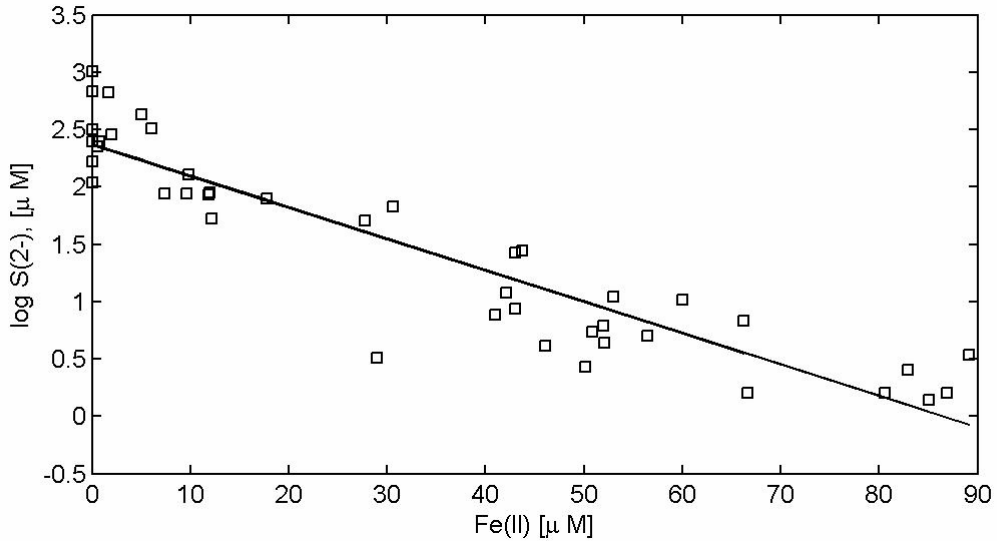

Figure 5.9: Correlation plot of the measured concentration of dissolved Fe(II) and S(2-) in the observation wells along Array A.

Besides the variations in fluid chemistry, the significant decrease in the phase and σ'' values observed for measurements collected during acetate injection might also be a consequence of the extremely small size of the iron sulfides, most probably resulting in a critical frequency (i.e., the frequency at which the maximum phase response is observed) significantly higher than collected in this study. Results from zero-field Mossbauer spectroscopy performed on similar Rifle reduced sediments show abundant iron sulfides in the <53 μm fraction (Qafoku et al., 2009), and freshly precipitated FeS phases during acetate amendment are expected to be very finely particulate, with particle sizes of tens to hundreds of nanometers (Williams et al., 2005). As such, wider frequency-band complex resistivity data are likely necessary to capture a significant response for very fast reactions at the interface between the groundwater and the formed iron sulfide mineral. However, in practice, it is necessary to overcome the problem of unwanted inductive and capacitive coupling noise that commonly corrupts higher frequency complex resistivity field data-sets, which is a current topic of research (e.g., Zimmermann et al., 2008).

In addition, recent studies in column experiments have demonstrated the concurrent precipitation of calcite during acetate injection at Rifle, with the effect being most pronounced during sulfate reduction (Li et al., 2009). Measurements of electrical properties have demonstrated that calcite can act as an insulator for the frequency range studied here (Wu et al., 2009; 2010), suggesting that the low absolute phase values observed in 2008 (days 400-450) may be associated with calcite minerals impeding the contact between the metallic minerals and the electrolyte. Subsequent precipitation of FeS and the accumulation of Fe(II) after the injection is stopped might overcome the insulating effect of calcite precipitation (especially if it is heterogeneously dispersed across mineral surfaces), corresponding to increase in the phase and σ'' values.

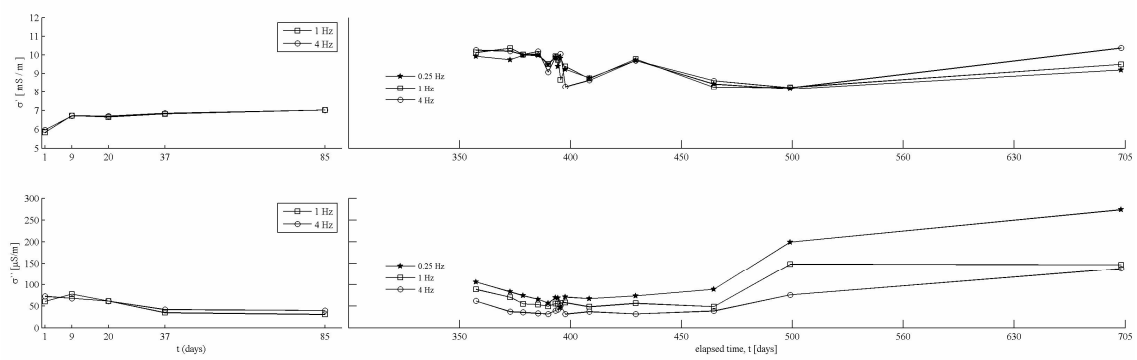

Figure 5.10: Plots of the real (σ', at the top) and imaginary (σ'', at the bottom) components of the complex conductivity. Values are given for a selected pixel close to the observation well D-01. Elapsed time in days is referenced to the start of acetate injection in 2007.

Figure 5.10 presents a modification of Figure 5.7, in order to present the variations of the real (σ') and imaginary (σ'') components of the electrical conductivity for the selected pixel over the two year monitoring period. Looking at variations in the real and imaginary components is particularly useful to distinguish effects related to the growth of biofilms or nanowires as reported in other works (e.g., Atekwana and Slater, 2009, and references therein).

Plots of the real component reveal a significant increase over measurements performed in 2007 compared to those performed in 2008-2009. This is possibly related to mineralogical changes following the 2007 injection, but more likely attributable to the increase in fluid conductivity after the first injection in 2008 due to the higher concentration of acetate injected. It is also important to note that the imaginary component exhibited negligible increase during the 2007 injection experiment. Microbial activity and, hence, growth and cell synthesis was unambiguously stimulated during the 2007 experiment, as predicted (Li et al., 2009) and evidenced by a wide range of biogeochemical data (Mouser et al., 2009; N'Guessan et al., 2009; Elifantz et al., 2010; Williams et al., 2011). Furthermore, analysis of groundwater proteomic samples obtained from wells D-05 and D-07 during the 2007 biostimulation experiment demonstrated a shift in *Geobacter* growth habit from planktonic to attached (Wilkins et al., 2009), indicative of biofilm formation. Laboratory experiments have suggested that an accumulation of cell surfaces following stimulation and growth, as well as the formation of biofilms, can increase in the imaginary component of the complex conductivity of sediments (Ntarlagiannis et al., 2005b; Davis et al., 2006; Abdel Aal et al., 2004; 2010). However, our 2007 complex resistivity monitoring experiments suggest that extension of such laboratory results to the field may be challenging. While the accumulation of cell surfaces and the formation of biofilm structures may impart modest increases in the imaginary component of the complex conductivity signature of subsurface sediments, our results indicate that such effects may be too low to be detected at field-relevant scales (e.g., depths greater than a few meters). In contrast, variations in electroactive fluid composition and precipitation of semi-conductive

minerals of varying surface area can induce large polarization effects that significantly deviate from pre-stimulation values, with such effects readily detectable at field-relevant scales.

5.6. Conclusions

We collected and inverted an extensive time-lapse complex resistivity data-set associated with a bioremediation experiment and interpreted the resulting images through joint consideration of geochemical and microbiological measurements. We illustrated the sensitivity of the inverted images to an appropriate error description and highlighted the impact that varied error descriptions can have on the interpretation of complex resistivity images in terms of biogeochemical processes. The extended data analysis and error description significantly improved the quality of the images over those obtained during previous complex resistivity monitoring experiments at the IRFC Rifle site (Williams et al., 2009).

The improved imaging procedure and extensive long-term data-set facilitated interpretation of the complex resistivity images to a range of biogeochemical initial conditions and remediation-induced processes. For this experiment, the resistivity images alone failed to provide meaningful information about bioremediation-induced processes; the inversion results provided information about baseline heterogeneity but indicated little response over time to the biostimulation. In contrast, the phase images exhibited strong sensitivity to variations in fluid chemistry and the precipitation of semi-conductive minerals, with an important decrease in the response for low frequencies (0.25 Hz) when dissolved iron was depleted from the groundwater, whereas higher frequencies (4 Hz) revealed a detectable increase in the phase response. Post-injection data exhibited very high absolute phase values, suggesting that the iterative precipitation of polarizable minerals (FeS) and accumulation of electroactive species, such as Fe(II), are capable of generating the most pronounced phase anomalies.

Based on our results, and consistent with previous studies (Williams et al., 2005; 2009), we can conclude that electrode polarization (when both metallic minerals and electroactive ions are present) is the principal polarization mechanisms underlying the response observed. A strong correlation is observed between high concentrations of Fe(II) and the imaginary component of the complex conductivity, as well as for the phase, for periods when concentrations of Fe(II) were above a threshold value of ca. 50 μM. For periods dominated by sulfate-reduction, when the concentration of electroactive compounds (e.g., Fe(II) and perhaps other redox-sensitive metals) is below a critical concentration (50 μM for our study), electrode polarization is minimized and other polarization mechanisms, such as electrochemical or membrane polarization, dominate. Such periods are characterized by a moderate phase response (absolute phase values below 10 mrad) in spite of the existence of metallic and clay minerals. A schematic representation summarizing the different conditions enhancing the observed phase response is presented in the Figure 5.11.

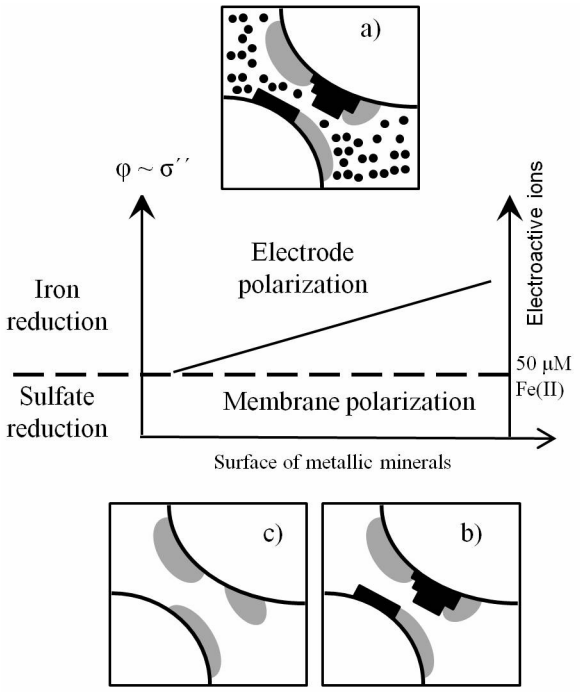

Figure 11: Schematic representation of the polarization mechanisms underlying the observed phase response during the two years of bioremediation monitoring. The solid black structures (e.g., FeS) represent metallic minerals, the gray bodies represent other kind of polarizable minerals (e.g., calcites, clays) and the solid circles represent electroactive ions (e.g., FeII) present in groundwater. Here 3 possible scenarios are considered: (a) Electrode polarization as the dominating polarization process, taking place on the surface of precipitated metallic minerals, characterized by high polarization (σ'' and phase) values if a critical concentration (represented by the dashed line) of electro-active ions (Fe(II) > 50 µM for our experiments) is present in the groundwater. Membrane polarization will be the dominating polarization processes, related to modest σ'' and phase values, for the cases that: (b) metallic minerals have been precipitated but concentration of electroactive ions are lower than the critical concentration (i.e., periods of dominating sulfate reduction in our experiments); and (c) for a negligible amount of metallic minerals.

Complex resistivity monitoring of the studied bioremediation experiments provided a characteristic response for four different processes: (i) delineation of natural bioreduction zones, where uranium is slowly removed from groundwater without amendment injections, characterized by a strong phase response, particularly at the highest measuring frequency; (ii) a noticeable decrease in the phase response (for all studied frequencies) was observed for measurements just after acetate injection during periods dominated by iron-reduction, characteristic of fast rates of uranium removal; (iii) low absolute phase values were observed for periods dominated by sulfate-reduction, characterized by less effective uranium removal; (iv) a significant increase in the phase response was observed for measurements collected after cessation of the amendment injection, consistent with subsequent decrease in dissolved U(VI). The described phase response is also observed for the imaginary component of complex conductivity (σ''), indicating that the processes delineated are not controlled by variations in the fluid conductivity associated with the amendment injection. As such, complex resistivity imaging might be a useful tool to determine when further biostimulation (i.e., resumed injection of organic carbon) is required in order to

maintain conditions favorable for the immobilization of redox sensitive contaminants, such as uranium.

More research is warranted to better understand the observed phase response and the sensitivity of the frequency-dependent response to specific biogeochemical changes (e.g., ion accumulation and depletion, mineral precipitation, etc.). Although microbial activity appears capable of generating large field-scale phase anomalies – with changes in fluid chemistry likely dominating the response – the mechanisms underlying the phase response are still open to debate. Data collection over a wider frequency band is critical for a more accurate understanding of the microbial and chemical processes ongoing during acetate amendment. Inversion of the complex resistivity measurements based on a time- or frequency-regularization scheme might be helpful to increase the resolution and reliability of the final images.

6. TIME-LAPSE SPECTRAL INDUCED POLARIZATION IMAGING OF STIMULATED URANIUM BIOREMEDIATION[4]

6.1. Abstract

Tomographic measurements of spectral induced polarization (SIP) were conducted at the U.S. Department of Energy's (DOE) Integrated Field Research Challenge site (IFRC) in Rifle, Colorado (USA), where biostimulation research is ongoing with the purpose to immobilize uranium in tailings-contaminated groundwater. The aims of the SIP surveys were to (a) collect data over a sufficiently broad bandwidth so as to determine the characteristic frequency of the spectral response, (b) investigate the distribution of spectral parameters (e.g., characteristic time constant) in an imaging framework, and (c) evaluate the potential of these images to delineate changes in the hydraulic properties of the aquifer. Careful field procedures provided high quality SIP data from 0.060 to 256 Hz for three different periods during the remediation experiment. Data quality was evaluated by means of analysis of the discrepancy between normal and reciprocal measurements. A Cole-Cole model was fitted to pixel values extracted from the inverted images in order to assess changes in SIP responses – particularly, in time constant (τ) and in chargeability (m) - due to processes accompanying the stimulation of subsurface microbial activity. We observed an important decrease in m and a minimal increase in τ once acetate injection commenced, which was well correlated with depletion of aqueous iron (Fe(II)) in a period characterized by high rates of iron- and sulfate-reduction. A significant increase in both τ and m was observed after halting acetate injection, consistent with the accumulation of semi-conductive minerals (e.g., FeS) during biostimulation and the post-injection rebound in aqueous Fe(II).

6.2. Introduction

The complex resistivity method has emerged as a promising tool for the characterization of hydraulic and environmental parameters in the near surface (e.g., Kemna et al., submitted to *Near Surface Geophysics*). This is given to the fact that complex resistivity measurements can provide information on the low-frequency conduction (i.e., resistivity method) and capacitive (i.e., induced polarization) properties of sediments (e.g., Lesmes and Frye, 2001; Lesmes and Morgan, 2001). Although an adequate interpretation of the induced polarization response remains challenging (e.g., Binley and Kemna, 2005;

[4] Flores Orozco, A., Williams, K.H., and Kemna, A. 2011. Time-lapse spectral induced polarization imaging of stimulated bioremediation: Near Surface Geophysics, submitted

Revil and Florsch, 2010), three main mechanisms have been found to control the polarization of bacteria-free and metal-free sediments: the so-called membrane polarization taking place through the constriction of the pore space, particularly in the presence of clay minerals, and the formation of ion selective zones (completely described in, e.g., Marshall and Madden, 1959; Ghorbani et al., 2008); the polarization of the electrical double layer (EDL) coating grain minerals (described in detail in Leroy et al., 2008; Revil and Florsch, 2010); and the Maxwell-Wagner polarization, taking place at high frequencies (> 100 Hz) at the interfaces of materials with different dielectric properties (e.g., Chen and Or, 2006; Leroy et al., 2008). Based on measurements performed at different frequencies (commonly referred to as spectral induced polarization, SIP), experiments conducted on metal-free sediments have revealed, for instance, a correlation between the polarization response and saturation (e.g., Titov et al., 2004; Ulrich and Slater, 2004), and with the growth and accumulation of microbial cells (e.g., Ntarlagiannis et al., 2005a; Abdel Aal et al., 2006; Atekwana and Slater, 2009). Moreover, recent studies have demonstrated a relationship between the length scale controlling groundwater flow and the length scale at which the polarization takes place (e.g., Kemna, 2000; Titov et al., 2002; Binley et al., 2005; Slater, 2007; Revil and Florsch, 2010). However, to date remarkably few studies have been conducted at the field scale to validate such inferences.

SIP measurements have traditionally been used in the geophysical exploration of sulfide ores (e.g., Marshall and Madden, 1959; van Voorhis et al., 1973; Pelton et al., 1978; Wong et al., 1979) due to the strong polarization response observed in presence of metallic minerals (e.g., iron sulfides like pyrite). The so-called electrode polarization is caused by changes in the charge transfer mechanisms from ionic (in the pore water) to electronic (in the metallic mineral) through redox reactions taking place at the interface between pore water and the surface of metallic minerals (e.g., Sumner, 1976; Pelton et al., 1978; Wong et al., 1979; Merriam, 2007; Revil and Cosenza, 2010). It has been demonstrated that the measured response in the low frequency (< 100 Hz) enhanced through electrode polarization is significantly larger than the polarization response of subsurface materials due to other polarization mechanisms (e.g., Pelton et al., 1978; Wong, 1979; Williams et al., 2005; Slater et al., 2006; Weller et al., 2010). Moreover, it has been observed that the critical frequency (at which the strongest polarization effect is observed) can be correlated to the size, volume, and texture of the metallic minerals (e.g., Pelton et al., 1978; Wong, 1979, Slater et al., 2007).

Recent laboratory studies have also demonstrated the sensitivity of SIP measurements to the precipitation of sulfide minerals accompanying the stimulation of microbial activity (Williams et al., 2005), and to changes in the spatiotemporal location of the minerals (Ntarlagiannis et al., 2005b). Analysis of the spectral response has been used to quantify the grain size of precipitated metallic minerals (Slater et al., 2006) and reversible reactions (i.e., possible oxidation and dissolution of precipitated minerals) (Slater et al., 2007). Taking these laboratory results into account, and given the possibility of measuring SIP in an imaging framework in conjunction with complex

resistivity inversion schemes (Kemna et al., 2000; Kemna et al., 2004), SIP imaging has been applied at the field scale to monitor microbial activity in the course of bioremediation experiments (Williams et al., 2009; Flores Orozco et al., 2011). Here, the method has been successfully used to delineate the accumulation of sulfide minerals (Williams et al., 2009), as well as the redox status of aquifer materials (Flores Orozco et al., 2011) accompanying stimulation of subsurface microbial activity. Although encouraging, these field studies have failed to collect data over a frequency bandwidth broad enough to determine the characteristic frequency of the spectral response. However, this is necessary given the observed link between the critical frequency of the SIP response and a characteristic length scale of pore space geometry (e.g., Pelton et al., 1978; Wong, 1979; Titov et al., 2002; Binley et al., 2010; Revil and Florsch, 2010).

Acquisition of SIP tomographic measurements over a broad frequency bandwidth at the field scale is very challenging because of three primary issues: (i) errors in the voltage measurements due to polarization of the electrodes used previously for current injection, especially for measurements at low frequencies (< 10 Hz) (e.g., Dahlin et al., 2002; LaBrecque and Daily, 2008); (ii) unwanted electromagnetic contamination of the data, i.e., inductive coupling (increasing with frequency and electrode separation) and capacitive coupling associated with the wire layout (Pelton et al., 1978; Zimmermann et al., 2008); and (iii) long acquisition times required to collect data at low frequencies (< 1 Hz), with data acquisition between tens of electrodes taking several hours. Hence, it is important to deploy an adequate measuring protocol (with the minimal number of independent measurements) and careful field procedures for the collection of reliable SIP data over a wide range of frequencies.

In this study we present SIP imaging results covering a frequency bandwidth which permitted the computation of Cole-Cole spectral parameters, particularly the time constant associated with the characteristic frequency. Changes in time-lapse images of Cole-Cole parameters were found in agreement with variations in groundwater chemistry and precipitation of metallic minerals (e.g., monosulfides, FeS). To our knowledge, this is the first field study presenting time-lapse SIP data collected over such a wide frequency bandwidth and able to solve for the critical frequency of the SIP response for different time-lapses.

In the next section, we present a brief description of the study area and the experimental set up, followed by a short summary of the specifications of the employed SIP imaging procedure and the Cole-Cole model, after which we present and discuss our results, and close with concluding remarks regarding prospects for future studies.

6.3. Methods

The Department of Energy (DOE) Rifle Integrated Field Research Challenge (IFRC) site is located near Rifle, Colorado (USA), on the grounds of a former uranium processing facility. Here, biostimulation via acetate injection has repeatedly been performed to reduce and immobilize U(VI) in a shallow and unconfined alluvial aquifer (Williams et al., 2011, and references therein). The site is characterized by a clay-rich

fill which extends from the surface to ~1.75 m below ground surface (bgs) and which overlies the unconfined aquifer. Aquifer material consists of unconsolidated sands, silts, clays, and gravels, which is underlain by an impermeable layer of silt- and mudstones comprising the Wasatch formation at a depth of ca. 6.5 m (bgs). The groundwater table was located at ~3.5 m (bgs) during the experiment, with groundwater velocities in the range from 0.1 - 0.6 m/day, and with flow direction toward the southwest. A complete description of the site can be found elsewhere (Williams et al., 2011, and references therein).

Site groundwater was amended with sodium acetate (in situ target concentrations of 15 mM) and sodium bromide (in-situ target concentration of 1.3 mM) and injected to the aquifer over the course of 36 days using ten injection boreholes. Fifteen observation wells were used to collect groundwater samples for geochemical analysis throughout the experiment: three upgradient and twelve downgradient from the area of injection (Figure 6.1). All wells were emplaced to an average depth of 6.5 m (~0.3 m into the Wasatch formation), with a diameter of 10.1 cm and screened (250 μm slot size) over the lower 3 m depth interval (for a complete description see Williams et al., 2011). SIP measurements were collected along two arrays: array A, placed 3 m down-gradient the injection gallery and perpendicular to groundwater flow direction; and array Y, placed parallel to groundwater flow direction and intersecting the injection gallery and array A (at 14 m and 17 m respectively along the direction of array Y), as depicted in Figure 6.1. Measurements along array A were collected one day before amendment injection (hereafter referred to as *t0*), 19 days after injection has been started (hereafter referred to as *t1*), and two days after the injection was stopped (hereafter referred to as *t2*). Measurements along array Y were collected only three days after the injection was stopped (hereafter referred to as *t3*). For data collection, 30 $Cu/CuSO_4$ non-polarizing electrodes were placed at the surface with a separation of 1 m between them. Measurements were collected over the frequency range from 0.06 to 256 Hz by means of a dipole-dipole configuration with a "skip-3" protocol, resulting in a dipole length of 4 m for current and potential dipoles (i.e., current injection performed, for example, between electrodes 1 and 5 and potential measurements between electrodes 6 and 10, 10 and 14, etc.), with a maximal length of 21 m between the current and potential dipoles. The selection of an appropriate measuring protocol plays a significant role regarding the resolution of the images and it has been the issue of several works (e.g., Bing and Greenhalgh, 2000; Stummer et al., 2004); however, we avoided the data acquisition with potential electrodes placed inside the current dipole to reduce electromagnetic effects in the data. We opted for this measuring protocol ("skip-3") also to better compare our results with those observed in previous studies performed at the site, and because such measuring protocol has demonstrated a satisfactory resolution in the images for the intended investigation depth (~6 m bgs) and reasonable acquisition times (~12 hours for a complete data set in the frequency range studied here). A Zonge GDP32(II) with 15 channels was used to perform the measurements, with coaxial cables connecting the electrodes with the receiver, in order to reduce electromagnetic coupling effects, as investigated in the study of Zimmermann et al. (2008) for tomographic

measurements in the laboratory.

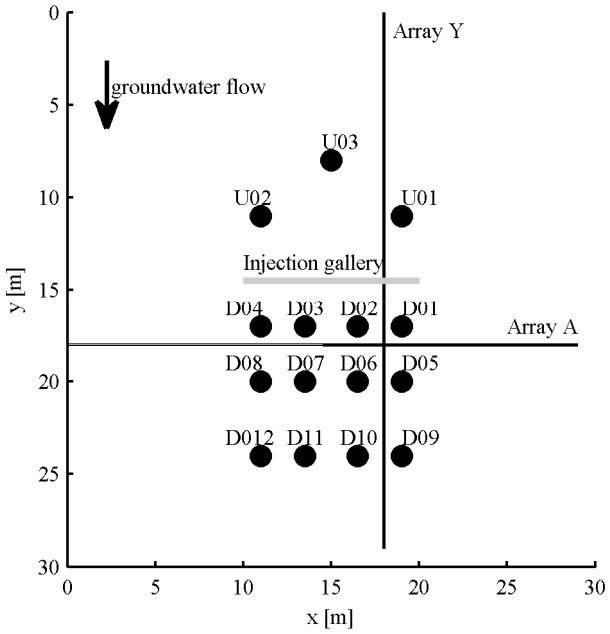

Figure 6.1: Schematic plan view of the experimental setup for the 2009 experiment at the Rifle IRFC site. The position of the observation wells up-gradient (open triangles: U01-U03) and down-gradient (solid triangles: D01-D12) of the injection gallery (gray thick line) are referred to the direction of the groundwater flow (solid arrow). The solid lines represent the location and extent of the arrays A and Y, with the electrode positions marked with solid circle. All the dimensions are given in meters.

Complex resistivity images for our study were obtained using the smoothness-constraint inversion code CRTomo (completely described in Kemna, 2000). The algorithm calculates the complex resistivity distribution on a 2D grid of lumped finite-element cells from a given data set of transfer impedances (Z_i, i = 1, …, N; with N being the number of measurements), at a given frequency. The inversion algorithm iteratively minimizes an objective function, which is composed of the measures of data misfit and model roughness, with both terms being balanced by a regularization parameter. More details on the inversion scheme and the underlying modeling algorithm are given in Kemna (2000). Inversion of multi-frequency measurements in this study was performed by the independent inversion of data sets collected at each acquisition frequency.

A proper quantification of the data error plays a critical role regarding the quality of the final images (LaBrecque et al., 1996). In our study, data errors have been evaluated in terms of discrepancy between normal and reciprocal measurements, which has become a common practice to assess data quality in tomographic measurements (e.g., Slater and Binley, 2006). For the inversion of resistance data, a linear model in function of the measured resistances, R (i.e., signal strength), was used to estimate the data error, $s(R)$, as outlined by LaBrecque et al. (1996); meanwhile phase data-error, $s(\phi)$, was quantified by a power-law function of resistance, which improves the resolution of phase images (Flores Orozco et al., 2011). The parameterization of the error models was performed by means of statistical analysis of a set of resistance ranges, as described in Flores

Orozco et al. (*submitted to Geophysics*).

Complex resistivity (ρ) (or complex conductivity, σ, $\sigma = 1/\rho$), measured in SIP, can be expressed either in terms of magnitude ($|\rho|$) and phase (ϕ) or in terms of real (ρ') and imaginary (ρ'') components. In order to describe the spectral response, it is common to use the empirical Cole-Cole model (Cole and Cole, 1941; Pelton et al., 1978; Wong, 1979):

$$\rho(\omega) = \rho_0 \left[1 - m \left(1 - \frac{1}{1 + (i\omega\tau)^c} \right) \right], \tag{6.1}$$

where $i^2 = -1$, ω denotes the angular frequency, ρ_0 the dc resistivity, m the chargeability, c is the frequency exponent describing the strength of the dispersion, and τ is the time constant (inversely related to the critical frequency). Previous studies have demonstrated that, for polarization associated with metallic mineral particles, an increase in particle size is related to an increase in τ and a decrease in m, while an increase in the volume of metallic minerals is related to an increase of τ and m (Pelton et al., 1978; Wong, 1979; Williams et al., 2005; Slater et al., 2007). Cole-Cole model parameters were in this study quantified using the non-linear Levenberg-Marquardt inversion routine by Kemna (2000).

Recent studies have demonstrated a better fit of spectra with arbitrary shapes through the superposition of a number of Debye models (simplification of the Cole-Cole model with $c = 1$ in Equation 6.1) for SIP measurements collected on different samples at the laboratory scale (e.g., Morgan and Lesmes, 1994; Nordsiek and Weller, 2008; Weller et al., 2010; Zisser et al., 2010). This approach, referred to as Debye decomposition (DD), assumes that the SIP response is the result of the superposition of different polarization effects taking place at different length scales (Morgan and Lesmes, 1994). Images of Cole-Cole parameters computed through a DD as outlined in Zisser et al. (2010) resulted in rough images strongly affected by numerous artifacts (data not shown), most probably related to the fact that each pixel (finite-element cell) was analyzed separately, without any coupling between adjacent cells. We also want to remark that tomographic measurements as those here presented are associated with uncertainties associated with data acquisition (i.e., field conditions in comparison to well controlled conditions in the laboratory) and uncertainties associated with the inversion; in addition to this, taking into consideration the larger number of measurements required in tomographic surveys (i.e., longer acquisition times), laboratory measurements are typically performed with a larger number of frequencies than those collected at the field scale. Regarding these issues, we opted for the superposition of two Cole-Cole terms to describe the SIP observed in our studies, one for the description of the low-frequency response and a second one to account for the electromagnetic effects at higher frequencies, as performed in previous studies addressing the analysis of SIP responses of sediments containing metallic minerals (e.g., Pelton et al., 1978; Kemna et al., 2000; Slater et al., 2007).

6.4. Results

6.4.1. Raw data analysis

Analysis of the SIP measurements revealed agreement between normal and reciprocal measurements for data collected in the frequency range between 0.06 and 216 Hz (as presented in Figure 6.2), an increase of two decades in the frequency bandwidth in comparison to previous studies at the site (Williams et al., 2009; Flores Orozco et al., 2011). Moreover, SIP measurements reveal a frequency-dependent response, with apparent (i.e., measured) spectra characterized by a frequency peak in the low frequencies (< 32 Hz). In Figure 6.3 we present plots of the standard deviation between normal and reciprocal phase measurements ($s(\Delta\phi)$) computed for each data set (collected at different frequency and time-lapse).

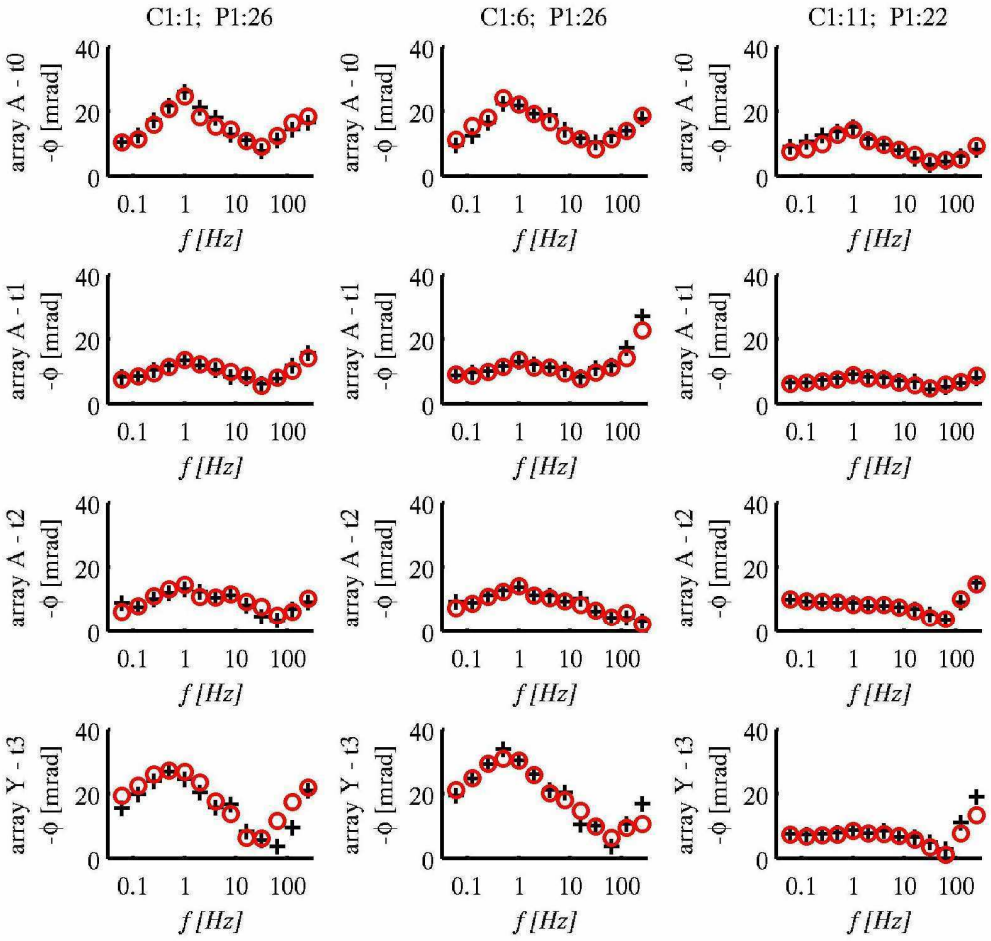

Figure 6.2: Phase measurements collected along array A (the first three columns) and array Y (the last column) for selected dipoles. The black and red symbols represent normal and reciprocal measurements respectively.

Plots in Figure 6.3 reveal variations in the $s(\Delta\varphi)$ for data sets collected at different frequencies, as observed in previous studies (Kemna et al., 2000; Flores Orozco et al., 2011); hence we performed the inversion of data sets collected at different frequencies with individual error parameters. However, the computed $s(\Delta\varphi)$ exhibited a relatively

constant value for measurements collected at the same frequency but at different time-lapses (in array A); hence we used the averaged error parameters to invert different time-lapse data sets collected at the same acquisition frequency (in array A). High acquisition frequencies (i.e., 64, 128, and 256 Hz) reveal a constant increase in the measured phase values with increasing the acquisition frequencies, as well as an increase in the normal-reciprocal misfit $s(\Delta\varphi)$. This is most probably related to electromagnetic (EM) coupling in the data and possible inferences of the 60 Hz AC (alternating current) electric power supply. Although some approaches have been proposed to model the EM response through the geometry of the cables connecting the electrodes to the receiver (e.g., Dahlin et al., 2002, and references therein), in our study EM effects in the data were removed before the inversion, through the subtraction of a second Cole-Cole term accounting for the peak observed at higher frequencies (> 32 Hz), as outlined by Pelton et al. (1978), and performed in an imaging framework by Kemna (2000) and Kemna et al. (2000). To better focus on the SIP response of the aquifer sediments, we will present and discuss in this study only the results obtained for data collected at low frequencies (< 32 Hz), where EM-induced effects are generally assumed to be negligible.

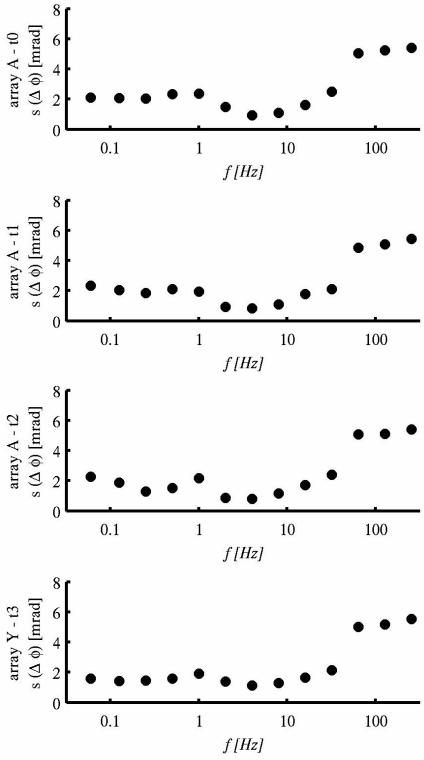

Figure 6.3: Computed standard deviation of the normal and reciprocal misfit ($s(\Delta\varphi)$), in mrad) for data sets collected at different frequencies along array A (the first three columns) and array Y (the last column).

6.4.2. Imaging results

For completeness, we present in Figure 6.4 the computed images of the complex conductivity (σ) for background data collected at 0.125 Hz along array A, as well as a representative lithological column of the site for comparison. The image of the real component of the complex conductivity (σ') shows agreement with the site lithology given by four main units: the clay-rich fill on top, the unsaturated and saturated alluvial sediments, and the impermeable layer from the Wasatch formation at the bottom, as depicted in Figure 6.4. The image of the imaginary component (σ'') shows also consistency with the given lithology; however, an anomaly is noticeable at ~15 m (along array direction) characterized by high σ'' values, related to the presence of metallic minerals precipitated in previous experiments (Qafoku et al., 2009; Flores Orozco et al., 2011; Williams et al., 2011).

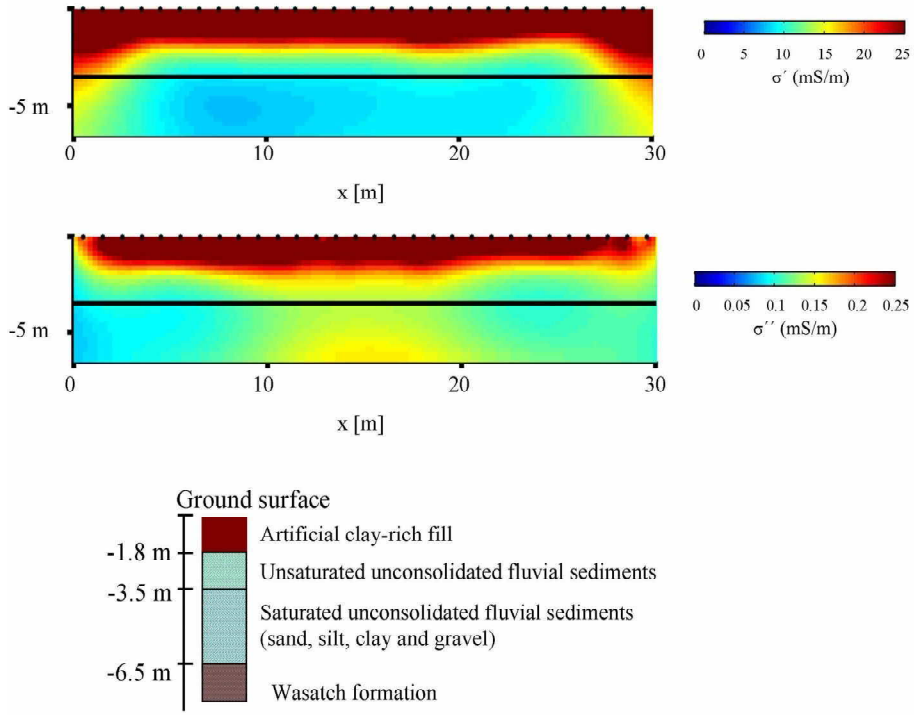

Figure 6.4: Images of the real (top) and imaginary (center) components of the complex conductivity for background data collected at 0.125 Hz in array A. The depth of the water table is marked for each image (solid black line), as well as the position of the electrodes at the surface (black points). On the bottom, a representative lithologic column of the site is given for comparison.

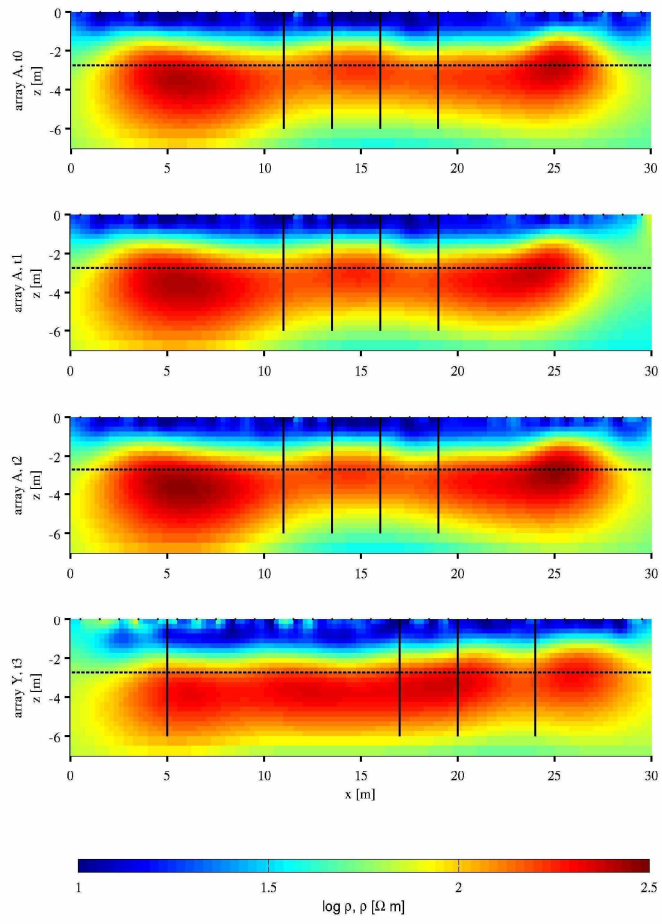

Figure 6.5: Resistivity magnitude images for measurements collected in array A and Y. The depth of the water table is marked for each image (dashed line), as well as the position of the electrodes at the surface (black points). Solid black lines indicate the location of observation wells D-04, D-03, D-02, and D-01 (from left to right) for array A; and U-01, D-01, D-05, and D-09 for array Y (from left to right).

Images of resistivity magnitude, and hence of the real component of the complex resistivity (considering that $|\rho| \approx \rho'$), show only modest variations with measurement frequency and only minor changes between measurements collected at different periods of the biostimulation (Figure 6.5). Meanwhile resistivity phase images show considerable changes in the frequency response (as presented in Figure 6.6), for different periods during biostimulation (array A) and at different locations (array Y), in agreement with previous studies (Williams et al., 2009; Flores Orozco et al., 2011).

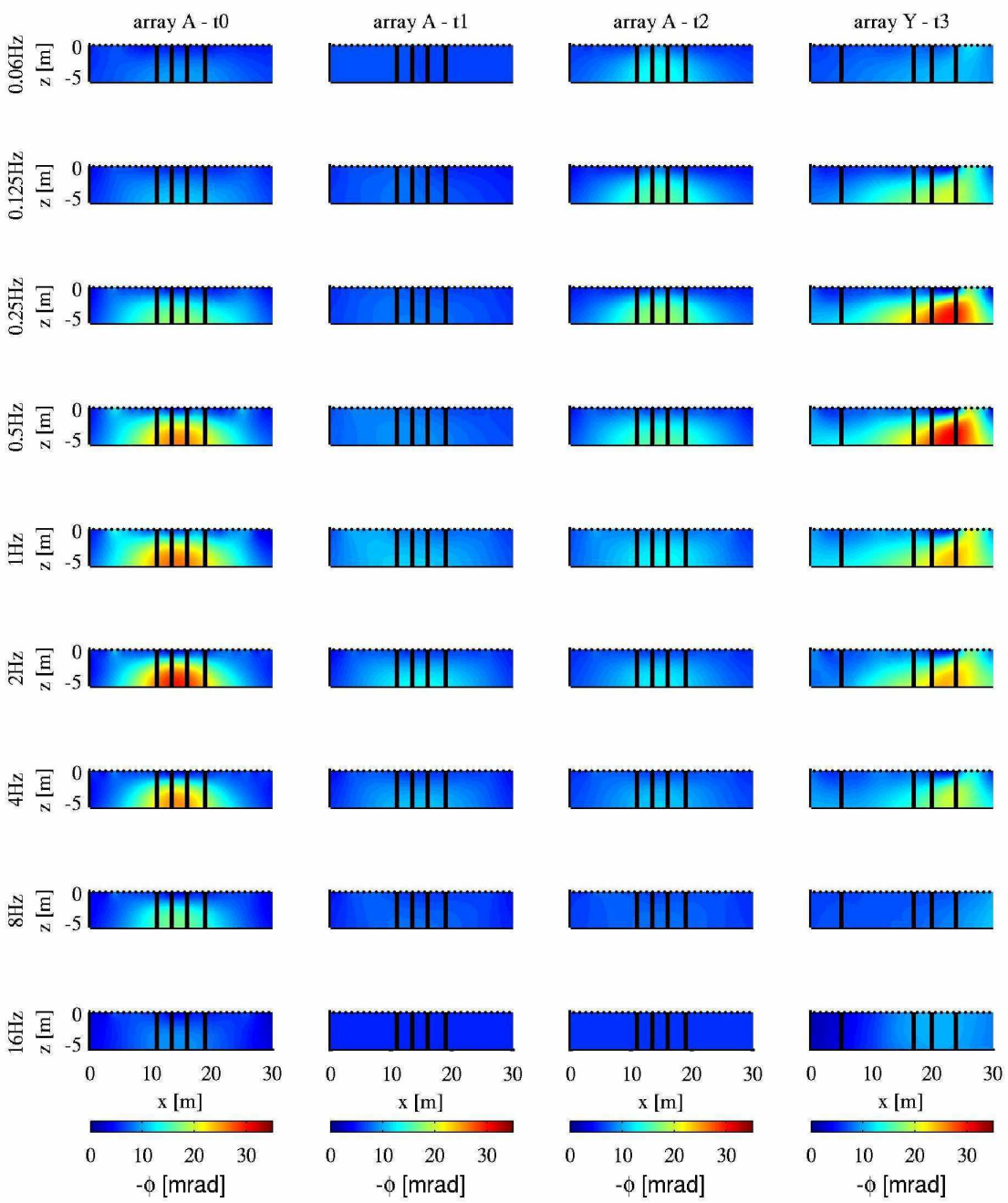

Figure 6.6: Resistivity phase images for measurements collected in array A and Y. The position of the electrodes at the surface is marked at the top for each image (black points). Black lines indicate the location of observation wells D-04, D-03, D-02, and D-01 (from left to right) for array A; and U-01, D-01, D-05, and D-09 for array Y (from left to right).

6.4.3. Geochemical interpretation of SIP images

Table 6.1 presents a summary of relevant geophysical and geochemical (i.e., concentrations of dissolved uranium (U(VI)), acetate, aqueous iron (Fe(II)), and total dissolved sulfide (ΣH_2S)) parameters observed at different periods in array A and at different locations along array Y. For array A, we present concentrations of geochemical parameters measured in water samples collected in the observation well D-03, where the highest changes in phase images were observed (Figure 6.6), as well as

the τ and m parameters obtained from fitting the Cole-Cole model to the multi-frequency pixel values of the images in the vicinity of the observation well D-03 (between 4 and 6 m bgs and between 14 and 15 m along the direction of the array). Analogously, for array Y we present geochemical concentrations measured in wells U-01, D-01, D-05, and D-09 and their corresponding Cole-Cole parameters (i.e., between 4 and 6 m bgs, and 11-12; 17.5-18.5; 20-21; and 24-25 m along the direction of the array Y). Table 6.1 also provides the computed root-mean-square error (RMSE), representing the difference in the phase values between the fitted Cole-Cole model and those extracted from the inverted images (for inversion results up to 32 Hz).

Array A [D-03]

	pre-injection	**injection**	**post-injection**
ρ [Ωm]	150	119	141
τ [s]	0.123	0.108	0.896
m [-]	0.081	0.038	0.082
RMSE	1.5	1.1	0.9
Acetate [mM]	0.0	5.9	0.8
U(VI) [µM]	0.8	0.3	0.3
Fe(II) [µM]	66.2	9.9	30.9
$\sum H_2S$ [µM]	9	762	92

Array Y [after stopping the amendment injection]

	U-01	**D-01**	**D-05**	**D-09**
ρ [Ωm]	152	110	102	105
τ [s]	0.23	0.69	0.33	0.31
m [-]	0.033	0.092	0.086	0.087
RMSE	2.1	2.3	1.9	2.2
Acetate [mM]	0	1.1	1.6	0.9
U(VI) [µM]	1.1	0.2	0.4	0.7
Fe(II) [µM]	2.5	59.1	7.2	58.9
$\sum H_2S$ [µM]	11	5	685	9

Table 6.1: Comparison of geochemical and Cole-Cole parameters observed along array A and array Y.

Figure 6.7 shows the spectral response of the resistivity phase (ϕ) for the selected pixel of array A for the different time-lapses (left side) and for the pixels extracted at different locations along array Y (right side). Although some discrepancies can be found between the observed phase response and the fitted Cole-Cole model response, the spectra are fairly well recovered, in particular with respect to the position (τ) and amplitude (m) of the phase peak, with computed RMSE values of the fitted models (as presented in Table 6.1) in range of the observed normal-reciprocal misfit ($s(\Delta\varphi)$) in the data collected at frequencies below 64 Hz (as presented in Figure 6.3).

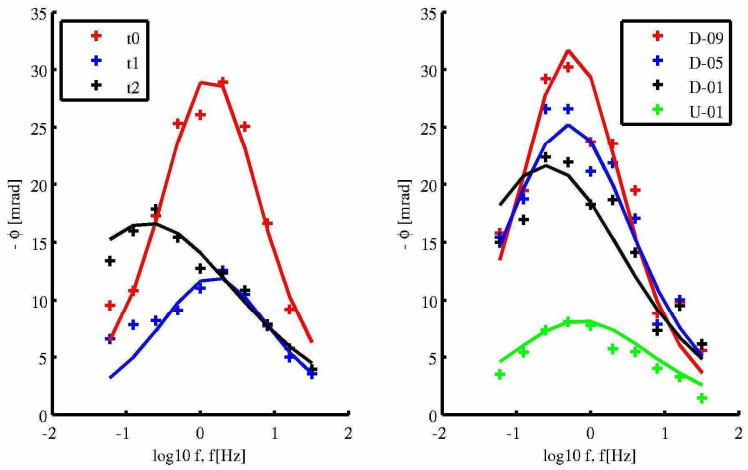

Figure 6.7: Spectral response of selected pixels. On the left: phase values extracted (crosses) from the inverted images of array A at the location of well D-01, for data collected before the amendment injection (*t0*), during the injection (*t1*), and after cessation of the amendment injection (*t2*). On the right: phase values extracted (crosses) from the inverted images of array Y at the location of wells U-01, D-01, D-05 and D-09 at time *t3*. The solid lines represent the responses of the Cole-Cole models fitted to the phase values, based on the parameters presented in Table 6.1. The computed root-mean-square error (RMSE) between phase values extracted from SIP images and the fitted Cole-Cole model response are presented in Table 6.1.

In order to better evaluate the distribution of spectral (i.e., Cole-Cole) parameters and their correlation with spatiotemporal changes in the subsurface accompanying the biostimulation processes, we fitted a Cole-Cole model to all pixel values for the resistivity and phase images. Figure 6.8 shows the resulting images for the Cole-Cole parameters ρ_0, τ, and m for both arrays. Images of array A in Figure 6.8 reveal a slight decrease in the resistivity values (ρ_0) in the injection area during the biostimulation (*t1*), most likely related to an increase in groundwater electrical conductivity due to the injection of acetate and bromide. Moreover, this period is characterized by a rapid decrease in the concentration of dissolved uranium (U(VI)), coincident with a significant decrease in the absolute phase values (Figure 6.5), as also observed in previous experiments (Williams et al., 2009; Flores Orozco et al., 2011). Acetate stimulates the growth of *Geobacter* strains through enzymatic reduction of iron oxides present in aquifer sediments, resulting in an initial increase in aqueous Fe(II). Both, subsequent and concurrent to this, the stimulation of sulfate reducing bacteria results in the accumulation of aqueous sulfide ($\sum H_2S$). Increasing concentrations of $\sum H_2S$ results

the titration of dissolved Fe(II) and the precipitation of iron sulfides (e.g., FeS). However, only a minimal change in the τ values can be observed for baseline data (*t0*) and data collected during injection (*t1*), due to the precipitation of metallic minerals. Nevertheless, a significant decrease is observed in the *m* values, most probably as a consequence of the increase in the electrical conductivity due to the amendment injection and the depletion of electroactive ions (Fe(II)) (as presented in Table 6.1), as suggested in previous works (Angoran and Madden, 1977; Williams et al., 2005; 2009; Flores Orozco et al., 2011). Images for data collected after cessation of amendment injection (*t2*) in Figure 6.8 show that resistivity values (ρ_0) increased again and are similar to baseline values; additionally, an increase in *m* values is also revealed, likely related to a slow increase in the concentration of electroactive ions (Fe(II)) once that the acetate injection has been ceased, as presented in Table 6.1. Moreover, a significant increase in τ values is noticeable, above baseline values, as predicted by the model proposed by Wong (1979), due to the precipitation of metallic minerals, such as monosulfides (FeS). A complete description of the geochemical analysis and results of groundwater sampling, as well as of the microbiological and geochemical processes taking place through the acetate injection, is provided in the study of Williams et al. (2011).

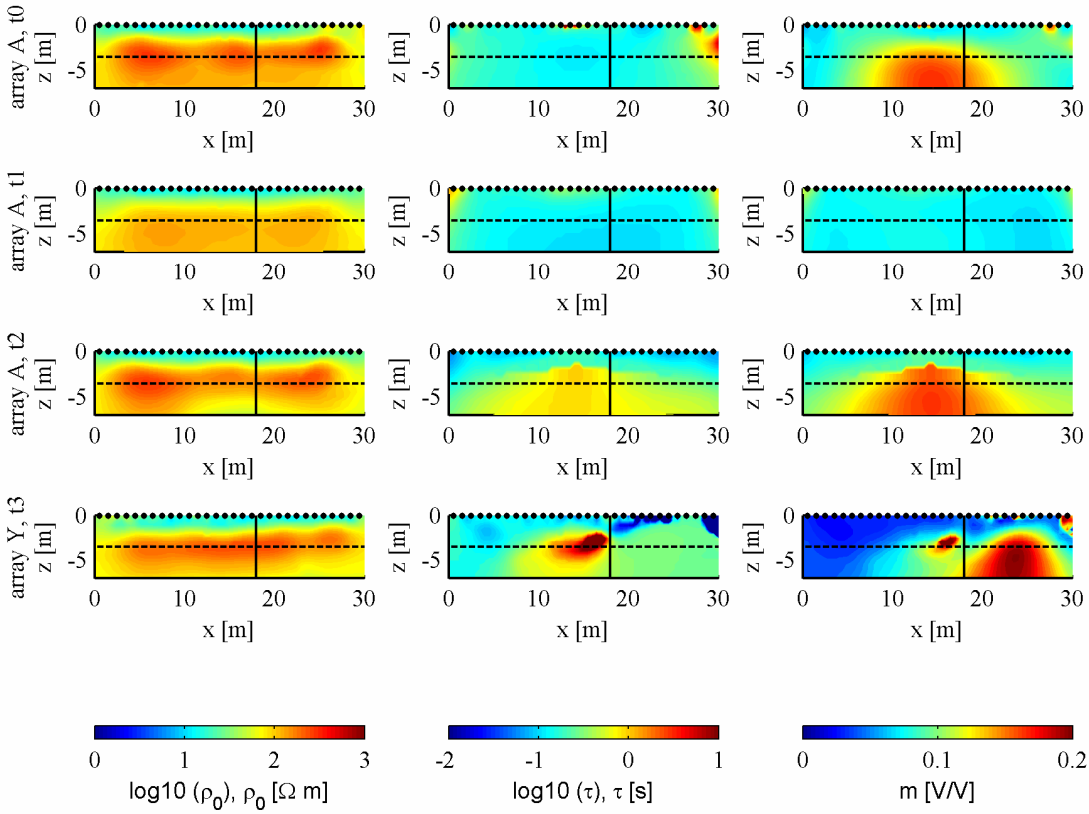

Figure 6.8: Images of Cole-Cole parameters computed for pixel values extracted from the inverted images of array A and Y, for data collected before the amendment injection (*t0*), during the injection (*t1*), and after cessation of the amendment injection (*t2*). The depth of the water table is marked for each image (dashed line), as well as the position of the electrodes at the surface (black points). The solid line indicates the position at which array A and array Y overlap.

Images for array Y reveal spatial changes consistent to temporal variations observed in array A for different periods of the biostimulation (i.e., at different groundwater geochemical composition). Plots in Figure 6.8 reveal high τ and m values at the center of the image (where the injection gallery is located), likely due to the precipitation of metallic minerals and the slow accumulation of electroactive ions (i.e., Fe(II)), which are consistent with values observed in array A for measurements collected after stopping the amendment injection (*t2*). A sharp contrast in array Y is noticeable at ~19 m (along array direction), where low values of τ and m are exhibited, similar to those observed in array A during the amendment injection (*t1*) – a period characterized by high rates of microbial activity and low concentrations of electroactive ions (Table 6.1). Another anomaly is revealed for distances further than ~22 m (in the direction of array Y), characterized by low values of τ, but high values of m, likely related to ongoing mineral precipitation concurrent with higher rates of electroactive ions (Table 6.1).

Although recent studies have demonstrated that measurable SIP responses can arise due to the accumulation of biofilms and microbial cells (Atekwana and Slater, 2009, and references therein), such effects are related to very modest phase values ($|\phi| < 2$ mrad) in comparison with the typical response associated with polarization due to metallic minerals ($|\phi| > 20$ mrad) (e.g., Ntarlagiannis et al., 2010). As such, phase anomalies associated with biological processes other than biomineralization may be difficult to detect at the field scale, with any response overwhelmed by changes in pore fluid chemistry and precipitation of metallic minerals (Flores Orozco et al., 2011). For this reason, we intentionally restrict our interpretation of the anomalous SIP responses to charge transfer processes associated with biomineralization and temporal variations in pore fluid composition.

Based on the time-lapse images computed for τ, we might estimate the change in the characteristic length scale accompanying the precipitation of metallic minerals by means of an established relationship between the relaxation time (τ) and the mineral particle radius (r). First outlined to describe the frequency dependence of the polarization for colloidal particles (Schwarz, 1962), the relationship was later explored for the characterization of metallic minerals (Wong, 1979). However, further research is warranted, considering that observed changes in τ in our experiment might be related to both increases in the size (through accumulation) and in the volume of the metallic minerals. Pelton et al. (1978) also reported an ambiguous trend between the time constant (τ) and the volume and/or the size of iron sulfides. Wong and Strangway (1981) also demonstrated that the volume of metallic minerals might be underestimated in the model proposed by Wong (1979), if the shape of the minerals is not spherical. This observation was also confirmed in the study of Slater at al. (2007) performed on columns ongoing microbial transformations similar to those addressed in this study. Weller et al. (2010) proposed a model linking the polarization effect (σ'') and the surface area (of metallic minerals) per unit pore volume. However, our results show that σ'' is dependent on groundwater geochemistry (particularly Fe(II) concentrations) and not only on the geometry of metallic minerals (i.e., surface area), with such effect not

investigated in the model proposed by Weller et al. (2010). Moreover, our results exhibit a significant change in the polarization response (σ'') at different frequencies (< 64 Hz), which is not addressed in the model proposed by Weller et al. (2010).

Regarding the lack of an adequate petrophysical model and extensive ground truth information (e.g., direct measurements of volume or size of precipitated minerals at different time-lapses) as typically the case of field-scale experiments, this study does not address the quantification of changes in the pore-scale geometry. However, we believe that the images here presented might be relevant for the up-scaling of relationships observed in the laboratory.

6.4. Conclusions and Outlook

In this study we have presented SIP measurements in the frequency bandwidth from 0.06 to 256 Hz characterized by a low misfit between normal and reciprocal readings, particularly for acquisition frequencies below 64 Hz. The measured spectra revealed a significant peak in the low frequencies (< 64 Hz) and a typical increase in the phase measurements collected at frequencies above 32 Hz, most probably related to electromagnetic contamination of the data. These data sets represent a frequency bandwidth broader than previous studies performed at the site, which permitted the estimation of spectral (i.e., Cole-Cole) parameters, particularly of the polarization time constant. We have demonstrated that spatiotemporal variations observed in the images of Cole-Cole parameters are consistent with changes in groundwater geochemistry and the precipitation of iron sulfides (FeS) accompanying the stimulation of subsurface microbial activity. Although promising, the presented images need to be further validated with ground truth information. We also suggest the collection of SIP borehole data to improve the resolution at depth in the images and to better define the geometry of the observed anomalies. Additionally, we believe that the integral inversion of the time-lapse SIP measurements using an additional regularization with respect to time and frequency may improve the quality and consistency of the computed Cole-Cole parameters. We also consider that more research should be conducted to improve polarization models in presence of metallic minerals, in order to quantitatively correlate SIP parameters (e.g., m, τ) with changes in the size and volume of metallic minerals within the saturated pore space; such work is important for improving estimates of hydraulic properties of the aquifer and changes in such properties that can accompany bioremediation.

7. CONCLUSIONS

The studies presented here demonstrate that field-scale SIP imaging provide valuable information for an improved characterization of geochemical changes in the subsurface taking place due to the presence of certain contaminants and remediation processes. Imaging of the resistivity magnitude (or of the real component of the complex conductivity) has been confirmed as a suitable method for the characterization of lithological units with high spatial resolution. However, resistivity images reveal only a weak correspondence with variations in groundwater geochemistry caused by the presence of contaminants or during the remediation processes studied here. By contrast, resistivity phase images, as well as the images of the polarization effect (imaginary component of the complex resistivity), reveal spatiotemporal anomalies correlated to the distribution of contaminants, to variations in groundwater geochemistry and redox status of the aquifer materials and to changes in the pore space due to precipitation of minerals. Moreover, field procedures implemented here permitted the collection of SIP measurements in a wider frequency bandwidth than previous studies conducted at the field scale. The analysis of the spectral response of data sets collected in a wide frequency bandwidth permitted to solve the values of the characteristic time-constant (τ) and chargeability (m) in an imaging framework. The resulting images revealed anomalies consistent with changes in pore-space geometry due to the presence of NAPL contaminants and the precipitation of metallic minerals accompanying the bio-stimulation. However, correlations presented in this study can be site-specific and a certain calibration is probably required to achieve the characterization of a different site.

There are a vast number of studies regarding the data treatment and data error quantification for ERT measurements; however, this subject has received only little attention for SIP imaging to date. To overcome this, this work presents a methodology for data treatment and quantification of the error in SIP tomographic measurements. Such methodology has been applied to an extensive data base in different sites and for different time-lapses. Moreover, considering the number of the sources of systematical error for SIP measurements, an adequate methodology is necessary to assess the quality of the collected measurements. The analysis of the normal and reciprocal measurements has been demonstrated to provide a better insight into the quality of ERT measurements than other methodologies. Taking this into account, data quality in data sets presented in this study was evaluated with regard to the normal and reciprocal misfit. In order to increase the reciprocity of the data, measurements were conducted with carefully designed measuring protocols in order to avoid systematic errors. In order to quantify the data-error present in the SIP measurements presented here, a thorough statistical analysis of the misfit between normal and reciprocal readings for SIP measurements was performed. Hence, it is possible to conclude that although time consuming, the acquisition of reciprocal data sets provides an efficient and simple method to capture more potential sources of errors than for instance the simple repetition of measurements.

In order to investigate the existing assumptions regarding the data-error description in SIP data sets, a series of measurements were conducted in the laboratory (to minimize the source of error), as described in the third chapter of this work. The analysis of data sets collected in the laboratory revealed a clear correlation between the discrepancy in normal and reciprocal magnitude and phase measurements on the one hand and the corresponding mean resistance value on the other hand. Consistent with previous studies, the misfit between normal and reciprocal resistances measurements exhibited a linear increase with increasing the mean resistance value. However, results presented here, reveal a decreasing phase discrepancy with increasing resistance. Such pattern was observed for measurements collected with different measuring protocols and at different frequencies, over a wide frequency range. Other dependencies of the phase discrepancy, such as its dependence on the absolute phase value, were also studied, revealing an ambiguous behavior. Regarding the observed pattern, an error- model was proposed to quantify the error present in phase measurements. Such error-model is based on a power-law relationship between the phase error and the corresponding resistances measured. Resulting SIP images presented in this work show anomalies consistent with spatio-temporal changes expected as result of the presence of contaminants or due to processes accompanying remediation of the site. Hence, it is possible to conclude that the deployed methodology for data treatment and the proposed error model are an adequate way to deal with SIP measurements, for data sets collected at different frequencies and for different time-lapses.

Recent studies have claimed that measurements of integral chargeability in the time-domain - as commonly performed in modern field-scale commercial measuring devices -, or measurements performed in a single-frequency might provide as much information as those performed in a wide range of frequencies. The imaging results presented in the fourth chapter for data collected in the time- and frequency-domain demonstrate that measurements recorded in a wide frequency range might provide an improved site characterization, regarding the possibility to infer changes in the pore-space geometry based on existing petrophysical models. Imaging results for single frequency IP data sets (collected in the time-domain or frequency-domain) provide consistent results regarding the amplitude of the polarization effect (σ'', m), which might permit to determine particular SIP targets or a fast site characterization, considering the shorter acquisition times for IP and SIP surveys. The measurements were performed in an area of a former hydrogenation plant where high BTEX concentrations (> 1 g/l) have been reported.

Consistent with previous studies performed in the laboratory, an increase in the polarization effects (ϕ, σ'') in SIP images is observed for increasing concentrations of dissolved BTEX contaminants in groundwater (BTEX concentrations below saturation concentration); whereas an abrupt change to low polarization values is correlated with higher BTEX concentrations (>1.7 g/l), and occurrence of free-phase products. Such response is observed for all frequencies collected below 40 Hz; at such frequency the response is highly contaminated with EM coupling. The same pattern was observed for the polarization response (ϕ, σ'') for data collected in the time-domain. Furthermore, dissolved concentration of BTEX contaminants (>1.7 g/l) are associated with a typical Cole-Cole spectral response, characterized by a frequency peak (in frequencies < 40 Hz); whereas

higher BTEX concentrations, and presumably the occurrence of free-phase products, are associated with a flat spectra, i.e., a semi-constant polarization value for all acquisition frequencies (< 40 Hz).

Values of the total chargeability (*mtot*) and median relaxation-time ($\tau 50$) were obtained by Debye decomposition, in order to model the spectral response of those pixels associated with a flat spectra, not adequately described by means of a Cole-Cole model. The computed *mtot* values are consistent with the ϕ, σ'' values extracted from SIP and converted time-domain images. Furthermore, the median relaxation-time ($\tau 50$) reveals a strong positive correlation with BTEX concentrations, as observed in laboratory studies, accounting for a decrease in the pore space where the polarization can take place, due to the presence of NAPL contaminants displacing pore-water. Such observation is of particular interest, considering the need to up- scale models towards the development of a quantitative tool for the characterization of contaminated sites.

The results presented in this Thesis confirm that SIP images permit an improved interpretation over the analysis of single-frequency, or integral chargeability, imaging results, due to the possibility to discriminate different polarization mechanisms through the analysis of the frequency-dependence of the SIP response. Moreover, results presented in chapter four permitted to investigate the effect of anthropogenic structures (i.e., cultural noise) in the SIP images. The imaging results for data collected before and after the removal of anthropogenic structures (e.g., pipes, wires and foundations of the hydrogenation plant) demonstrate that useful information can still be retrieved from the images at some distance (a few meters) away from such structures. Electrical images obtained for data collected before and after the excavation of a trench show consistency in the electrical units, particularly for the saturated area (~ 8 m bgs).

The last two chapters demonstrated the potential of SIP images for the characterization of processes accompanying the remediation of contaminated sites. Here, the remediation approach based on the stimulation of indigenous microorganisms was efficiently used to remove dissolved uranium (U(VI)) from groundwater. Precipitation of iron sulfides accompanying the reduction of U(VI) provided an suitable target for SIP survey. Moreover, the stimulation of microbial growth permitted the evaluation of the SIP technique to assess the accumulation of microbial cells and the formation of biofilms, as suggested in recent studies performed at the laboratory scale. Imaging results presented in this study provide a characteristic response for four different processes: (i) delineation of natural bioreduction zones, where uranium is slowly removed from groundwater without amendment injections, characterized by a strong phase response, particularly at high measuring frequency; (ii) a noticeable decrease in the phase response (for all studied frequencies) was observed for measurements just after acetate injection during periods dominated by iron-reduction, characteristic of fast rates of uranium removal; (iii) low absolute phase values were observed for periods dominated by sulfate-reduction, characterized by less effective uranium removal; (iv) a significant increase in the phase response was observed for measurements collected after cessation of the amendment injection, consistent with subsequent decrease in dissolved U(VI).

The results presented here demonstrated that electrode polarization is the principal polarization mechanism underlying the response observed, due to the precipitation of metallic minerals (e.g., iron sulfides) as a consequence of the stimulation of iron- and sulfate-reducing bacteria. Moreover, a strong correlation was observed between high concentrations of aqueous Fe(II) and the polarization effect (ϕ, σ''), for periods when concentrations of Fe(II) were above a threshold value of ca. 50 μM. For periods dominated by sulfate-reduction, when the concentration of electroactive compounds (e.g., Fe(II) and perhaps other redox-sensitive metals) is below a critical concentration (50 μM), electrode polarization is minimized and other polarization mechanisms, such as electrochemical or membrane polarization, dominate. Such periods are characterized by a moderate phase response (absolute phase values below 10 mrad) in spite of the existence of metallic and clay minerals. As such, complex resistivity imaging might be a useful tool to determine when further biostimulation (i.e., resumed injection of organic carbon) is required in order to maintain conditions favorable for the immobilization of redox sensitive contaminants, such as uranium.

Improvements on the field procedures permitted the collection of SIP measurements in the frequency bandwidth from 0.06 to 256 Hz. These measurements exhibit a low misfit between normal and reciprocal readings, particularly for acquisition frequencies below 60 Hz. The measured spectra reveal a significant peak in the low frequencies (< 64 Hz) and a typical increase in the phase measurements collected at frequencies above 32 Hz, most probably related to electromagnetic contamination of the data. These data sets represent a frequency bandwidth broader than previous studies performed at the site, which permitted the estimation of spectral (i.e., Cole-Cole) parameters, particularly of the polarization time constant. As demonstrated in this work, observed spatiotemporal variations in the images of Cole-Cole parameters are consistent with changes in groundwater geochemistry and the precipitation of iron sulfides (FeS) accompanying the stimulation of subsurface microbial activity. However, due to the lack of sufficient ground truth information, it was not possible to validate the inferred changes in pore-space geometry (i.e., changes in hydraulic conductivity), as a result of the precipitation of minerals accompanying biostimulation. Furthermore, the existing electrochemical model linking the relaxation time (τ) and the mineral particle radius (r) resulted in ambiguous results regarding the quantification of changes in volume and size of metallic minerals.

8. PERSPECTIVES

Although the results presented in this study are very promising, more research is required to better understand the mechanisms underlying the polarization response observed. Moreover, experimental studies at the laboratory scale, in conjunction with field investigations, should be taken into considerations for the improvement of petrophysical models, a requierement for up-scaling. This study has demonstrated strong correlation between the SIP response and different geochemical parameters. However, a conclusive interpretation of the polarization mechanisms is still open to debate. In particular, more studies need to be conducted to identify the polarization response of dissolved contaminants and of free-phase products; to better understand the polarization enhanced through the chemical interactions between NAPL contaminants (e.g., BTEX) and groundwater; to better quantify the role of electroactive ions in electrode polarization in presence of metallic minerals; and to address the polarization of microbial cells (e.g., biofilms) for measurements at the field scale.

The collection of SIP borehole data is critical to improve the resolution at depth in the images and to better define the geometry of the observed anomalies. However, this needs to be combined with adequate field procedures, as those described in this study. Additionally, the integral inversion of the time-lapse SIP measurements using an additional regularization with respect to time and frequency may improve the quality and consistency of the computed images of spectral parameters (e.g., relaxation-time).

9. REFERENCES

Aal, G.Z.A., Atekwana, E.A., Rossbach, S. and Werkema, D.D., 2010. Sensitivity of geoelectrical measurements to the presence of bacteria in porous media. J. Geophys. Res., 115, G03017

Abdel Aal, G.A., Atekwana, E., Radzikowski, S. and Rossbach, S., 2009. Effect of bacterial adsorption on low frequency electrical properties of clean quartz sands and iron-oxide coated sands. Geophysical Research Letters, 36.

Abdel Aal, G.Z., Atekwana, E.A. and Slater, L.D., 2004. Effects of microbial processes on electrolytic and interfacial electrical properties of unconsolidated sediments. Geophysical Research Letters, 31(12).

Abdel Aal, G.Z., Slater, L.D. and Atekwana, E.A., 2006. Induced-polarization measurements on unconsolidated sediments from a site of active hydrocarbon biodegradation. Geophysics, 71(2): H13-H24.

Abernathy, S.M., Gil, R. and Akinyemi, A., 2007. ENVR 103-Remediation of Cr(VI) using zero-valent iron nanoparticles: Kinetics and stoichiometry. Abstracts of Papers of the American Chemical Society, 233: 421-421.

Ahn, J.S., Chon, C.M., Moon, H.S. and Kim, K.W., 2003. Arsenic removal using steel manufacturing byproducts as permeable reactive materials in mine tailing containment systems. Water Research, 37(10): 2478-2488.

Alfreider, A. and Vogt, C., 2007. Bacterial Diversity and Aerobic Biodegradation Potential in a BTEX-Contaminated Aquifer. Water, Air, & Soil Pollution, 183(1): 415-426.

Amir, A. and Lee, W., 2011. Enhanced reductive dechlorination of tetrachloroethene by nano-sized zero valent iron with vitamin B12. Chemical Engineering Journal, 170(2-3): 492-497.

Anderson, R.T., Vrionis, H.A., Ortiz-Bernad, I., Resch, C.T., Long, P.E., Dayvault, R., Karp, K., Marutzky, S., Metzler, D.R., Peacock, A., White, D.C., Lowe, M. and Lovley, D.R., 2003. Stimulating the in situ activity of Geobacter species to remove uranium from the groundwater of a uranium-contaminated aquifer. Applied and Environmental Microbiology, 69(10): 5884-5891.

Angoran, Y. and Madden, T.R., 1977. Induced polarization - preliminary study of its chemical basis. Geophysics, 42(4): 788-803.

Archie, G.E., 1942. The electrical resistivity log as an aid in determining some reservoir characteristics. Trans. Am. Inst. Min. Metall. Pet. Eng., 146: 54 - 67.

Aristodemou, E. and Thomas-Betts, A., 2000. DC resistivity and induced polarisation investigations at a waste disposal site and its environments. Journal of Applied Geophysics, 44(2-3): 275-302.

Arora, M., Snape, I. and Stevens, G.W., 2011. The effect of temperature on toluene sorption by granular activated carbon and its use in permeable reactive barriers in cold regions. Cold Regions Science and Technology, 66(1): 12-16.

Atekwana, E.A., Atekwana, E., Legall, F.D. and Krishnamurthy, R.V., 2005. Biodegradation and mineral weathering controls on bulk electrical conductivity in a shallow hydrocarbon contaminated aquifer. Journal of Contaminant Hydrology, 80(3-4): 149-167.

Atekwana, E.A. and Atekwana, E.A., 2010. Geophysical Signatures of Microbial Activity at Hydrocarbon Contaminated Sites: A Review. Surveys in Geophysics, 31(2): 247-283.

Atekwana, E.A., Atekwana, E.A., Werkema, D.D., Allen, P.J., Smart, L.A., Duris, J.W., Cassidy, D.P., Sauck, W.A. and Rossbach, S., 2004. Evidence for microbial enhanced electrical conductivity in hydrocarbon-contaminated sediments. Geophysical Research Letters, 31: L23501.

Atekwana, E.A., Sauck, W.A. and Werkema, D.D., 2000. Investigations of geoelectrical signatures at a hydrocarbon contaminated site. Journal of Applied Geophysics, 44(2-3): 167-180.

Atekwana, E.A. and Slater, L.D., 2009. Biogeophysics: A new frontier in Earth science research. Reviews of Geophysics, 47: RG4004.

Baciocchi, R., Boni, M.R. and D'Aprile, L., 2003. Characterization and performance of granular iron as reactive media for TCE degradation by permeable reactive barriers. Water Air and Soil Pollution, 149(1-4): 211-226.

Barkay, T. and Schaefer, J., 2001. Metal and radionuclide bioremediation: issues, considerations and potentials. Current Opinion in Microbiology, 4(3): 318-323.

Barnes, R.J., Riba, O., Gardner, M.N., Scott, T.B., Jackman, S.A. and Thompson, I.P., 2010. Optimization of nano-scale nickel/iron particles for the reduction of high concentration chlorinated aliphatic hydrocarbon solutions. Chemosphere, 79(4): 448-454.

Bayer, P., and Finkel, M. 2006. Life cycle assessment of active and passive groundwater remediation technologies. Journal of Contaminant Hydrology 83, 171-199.

Bauer, S., Bayer-Raich, M., Holder, T., Kolesar, C., Müller, D. and Ptak, T., 2004. Quantification of groundwater contamination in an urban area using integral pumping tests. Journal of Contaminant Hydrology, 75(3-4): 183-213.

Béland-Pelletier, C., Fraser, M., Barker, J. and Ptak, T., 2011. Estimating contaminant mass discharge: A field comparison of the multilevel point measurement and the integral pumping investigation approaches and their uncertainties. Journal of Contaminant Hydrology, 122(1-4): 63-75.

Bennett, P., He, F., Zhao, D., Aiken, B. and Feldman, L., 2010. In situ testing of metallic iron nanoparticle mobility and reactivity in a shallow granular aquifer. Journal of Contaminant Hydrology, 116(1-4): 35-46.

Bentley, L.R. and Gharibi, M., 2004. Two- and three-dimensional electrical resistivit y imaging at a heterogeneous remediation site. Geophysics, 69(3): 674-680.

Bezbaruah, A.N., Thompson, J.M. and Chisholm, B.J., 2009. Remediation of alachlor and atrazine contaminated water with zero-valent iron nanoparticles. Journal of Environmental Science and Health Part B-Pesticides Food Contaminants and Agricultural Wastes, 44(6): 518-524.

Bing, Z. and Greenhalgh, S.A., 2000. Cross-hole resistivity tomography using different electrode configurations. Geophysical Prospecting, 48(5): 887-912.

Binley, A. and Kemna, A., 2005. DC resistivity and induced polarization methods. In: R.a. Hubbard (Editor), Hydrogeophysics. Springer, pp. 129-156.

Binley, A., Kruschwitz, S., Lesmes, D. and Kettridge, N., 2010. Exploiting the temperature effects on low frequency electrical spectra of sandstone: A comparison of effective diffusion path lengths. Geophysics, 75(6): A43-A46.

Binley, A., Ramirez, A. and Daily, W., 1995. Regularised image reconstruction of noisy electrical resistance tomography data, Proceedings of the 4th workshop of the European concerted action on process tomography, pp. 401-410.

Binley, A., Slater, L.D., Fukes, M. and Cassiani, G., 2005. Relationship between spectral induced polarization and hydraulic properties of saturated and unsaturated sandstone. Water Resources Research, 41(12): W12147.

Blaschek, R., Hordt, A. and Kemna, A., 2008. A new sensitivity-controlled focusing regularization scheme for the inversion of induced polarization data based on the minimum gradient support. Geophysics, 73(2): F45-F54.

Blowes, D.W., Ptacek, C.J., Benner, S.G., McRae, C.W.T., Bennett, T.A. and Puls, R.W.,2000. Treatment of inorganic contaminants using permeable reactive barriers. Journal of Contaminant Hydrology, 45(1-2): 123-137.

Boopathy, R., 2000. Factors limiting bioremediation technologies. Bioresource Technology, 74(1): 63-67.

Börner, F., Gruhne, M. and Schön, J.H., 1993. Contamination indications derived from electrical properties in the low frequency range. Geophysical Prospecting, 41: 83-98.

Börner, F.D. and Schön, J.H., 1995. Low frequency complex conductivity measurements of microcrack properties. Surveys in Geophysics, 16(1): 121-135.

Boucher, M., Favreau, G., Descloitres, M., Vouillamoz, J.-M., Massuel, S., Nazoumou, Y. Cappelaere, B. and Legchenko, A., 2009. Contribution of geophysical surveys to groundwater modelling of a porous aquifer in semiarid Niger: An overview. Comptes Rendus Geosciences, 341(10-11): 800-809.

Bouwer, H., 2002. Artificial recharge of groundwater: hydrogeology and engineering. Hydrogeology Journal, 10(1): 121-142.

Bowling, J.C., Rodriguez, A.B., Harry, D.L. and Zheng, C.M., 2005. Delineating alluvial aquifer heterogeneity using resistivity and GPR data. Ground Water, 43(6): 890-903.

Calabro, P.S. and Moraci, N., 2010. Heavy metals removal and hydraulic performance in zero-valent iron/pumice permeable reactive barriers. Journal of Environmental Management, 91(11): 2336-2341.

Cassiani, G., Kemna, A., Villa, A. and Zimmermann, E., 2009. Spectral induced polarization for the characterization of free-phase hydrocarbon contamination of sediments with low clay content. Near Surface Geophysics, 7(5-6): 547-562.

Chambers, J.E., Kuras, O., Meldrum, P.I., Ogilvy, R.D. and Hollands, J., 2006. Electrical resistivity tomography applied to geologic, hydrogeologic, and engineering investigations at a former waste-disposal site. Geophysics, 71(6): B231-B239.

Chambers, J.E., Loke, M.H., Ogilvy, R.D. and Meldrum, P.I., 2004. Noninvasive monitoring of DNAPL migration through a saturated porous medium using electrical impedance tomography. Journal of Contaminant Hydrology, 68(1–2): 1-22.

Chambers, J.E., Wilkinson, P.B., Wealthall, G.P., Loke, M.H., Dearden, R., Wilson, R., Allen, D. and Ogilvy, R.D., 2010. Hydrogeophysical imaging of deposit heterogeneit y and groundwater chemistry changes during DNAPL source zone bioremediation. Journal of Contaminant Hydrology, 118(1-2): 43-61.

Chapman, S.W., Byerley, B.T., Smyth, D.J.A. and Mackay, D.M., 1997. A pilot test of passive oxygen release for enhancement of in situ bioremediation of BTEX- contaminated ground water. Ground Water Monitoring and Remediation, 17(2): 93-105.

Chen, J.S., Hubbard, S.S., Williams, K.H., Pride, S., Li, L., Steefel, C. and Slater, L., 2009a. A state-space Bayesian framework for estimating biogeochemical transformations using time-lapse geophysical data. Water Resources Research, 45.

Chen, J., Hubbard, S.S., Williams, H.K., Flores Orozco, A., and Kemna, A. 2012. Estimating the spatio-temporal distribution of geochemical parameters associated with biostimulation using spectral induced polarization data and hierarchical bayesian models. Water Resources Research 48, W05555.

Chen, L., Liu, F., Liu, Y., Dong, H. and Colberg, P.J.S., 2011. Benzene and toluene biodegradation down gradient of a zero-valent iron permeable reactive barrier. Journal of Hazardous Materials, 188(1-3): 110-115.

Chen, W., Hou, L., Luo, X. and Zhu, L., 2009b. Effects of chemical oxidation on sorption and desorption of PAHs in typical Chinese soils. Environmental Pollution, 157(6): 1894-1903.

Chen, Y.P. and Or, D., 2006. Effects of Maxwell-Wagner polarization on soil complex dielectric permittivity under variable temperature and electrical conductivity. Water Resources Research, 42(6): W06423.

Chesnut, D.A., 1994. Heterogeneity and Vapor Extraction Performance, Emerging Technologies in Hazardous Waste Management IV, pp. 8-32.

Choi, S.J., Choi, J.H. and Kim, Y.H., 2007. Reductive dechlorination and biodegradation of 2,4,6-trichlorophenol using sequential permeable reactive barriers: Laboratory studies. Chemosphere, 67(8): 1551-1557.

Cole, K.S. and Cole, R.H., 1941. Dispersion and absorption in dielectrics I. Alternating current characteristics. Journal of Chemical Physics, 9(4): 341-351.

Commer, M., Newman, G.A., Williams, K.H. and Hubbard, S.S., 2011. 3D induced-polarization data inversion for complex resistivity. Geophysics, 76(3): F157-F171.

Cortina, J.L., Gibert, O., de Pablo, J. and Ayora, C., 2010. In situ removal of arsenic from groundwater by using permeable reactive barriers of organic matter/limestone/zero- valent iron mixtures. Environmental Geochemistry and Health, 32(4): 373-378.

Cosenza, P., Ghorbani, A., Revil, A., Zamora, M., Schmutz, M., Jougnot, D. and Florsch, N., 2008. A physical model of the low-frequency electrical polarization of clay rocks. Journal of Geophysical Research-Solid Earth, 113(B8): -.

Crimi, M.L. and Siegrist, R.L., 2004. Association of cadmium with MnO2 particles generated during permanganate oxidation. Water Research, 38(4): 887-894.

Cundy, A.B., Hopkinson, L. and Whitby, R.L.D., 2008. Use of iron-based technologies in contaminated land and groundwater remediation: A review. Science of the Total Environment, 400(1-3): 42-51.

Dahlin, T., 2000. Short note on electrode charge-up effects in DC resistivity data acquisition using multi-electrode arrays. Geophysical Prospecting, 48(1): 181-187.

Dahlin, T., 2001. The development of DC resistivity imaging techniques. Computers & Geosciences, 27(9): 1019-1029.

Dahlin, T., Leroux, V. and Nissen, J., 2002. Measuring techniques in induced polarisation imaging. Journal of Applied Geophysics, 50(3): 279-298.

Daily, W. and Owen, E., 1991. Cross-Borehole Resistivity Tomography. Geophysics, 56(8): 1228-1235.

Daily, W. and Ramirez, A., 1995. Electrical-Resistance Tomography During in-Situ Trichloroethylene Remediation at the Savanna River Site. Journal of Applied Geophysics, 33(4): 239-249.

Daily, W., Ramirez, A., Binley, A. and Labrecque, D., 2004. Electrical Resistance Tomography - Theory and Practise. In: D. Butler (Editor), Near Surface Geophysics. SEG.

Daily, W.D. and Ramirez, A.L., 1984. Insitu Porosity Distribution Using Geophysical Tomography. Geophysical Research Letters, 11(6): 614-616.

Davis, C.A., Atekwana, E., Atekwana, E., Slater, L.D., Rossbach, S. and Mormile, M.R., 2006. Microbial growth and biofilm formation in geologic media is detected with complex conductivity measurements. Geophysical Research Letters, 33(18).

Day-Lewis, F.D. and Singha, K., 2008. Geoelectrical inference of mass transfer parameters using temporal moments. Water Resources Research, 44(5): -.

De Franco, R., Biella, G., Tosi, L., Teatini, P., Lozej, A., Chiozzotto, B., Giada, M., Rizzetto, F., Claude, C., Mayer, A., Bassan, V. and Gasparetto-Stori, G., 2009. Monitoring the saltwater intrusion by time lapse electrical resistivity tomography: The Chioggia test site (Venice Lagoon, Italy). Journal of Applied Geophysics, 69(3-4): 117-130.

De Ryck, S.M., Redman, J.D. and Annan, A.P., 1993. Geophysical monitoring of a controlled kerosene spill. In: R.S. Bell and C.M. Lepper (Editors), Symposium on the Application of Geophysics to Engineering and Environmental Problems (SAGEEP). Debye, P., 1929. Polar molecules: Chemical Catalog Co.

Destouni, G. and Graham, W., 1997. The influence of observation method on local concentration statistics in the subsurface. Water Resour. Res., 33(4): 663-676.

Dias, C.A., 2000. Developments in a model to describe low-frequency electrical polarization of rocks. Geophysics, 65(2): 437-451.

Dickinson, M. and Scott, T.B., 2010. The application of zero-valent iron nanoparticles for the remediation of a uranium-contaminated waste effluent. Journal of Hazardous Materials, 178(1-3): 171-179.

Dietrich, P. and Leven, C., 2006. Direct-push technologies. In: R. Kirsch (Editor), Ground-water Geophysics: A Tool for Hydrology. Springer, Berlin, pp. 321-340.

Dietze, M. and Dietrich, P., 2011. A field comparison of BTEX mass flow rates based on integral pumping tests and point scale measurements. Journal of Contaminant Hydrology, 122(1-4): 1-15.

Doherty, R., Kulessa, B., Ferguson, A.S., Larkin, M.J., Kulakov, L.A. and Kalin, R.M., 2010. A microbial fuel cell in contaminated ground delineated by electrical self-potential and normalized induced polarization data. J. Geophys. Res., 115, G00G08,

Elifantz, H., N'Guessan, L.A., Mouser, P.J., Williams, K.H., Wilkins, M.J., Risso, C., Holmes, D.E., Long, P.E. and Lovley, D.R., 2010. Expression of acetate permease-like (apl) genes in subsurface communities of Geobacter species under fluctuating acetate concentrations. Fems Microbiology Ecology, 73(3): 441-449.

Elliott, D.W. and Zhang, X.W., 2001. Field Assessment of Nanoscale Bimetallic Particles for Groundwater Treatment. Environmental Science \& Technology, 35(24): 4922-4926. Elliott, P., Ragusa, S. and Catcheside, D., 1998. Growth of sulfate-reducing bacteria under acidic conditions in an upflow anaerobic bioreactor as a treatment system for acid mine drainage. Water Research, 32(12): 3724-3730.

Englert, A., Hubbard, S.S., Williams, K.H., Li, L. and Steefel, C.I., 2009. Feedbacks Between Hydrological Heterogeneity and Bioremediation Induced Biogeochemical Transformations. Environmental Science & Technology, 43(14): 5197-5204.

Falta, R.W., Suresh Rao, P. and Basu, N., 2005. Assessing the impacts of partial mass depletion in DNAPL source zones: I. Analytical modeling of source strength functions and plume response. Journal of Contaminant Hydrology, 78(4): 259-280.

Farrell, J. and Mishra, D.B., 2004. Understanding nitrate reactions with zerovalent iron media in permeable reactive barriers. Abstracts of Papers of the American Chemical Society: U607-U607.

Feenstra, S., Mackay, D.M. and Cherry, J.A., 1991. A Method for Assessing Residual NAPL Based on Organic Chemical Concentrations in Soil Samples. Ground Water Monitoring & Remediation, 11(2): 128-136.

Ferrarese, E., Andreottola, G. and Oprea, I.A., 2008. Remediation of PAH-contaminated sediments by chemical oxidation. Journal of Hazardous Materials, 152(1): 128-139.

Fiandaca, G., Auken, E., Christiansen, A.V., and Gazoty, A. 2012. Time-domain-induced polarization: Full-decay forward modeling and 1D laterally constrained inversion of Cole-Cole parameters. Geophysics 77, E213-E225.

Finneran, K.T., Housewright, M.E. and Lovley, D.R., 2002. Multiple influences of nitrate on uranium solubility during bioremediation of uranium-contaminated subsurface sediments. Environmental Microbiology, 4(9): 510-516.

Fischer, A., Bauer, J., Meckenstock, R.U., Stichler, W., Griebler, C., Maloszewski, P., Kästner, M. and Richnow, H.H., 2006. A Multitracer Test Proving the Reliability of Rayleigh Equation-Based Approach for Assessing Biodegradation in a BTEX Contaminated Aquifer. Environmental Science & Technology, 40(13): 4245-4252.

Flores Orozco, A., Kemna, A., and Zimmermann, E. 2012a. Data error quantification in spectral induced polarization imaging. Geophysics 77 (3), E227-E237.

Flores Orozco, A., Kemna, A., Oberdörster, C., Zschornack, L., Leven, C., Dietrich, P., and Weiss, H. 2012b. Delineation of subsurface hydrocarbon contamination at a former hydrogenation plant using spectral induced polarization imaging. Accepted in Journal of Contaminant Hydrology.

Flores Orozco, A., Williams, H.K., and Kemna, A. 2012c. Time-lapse spectral induced polarization imaging of stimulated uranium bioremediation. Submitted to Near Surface Geophysics.

Flores Orozco, A., Williams, K.H., Long, P.E., Hubbard, S.S., and Kemna, A. 2011. Using complex resistivity imaging to infer biogeochemical processes associated with bioremediation of a uranium-contaminated aquifer. Journal of Geophysical Research 116, G03001.

Friis, A.K., Heron, G., Albrechtsen, H.J., Udell, K.S. and Bjerg, P.L., 2006. Anaerobic dechlorination and redox activities after full-scale Electrical Resistance Heating (ERH) of a TCE-contaminated aquifer. Journal of Contaminant Hydrology, 88(3-4): 219-234.

Frohlich, R.K. and Urish, D.W., 2002. The use of geoelectrics and test wells for the assessment of groundwater quality of a coastal industrial site. Journal of Applied Geophysics, 50(3): 261-278.

Gan, S., Lau, E.V. and Ng, H.K., 2009. Remediation of soils contaminated with polycyclic aromatic hydrocarbons (PAHs). Journal of Hazardous Materials, 172(2-3): 532-549.

Garambois, S., Senechal, P. and Perroud, H., 2002. On the use of combined geophysical methods to assess water content and water conductivity of near-surface formations. Journal of Hydrology, 259(1-4): 32-48.

Garg, S.K., Tripathi, M., Vikram, S. and Jain, R.K., 2011. Isolation and Growth Characteristics of Chromium(VI) and Pentachlorophenol Tolerant Bacterial Isolate from Treated Tannery Effluent for its Possible Use in Simultaneous Bioremediation. Indian Journal of Microbiology, 51(1): 61-69.

Ghorbani, A., Cosenza, P., Ruy, S., Doussan, C. and Florsch, N., 2008. Non-invasive monitoring of water infiltration in a silty clay loam soil using Spectral Induced Polarization. Water Resources Research, 44(8).

Gibson, T.L., Abdul, A.S. and Chalmer, P.D., 1998. Enhancement of in situ bioremediation of BTEX-contaminated ground water by oxygen diffusion from silicone tubing. Ground Water Monitoring and Remediation, 18(1): 93-104.

Gödeke, S., Richnow, H.-H., Wei, H., Fischer, A., Vogt, C., Borsdorf, H. and Schirmer, M., 2006. Multi tracer test for the implementation of enhanced in-situ bioremediation at a BTEX-contaminated megasite. Journal of Contaminant Hydrology, 87(3-4): 211-236. Goes, B.J.M. and Meekes, J.A.C., 2004. An Effective Electrode Configuration for the Detection of DNAPLs with Electrical Resistivity Tomography. Journal of Environmental and Engineering Geophysics, 9(3): 127-141.

Gorby, Y.A. and Lovley, D.R., 1992. Enzymic uranium precipitation. Environmental Science and Technology, 26(1): 205-207.

Grieger, K.D., Fjordboge, A., Hartmann, N.B., Eriksson, E., Bjerg, P.L. and Baun, A., 2010. Environmental benefits and risks of zero-valent iron nanoparticles (nZVI) for in situ remediation: Risk mitigation or trade-off? Journal of Contaminant Hydrology, 118(3-4): 165-183.

Hayes, K.F., Han, Y.S., Gallegos, T.J. and Demond, A.H., 2011. FeS-coated sand for removal of arsenic(III) under anaerobic conditions in permeable reactive barriers. Water Research, 45(2): 593-604.

He, F., Zhao, D. and Paul, C., 2009. Field assessment of carboxymethyl cellulose stabilized iron nanoparticles for in situ destruction of chlorinated solvents in source zones. Water Research, 44(7): 2360-2370.

Hördt, A., Blaschek, R., Kemna, A. and Zisser, N., 2007. Hydraulic conductivity estimation from induced polarisation data at the field scale - the Krauthausen case history. Journal of Applied Geophysics, 62(1): 33-46.

Hördt, A., Druiventak, A., Blaschek, R., Binot, F., Kemna, A., Kreye, P. and Zisser, N., 2009. Case histories of hydraulic conductivity estimation with induced polarization at the field scale. Near surface geophysics, 7(5-6): 529-545.

Jarsjö, J., Bayer-Raich, M. and Ptak, T., 2005. Monitoring groundwater contamination and delineating source zones at industrial sites: Uncertainty analyses using integral pumping tests. Journal of Contaminant Hydrology, 79(3-4): 107-134.

Jeen, S.-W., Gillham, R.W. and Blowes, D.W., 2006. Effects of Carbonate Precipitates on Long-Term Performance of Granular Iron for Reductive Dechlorination of TCE. Environmental Science & Technology, 40(20): 6432-6437.

Jeen, S.W., Gillham, R.W. and Przepiora, A., 2011. Predictions of long-term performance of granular iron permeable reactive barriers: Field-scale evaluation. Journal of Contaminant Hydrology, 123(1-2): 50-64.

Johnson, T.C., Versteeg, R.J., Ward, A., Day-Lewis, F.D. and Revil, A., 2010. Improved hydrogeophysical characterization and monitoring through parallel modeling and inversion of time-domain resistivity andinduced-polarization data. Geophysics, 75(4): WA27-WA41.

Jones, E.H., Reynolds, D.A., Wood, A.L. and Thomas, D.G., 2011. Use of Electrophoresis for Transporting Nano-Iron in Porous Media. Ground Water, 49(2): 172-183.

Jougnot, D., Ghorbani, A., Revil, A., Leroy, P. and Cosenza, P., 2010. Spectral induced polarization of partially saturated clay-rocks: a mechanistic approach. Geophysical Journal International, 180(1): 210-224.

Jozefczak, A. and Skumiel, A., 2011. Ultrasonic investigation of magnetic nanoparticles suspension with PEG biocompatible coating. Journal of Magnetism and Magnetic Materials, 323(11): 1509-1516.

Karaoulis, M., Revil, A., Werkema, D.D., Minsley, B.J., Woodruff, W.F. and Kemna, A., 2011. Time-lapse three-dimensional inversion of complex conductivity data using an active time constrained (ATC) approach. Geophysical Journal International, 187(1): 237-251.

Karn, B., Kuiken, T. and Otto, M., 2009. Nanotechnology and in Situ Remediation: A Review of the Benefits and Potential Risks. Environ Health Perspect, 117(12).

Kemna, A., 2000. Tomographic inversion of complex resistivity - theory and application, Ruhr-University of Bochum.

Kemna, A. and Binley, A., 1996. Complex electrical resistivity tomography for contaminant plume delineation In: E. Section (Editor), 2nd Meeting on Environmental and Engineering Geophysics. Environmetal and Engineering Geophysical Society pp. 196 - 199.

Kemna, A., Binley, A., Day-Lewis, F., Englert, A., Tezkan, B., Vanderborght, J., Vereecken, H. and Winship, P., 2006. Solute transport processes, Applied Hydrogeophysics. NATO Science Series IV Earth and Environmental Sciences, pp. 117-159.

Kemna, A., Binley, A., Ramirez, A. and Daily, W., 2000. Complex resistivity tomography for environmental applications. Chemical Engineering Journal, 77(1-2): 11-18.

Kemna, A., Binley, A. and Slater, L., 2004a. Crosshole IP imaging for engineering and environmental applications. Geophysics, 69(1): 97-107.

Kemna, A., Binley, A., Cassiani, G., Niederleithinger, E., Revil, A., Slater, L., Williams, K., Flores Orozco, A., Haegel, F.H., Hördt, A., Kruschwitz, S., Leroux, V., Titov, K., Zimmermann, E. 2011. An overview of the spectral induced polarization method for near-surface applications: Near Surface Geophysics, submitted.

Kemna, A., Münch, H.M., Titov, K., Zimmermann, E. and Vereecken, H., 2005. Relation of SIP relaxation time of sands to salinity, grain size and hydraulic conductivity, Near Surface 2005 - 11th European Meeting of Environmental and Engineering Geophysics, Palermo, Italy.

Kemna, A., Räkers, E. and Binley, A., 1997. Application of complex resistivity tomography to field data from a Kerosene-contaminated site, 3rd Mtg. Environmental and Engineering Geophysics. Environ. Eng. Geophys. Soc., pp. 151-154.

Kemna, A., Räkers, E. and Dresen, L., 1999. Field applications of complex resistivit y tomography, 69thAnn. Int. Mtg., Soc. Expl. Geophys., Expanded Abstracts, pp. 331 - 334.

Kemna, A., Vanderborght, J., Englert, A., Müller, K., Tillman, A. and Vereecken, H., 2004b. Characterization of structures and transport processes in a heterogeneous aquifer using electrical conductivity and induced polarization imaging, AGU Fall Meeting Abstracts, pp. Abstract #H13G-02.

Kemna, A., Vanderborght, J., Kulessa, B. and Vereecken, H., 2002. Imaging and characterisation of subsurface solute transport using electrical resistivity tomography (ERT) and equivalent transport models. Journal of Hydrology, 267(3-4): 125-146.

Kettridge, N., Comas, X., Baird, A., Slater, L., Strack, M., Thompson, D., Jol, H. and Binley, A., 2008. Ecohydrologically important subsurface structures in peatlands revealed by ground-penetrating radar and complex conductivity surveys. Journal of Geophysical Research-Biogeosciences, 113(G4).

Knox, R.C., Shau, B.J., Sabatini, D.A. and Harwell, J.H., 1999. Field Demonstration Studies of Surfactant-Enhanced Solubilization and Mobilization at Hill Air Force Base, Utah, Innovative Subsurface Remediation, pp. 49-63.

Köber, R., Schlicker, O., Ebert, M. and Dahmke, A., 2002. Degradation of chlorinated ethylenes by Fe0: inhibition processes and mineral precipitation. Environmental Geology, 41(6): 644-652.

Köstel, J., Kemna, A., Javaux, M., Binley, A. and Vereecken, H., 2008. Quantitative imaging of solute transport in an unsaturated and undisturbed soil monolith with 3-D ERT and TDR. Water Resources Research, 44: 12.

Krebsyuill, B., Harwell, J.H., Sabatini, D.A. and Knox, R.C., 1995. Economic-Considerations in Surfactant-Enhanced Pump-and-Treat Remediation. Surfactant-Enhanced Subsurface Remediation, 594: 265-278.

LaBrecque, D. and Daily, W., 2008. Assessment of measurement errors for galvanic-resistivity electrodes of different composition. Geophysics, 73(2): F55-F64.

LaBrecque, D.J., Miletto, M., Daily, W., Ramirez, A. and Owen, E., 1996. The effects of noise on Occam's inversion of resistivity tomography data. Geophysics, 61(2): 538-548.

Leroy, P., Revil, A., Kemna, A., Cosenza, P. and Ghorbani, A., 2008. Complex conductivity of water-saturated packs of glass beads. Journal of Colloid and Interface Science, 321(1): 103-117.

Lesmes, D.P. and Frye, K.M., 2001. Influence of pore fluid chemistry on the complex conductivity and induced polarization responses of Berea sandstone. Journal of Geophysical Research, 106(B3): 4079-4090.

Lesmes, D.P. and Morgan, F.D., 2001. Dielectric spectroscopy of sedimentary rocks. Journal of Geophysical Research-Solid Earth, 106(B7): 13329-13346.

Lessoff, S.C., Schneidewind, U., Leven, C., Blum, P., Dietrich, P. and Dagan, G., 2010. Spatial characterization of the hydraulic conductivity using direct-push injection logging. Water Resources Research, 46.

Li, L. and Benson, C.H., 2010. Evaluation of five strategies to limit the impact of fouling in permeable reactive barriers. Journal of Hazardous Materials, 181(1-3): 170-180.

Li, L., Steefel, C.I., Williams, K.H., Wilkins, M.J. and Hubbard, S.S., 2009. Mineral Transformation and Biomass Accumulation Associated With Uranium Bioremediation at Rifle, Colorado. Environmental Science \& Technology, 43(14): 5429-5435.

Li, Y.G. and Oldenburg, D.W., 2000. 3-D inversion of induced polarization data. Geophysics, 65(6): 1931-1945.

Linde, N., Binley, A., Tryggvason, A., Pedersen, L.B. and Revil, A., 2006. Improved hydrogeophysical characterization using joint inversion of cross-hole electrical resistance and ground-penetrating radar traveltime data. Water Resources Research, 42(12).

Loke, M.H., Acworth, I. and Dahlin, T., 2003. A comparison of smooth and blocky inversion methods in 2D electrical imaging surveys. Exploration Geophysics, 34(3).

Looms, M.C., 2007. Hydrogeological characterisation using cross-borehole ground penetrating radar and electrical resistivity tomography. PhD Thesis, University of Copenhagen, Copenhagen.

Lovley, D.R., Holmes, D.E. and Nevin, K.P., 2004. Dissimilatory Fe(III) and Mn(IV) reduction. Advances in Microbial Physiology, Vol. 49, 49: 219-286.

Lovley, D.R., Phillips, E.J.P., Gorby, Y.A. and Landa, E.R., 1991. Microbial Reduction of Uranium. Nature, 350(6317): 413-416.

Lowry, G.V., Saleh, N., Kim, H.J., Phenrat, T., Matyjaszewski, K. and Tilton, R.D., 2008. Ionic strength and composition affect the mobility of surface-modified Fe-0 nanoparticles in water-saturated sand columns. Environmental Science & Technology, 42(9): 3349-3355.

Mackay, D.M. and Cherry, J.A., 1989. Groundwater contamination: pump-and-treat remediation. Environmental Science and Technology, 23(6): 630-636.

Mackay, D.M., Wilson, R.D., Brown, M.J., Ball, W.P., Xia, G. and Durfee, D.P., 2000. A controlled field evaluation of continuous vs. pulsed pump-and-treat remediation of a VOC-contaminated aquifer: site characterization, experimental setup, and overview of results. Journal of Contaminant Hydrology, 41(1-2): 81-131.

Mackenzie, P.D., Horney, D.P. and Sivavec, T.M., 1999. Mineral precipitation and porosity losses in granular iron columns. Journal of Hazardous Materials, 68(1-2): 1-17.

Marshall, D. and Madden, T., 1959. Induced polarization, a study of its causes. Geophysics, 24: 790-816.

Mazac, O., Kelly, W.E. and Landa, I., 1987. Surface geoelectrics for groundwater pollution and protection studies. Journal of Hydrology, 93(3-4): 277-294.

McCall, W., Butler, J.J., Healey, J.M., Lanier, A.A., Sellwood, S.M. and Garnett, E.J., 2002. A dual-tube direct-push method for vertical profiling of hydraulic conductivity in unconsolidated formations. Environmental & Engineering Geoscience, 8(2): 75-84.

McCall, W., Nielsen, D., N., Farrington, S.P. and Christy, T.M., 2006. Use of Direct Push Technologies in Environmental Site Characterization and Ground-Water Monitoring, Practical handbook of environmental site characterization and ground-water monitoring. CRC Press taylor and Francis Group, Boca Raton, Florida, pp. 345-372.

McCarty, P.L., 2010. In Situ Remediation of Chlorinated Solvent Plumes. Springer New York, 786 pp.

Merriam, J.B., 2007. Induced polarization and surface electrochemistry. Geophysics, 72(4): F157-F166.

Militzer, H. and Weber, F., 1985. Angewandte Geophysik, Band 2 - Geoelektrik, Geothermik, Radiometrie, Aerogeophysik. Springer, Wien.

Miller, C.R., Routh, P.S., Brosten, T.R. and McNamara, J.P., 2008. Application of time-lapse ERT imaging to watershed characterization. Geophysics, 73(3): G7-G17.

Morgan, F.D. and Lesmes, D.P., 1994. Inversion for Dielectric-Relaxation Spectra. Journal of Chemical Physics, 100(1): 671-681.

Morrison, S.J., Carpenter, C.E., Metzler, D.R., Bartlett, T.R., Morris, S.A., David, L.N., Stan, J.M., Christopher, C.F. and James, A.D., 2003. Design and Performance of a Permeable Reactive Barrier for Containment of Uranium, Arsenic, Selenium, Vanadium, Molybdenum, and Nitrate at Monticello, Utah, Handbook of Groundwater Remediation using Permeable Reactive Barriers. Academic Press, San Diego, pp. 371- 399.

Morrison, S.J., Metzler, D.R. and Carpenter, C.E., 2001. Uranium Precipitation in a Permeable Reactive Barrier by Progressive Irreversible Dissolution of Zerovalent Iron. Environmental Science and Technology, 35(2): 385-390.

Morrison, S.J., Mushovic, P.S. and Niesen, P.L., 2006. Early Breakthrough of Molybdenum and Uranium in a Permeable Reactive Barrier. Environmental Science \& Technology, 40(6): 2018-2024.

Mouser, P.J., N'Guessan, A.L., Elifantz, H., Holmes, D.E., Williams, K.H., Wilkins, M.J., Long, P.E. and Lovley, D.R., 2009. Influence of Heterogeneous Ammonium Availability on Bacterial Community Structure and the Expression of Nitrogen Fixation and Ammonium Transporter Genes during in Situ Bioremediation of Uranium-Contaminated Groundwater. Environmental Science and Technology, 43(12): 4386-4392.

Muller, K., Vanderborght, J., Englert, A., Kemna, A., Huisman, J.A., Rings, J. and Vereecken, H., 2010. Imaging and characterization of solute transport during two tracer tests in a shallow aquifer using electrical resistivity tomography and multilevel groundwater samplers. Water Resources Research, 46.

N'Guessan, A.L., Elifantz, H., Nevin, K.P., Mouser, P.J., Methe, B., LWoodard, T., Manley, K., Williams, K.H., Wilkins, M.J., Larsen, J.T., Long, P.E. and Lovley, D.R., 2010. Molecular analysis of phosphate limitation in Geobacteraceae during the bioremediation of a uranium-contaminated aquifer. Isme Journal, 4(2): 253-266.

N´Guessan, A.L., Vrionis, H.A., Resch, C.T., Long, P.E. and Lovley, D.R., 2008. Sustained Removal of Uranium From Contaminated Groundwater Following Stimulation of Dissimilatory Metal Reduction. Environmental Science \& Technology, 42(8): 2999-3004.

Naftz, D.L., Fuller, C.C., Davis, J.A., Morrison, S.J., Feltcorn, E.M., Freethey, G.W., Rowland, R.C., Wilkowske, C., Piana, M., David, L.N., Stan, J.M., Christopher, C.F. and James, A.D., 2003. Field Demonstration of Three Permeable Reactive Barriers to Control Uranium Contamination in Groundwater, Fry Canyon, Utah, Handbook of Groundwater Remediation using Permeable Reactive Barriers. Academic Press, San Diego, pp. 401-434.

Nassir, S.S.A., Loke, M.H., Lee, C.Y. and Nawawi, M.N.M., 2000. Salt-water intrusion mapping by geoelectrical imaging surveys. Geophysical Prospecting, 48(4): 647-661. Naudet, V., Revil, A., Rizzo, E., Bottero, J.Y. and Begassat, P., 2004. Groundwater redox conditions and conductivity in a contaminant plume from geoelectrical investigations. Hydrology and Earth System Sciences, 8(1): 8-22.

Neculita, C.-M., Zagury, G.r.J. and BussiÃ¨re, B., 2007. Passive Treatment of Acid Mine Drainage in Bioreactors using Sulfate-Reducing Bacteria. J. Environ. Qual., 36(1): 1-16.

Newell, C.J., Bowers, R.L. and Rifai, H., 1994. Impact of non-aqueous ühase liquids (NAPLs) on groundwater remediation, Summer national AICHE meeting.

Nguyen, F., Kemna, A., Antonsson, A., Engesgaard, P., Kuras, O., Ogilvy, R., Gisbert, J., Jorreto, S. and Pulido-Bosch, A., 2009. Characterization of seawater intrusion using 2D electrical imaging. Near Surface Geophysics, 7(5-6): 377-390.

Nies, D.H., 1999. Microbial heavy-metal resistance. Applied Microbiology and Biotechnology, 51(6): 730-750.

Nikolaidis, N.P., Robbins, G.A., Scherer, M., McAninch, B., Binkhorst, G., Asikainen, J. and Suib, S.L., 1994. Vertical Distribution and Partitioning of Chromium in a Glaciof luvial Aquifer. Blackwell Publishing Ltd, pp. 150-159.

Nordsiek, S. and Weller, A., 2008. A new approach to fitting induced-polarization spectra. Geophysics, 73(6): F235-F245.

Ntarlagiannis, D., Williams, K., Slater, L., Hubbard, S. and Wu, Y., 2010. Investigating the effect of electro-active ion concentration on induced polarization signatures arising from biomineral formation. Geochimica Et Cosmochimica Acta, 74(12): A767-A767.

Ntarlagiannis, D., Williams, K.H., Slater, L. and Hubbard, S., 2005a. Low-frequency electrical response to microbial induced sulfide precipitation. Journal of Geophysical Research-Biogeosciences, 110(G2): G02009.

Ntarlagiannis, D., Yee, N. and Slater, L., 2005b. On the low-frequency electrical polarization of bacterial cells in sands. Geophysical Research Letters, 32(24): L24402.

Oberdörster, C., Vanderborght, J., Kemna, A. and Vereecken, H., 2010. Investigating Preferential Flow Processes in a Forest Soil Using Time Domain Reflectometry and Electrical Resistivity Tomography. Vadose Zone Journal, 9(2): 350-361.

Ogilvy, R.D., Meldrum, P.I., Kuras, O., Wilkinson, P.B., Chambers, J.E., Sen, M., Pulido-Bosch, A., Gisbert, J., Jorreto, S., Frances, I. and Tsourlos, P., 2009. Automated monitoring of coastal aquifers with electrical resistivity tomography. Near Surface Geophysics, 7(5-6): 367-375.

Oldenborger, G.A., Knoll, M.D., Routh, P.S. and LaBrecque, D.J., 2007. Time-lapse ERT monitoring of an injection/withdrawal experiment in a shallow unconfined aquifer. Geophysics, 72(4): F177-F187.

Oldenburg, D.W. and Li, Y.G., 1994. Inversion of Induced Polarization Data. Geophysics, 59(9): 1327-1341.

Oldenburg, D.W. and Li, Y.G., 1999. Estimating depth of investigation in dc resistivity and IP surveys. Geophysics, 64(2): 403-416.

Olhoeft, G.R., 1985. Low-Frequency Electrical-Properties. Geophysics, 50(12): 2492-2503. Or, D. and Wraith, J.M., 1999. Temperature effects on soil bulk dielectric permittivity measured by time domain reflectometry: A physical model (vol 35, pg 371, 1999). Water Resources Research, 35(7): 2283-2283.

Pelton, W.H. and Smith, P.K., 1976. Mapping porphyry copper deposits in the Philippines with IP. Geophysics, 41(1): 106-122.

Pelton, W.H., Ward, S.H., Hallof, P.G., Sill, W.R. and Nelson, P.H., 1978. Mineral discrimination and removal of inductive coupling with multifrequency IP. Geophysics, 43(3): 588-609.

Personna, Y.R., Ntarlagiannis, D., Slater, L., Yee, N., O'Brien, M. and Hubbard, S., 2008. Spectral induced polarization and electrodic potential monitoring of microbially mediated iron sulfide transformations. Journal of Geophysical Research- Biogeosciences, 113(G2).

Puls, R.W., Blowes, D.W. and Gillham, R.W., 1999. Long-term performance monitoring for a permeable reactive barrier at the U.S. Coast Guard Support Center, Elizabeth City, North Carolina. Journal of Hazardous Materials, 68(1-2): 109-124.

Puls, R.W. and Paul, C.J., 1997. Multi-layer sampling in conventional monitoring wells for improved estimation of vertical contaminant distributions and mass. Journal of Contaminant Hydrology, 25(1-2): 85-111.

Puls, R.W., Powell, R.M., Paul, C.J. and Blowes, D., 1998. Groundwater Remediation of Chromium Using Zero-Valent Iron in a Permeable Reactive Barrier, Innovative Subsurface Remediation, pp. 182-194.

Purvance, D.T. and Andricevic, R., 2000a. Geoelectric characterization of the hydraulic conductivity field and its spatial structure at variable scales. Water Resources Research, 36(10): 2915-2924.

Purvance, D.T. and Andricevic, R., 2000b. On the electrical-hydraulic conductivit y correlation in aquifers. Water Resources Research, 36(10): 2905-2913.

Qafoku, N.P., Kukkadapu, R.K., McKinley, J.P., Arey, B.W., Kelly, S.D., Wang, C., Resch, C.T. and Long, P.E., 2009. Uranium in Framboidal Pyrite from a Naturally Bioreduced Alluvial Sediment. Environmental Science and Technology, 43(22): 8528-8534.

Radhika, V., Subramanian, S. and Natarajan, K.A., 2006. Bioremediation of zinc using Desulfotomaculum nigrificans: Bioprecipitation and characterization studies. Water Research, 40(19): 3628-3636.

Ramirez, A., Daily, W., Binley, A. and LaBrecque, D., 1999. Electrical impedance tomography of known targets. Journal of Environmental and Engineering Geophysics, 4: 11-26.

Ramirez, A., Daily, W., Labrecque, D., Owen, E. and Chesnut, D., 1993. Monitoring an Underground Steam Injection Process Using Electrical-Resistance Tomography. Water Resources Research, 29(1): 73-87.

Rangsivek, R. and Jekel, M.R., 2005. Removal of dissolved metals by zero-valent iron (ZVI): Kinetics, equilibria, processes and implications for stormwater runoff treatment. Water Research, 39(17): 4153-4163.

Rein, A., Popp, S., Zacharias, S., Leven, C., Bittens, M. and Dietrich, P., 2011. Comparison of approaches for the characterization of contamination at rural megasites. Environmental Earth Sciences, 63(6): 1239-1249.

Revil, A. and Cosenza, P., 2010. Comment on "Generalized effective-medium theory of induced polarization" (Michael Zhdanov, 2008, Ggeophysics, 73, F197-F211). Geophysics, 75(2): X7-X9.

Revil, A. and Florsch, N., 2010. Determination of permeability from spectral induced polarization in granular media. Geophysical Journal International, 181(3): 1480-1498.

Revil, A. and Glover, P.W.J., 1998. Nature of surface electrical conductivity in natural sands, sandstones, and clays. Geophysical Research Letters, 25(5): 691-694.

Revil, A., Mendonca, C.A., Atekwana, E.A., Kulessa, B., Hubbard, S.S. and Bohlen, K.J., 2010. Understanding biogeobatteries: Where geophysics meets microbiology. Journal of Geophysical Research-Biogeosciences, 115.

Revil, A., Naudet, V. and Meunier, J.D., 2004. The hydroelectric problem of porous rocks: inversion of the position of the water table from self-potential data. Geophysical Journal International, 159(2): 435-444. Richardson, J.P. and Nicklow, J.W., 2002. In situ permeable reactive barriers for groundwater contamination. Soil & Sediment Contamination, 11(2): 241-268.

Revil, A., Karaoulis, M., Johnson, T., and Kemna, A. 2012. Review: Some low-frequency electrical methods for subsurface characterization and monitoring in hydrogeology. Hydrogeology Journal, 1-42. doi:10.1007/s10040-011-0819-x

Rubin, Y., and Hubbard, S. 2005. Hydrogeophysics. Springer. Dordrecht, Netherlands

Samanta, S.K., Singh, O.V. and Jain, R.K., 2002. Polycyclic aromatic hydrocarbons: environmental pollution and bioremediation. Trends in Biotechnology, 20(6): 243-248.

Sauck, W.A., 2000. A model for the resistivity structure of LNAPL plumes and their environs in sandy sediments. Journal of Applied Geophysics, 44(2-3): 151-165.

Schirmer, M., Dahmke, A., Dietrich, P., Dietze, M., Gödeke, S., Richnow, H.H., Schirmer, K., Weiß, H. and Teutsch, G., 2006a. Natural attenuation research at the contaminated megasite Zeitz. Journal of Hydrology, 328(3-4): 393-407.

Schädler, S., Morio, M., Bartke, S., and Finkel, M. 2011. Integrated planning and spatial evaluation of megasite remediation and reuse options. Journal of Contaminant Hydrology 127, 88-100.

Schädler, S., Morio, M., Bartke, S., Rohr-Zänker, R., and Finkel, M. 2010. Designing sustainable and economically attractive brownfield revitalization options using an integrated assessment model. Journal of Environmental Management 92, 827-837.

Schirmer, M., Godeke, S., Richnow, H.H., Weiss, H., Fischer, A., Vogt, C. and Borsdorf, H., 2006b. Multi tracer test for the implementation of enhanced in-situ bioremediation at a BTEX-contaminated megasite. Journal of Contaminant Hydrology, 87(3-4): 211-236.

Schmutz, M., Ghorbani, A., Vaudelet, P. and Revil, A., 2011. Spectral Induced Polarization Detects Cracks and Distinguishes between Open- and Clay-filled Fractures. Journal of Environmental and Engineering Geophysics, 16(2): 85-91.

Schmutz, M., Revil, A., Vaudelet, P., Batzle, M., Femenía Viñao, P. and Werkema, D., 2010. Influence of oil saturation upon spectral induced polarization of oil bearing sands. Geophysical Journal International, 183(1): 211-224.

Schrick, B., Hydutsky, B.W., Blough, J.L. and Mallouk, T.E., 2004. Tailoring the surface of metallic nanoparticles for environmental remediation. Abstracts of Papers of the American Chemical Society, 227: U1440-U1440.

Schrick, B., Ponder, S.M. and Mallouk, T.E., 2000. Remediation of chlorinated hydrocarbons using supported zero valent nickel-iron nanoparticles. Abstracts of Papers of the American Chemical Society, 220: U362-U362.

Schulmeister, M.K., Butler, J.J., Healey, J.M., Zheng, L., Wysocki, D.A. and McCall, G.W., 2003. Direct-push electrical conductivity logging for high-resolution hydrostratigraphic characterization. Ground Water Monitoring and Remediation, 23(3): 52-62.

Schwarz, G., 1962. A theory of the low-frequency dielectric dispersion of colloidal particles in electrolyte solution. The Journal of Physical Chemistry, 66(12): 2636-2642.

Scott, J.B.T. and Barker, R.D., 2003. Determining pore-throat size in Permo-Triassic sandstones from low-frequency electrical spectroscopy. Geophysical Research Letters, 30(9): -.

Seigel, H.O., 1959. Mathematical formulation and type curves for induced polarization. Geophysics, 24(3): 547-565.

Seigel, H.O., Vanhala, H. and Sheard, S.N., 1997. Some case histories of source discrimination using time-domain spectral IP. Geophysics, 62(5): 1394-1408.

Sethi, R., Vecchia, E.D., Coisson, M., Appino, C. and Vinai, F., 2009. Magnetic Characterization and Interaction Modeling of Zerovalent Iron Nanoparticles for the Remediation of Contaminated Aquifers. Journal of Nanoscience and Nanotechnology, 9(5): 3210-3218.

Singha, K. and Gorelick, S.M., 2006. Effects of spatially variable resolution on field-scale estimates of tracer concentration from electrical inversions using Archie's law. Geophysics, 71(3): G83-G91.

Singhal, D.C., Niwas, S., Shakeel, M. and Adam, E.M., 1998. Estimation of hydraulic characteristics of alluvial aquifers from electrical resistivity data. Journal of the Geological Society of India, 51(4): 461-470.

Skold, M., Revil, A. and Vaudelet, P., 2011. The pH dependence of spectral induced polarization of silica sands: Experiment and modeling. Geophysical Research Letters, 38.

Slater, L., 2007. Near surface electrical characterization of hydraulic conductivity: From petrophysical properties to aquifer geometries - A Review. Surveys in Geophysics, 28(2): 169-197.

Slater, L. and Binley, A., 2006. Synthetic and field-based electrical imaging of a zerovalent iron barrier: Implications for monitoring long-term barrier performance. Geophysics, 71(5): B129-B137.

Slater, L., Binley, A.M., Daily, W. and Johnson, R., 2000. Cross-hole electrical imaging of a controlled saline tracer injection. Journal of Applied Geophysics, 44(2-3): 85-102.

Slater, L. and Lesmes, D., 2002a. IP interpretation in environmental investigations. Geophysics, 67: 77.

Slater, L. and Lesmes, D.P., 2002b. Electrical-hydraulic relationships observed for unconsolidated sediments. Water Resources Research, 38(10).

Slater, L., Ntarlagiannis, D., Personna, Y.R. and Hubbard, S., 2007. Pore-scale spectral induced polarization signatures associated with FeS biomineral transformations. Geophysical Research Letters, 34(21).

Slater, L., Ntarlagiannis, D. and Wishart, D., 2006. On the relationship between induced polarization and surface area in metal-sand and clay-sand mixtures. Geophysics, 71(2): A1-A5.

Slater, L.D., Choi, J. and Wu, Y.X., 2005. Electrical properties of iron-sand columns: Implications for induced polarization investigation and performance monitoring of iron-wall barriers. Geophysics, 70(4): G87-G94.

Slater, L.D. and Glaser, D.R., 2003. Controls on induced polarization in sandy unconsolidated sediments and application to aquifer characterization. Geophysics, 68(5): 1547-1558.

Slater, L.D., Ntarlagiannis, D., Day-Lewis, F.D., Mwakanyamale, K., Versteeg, R.J., Ward, A., Strickland, C., Johnson, C.D. and Lane, J.W., 2010. Use of electrical imaging and distributed temperature sensing methods to characterize surface water-groundwater exchange regulating uranium transport at the Hanford 300 Area, Washington. Water Resources Research, 46.

Slater, L.D. and Reeve, A., 2002. Investigating peatland stratigraphy and hydrogeology using integrated electrical geophysics. Geophysics, 67(2): 365-378.

Soga, K., Page, J.W.E. and Illangasekare, T.H., 2004. A review of NAPL source zone remediation efficiency and the mass flux approach. Journal of Hazardous Materials, 110(1-3): 13-27.

Sogade, J.A., Scira-Scappuzzo, F., Vichabian, Y., Shi, W.Q., Rodi, W., Lesmes, D.P. and Morgan, F.D., 2006. Induced-polarization detection and mapping of contaminant plumes. Geophysics, 71(3): B75-B84.

Spitzer, K. and Chouteau, M., 2003. A dc resistivity and IP borehole survey at the Casa Berardi gold mine in northwestern Quebec. Geophysics, 68(2): 453-463.

Stummer, P., Maurer, H. and Green, A.G., 2004. Experimental design: Electrical resistivit y data sets that provide optimum subsurface information. Geophysics, 69(1): 120-139.

Sumanovac, F., 2006. Mapping of thin sandy aquifers by using high resolution reflection seismics and 2-D electrical tomography. Journal of Applied Geophysics, 58(2): 144-157.

Sumner, J.S., 1976. Principles of induced polarization for geophysical exploration. Elsevier, Amsterdam.

Taghavy, A., Costanza, J., Pennell, K.D. and Abriola, L.M., 2010. Effectiveness of nanoscale zero-valent iron for treatment of a PCE-DNAPL source zone. Journal of Contaminant Hydrology, 118(3-4): 128-142.

Telford, W.M., Geldart, L.P. and Sheriff, R.E., 1991. Applied geophysics (second edition). Cambridge University Press, Cambridge, 770 pp.

Theron, J., Walker, J.A. and Cloete, T.E., 2008. Nanotechnology and Water Treatment: Applications and Emerging Opportunities. Critical Reviews in Microbiology,34(1):43-69.

Tillmann, A., Englert, A., Nyari, Z., Fejes, I., Vanderborght, J. and Vereecken, H., 2008. Characterization of subsoil heterogeneity, estimation of grain size distribution and hydraulic conductivity at the Krauthausen test site using Cone Penetration Test. Journal of Contaminant Hydrology, 95(1-2): 57-75.

Titov, K., Kemna, A., Tarasov, A. and Vereecken, H., 2004. Induced polarization of unsaturated sands determined through time domain measurements. Vadose Zone Journal, 3(4): 1160-1168.

Titov, K., Komarov, V., Tarasov, V. and Levitski, A., 2002. Theoretical and experimental study of time domain-induced polarization in water-saturated sands. Journal of Applied Geophysics, 50(4): 417-433.

Tong, M.S., Li, L., Wang, W.N., Fan, Q.H., Jiang, Y.Z., Zhang, J.J., Ding, Z. and Cui, J., 2005a. Estimation of pore size distribution and permeability of shaly sands from induced polarization time spectra. Chinese Journal of Geophysics-Chinese Edition, 48(3): 710-716.

Tong, M.S., Li, L., Wang, W.N. and Jiang, Y.H., 2006. Determining capillary-pressure curve, pore-size distribution, and permeability from induced polarization of shaley sand. Geophysics, 71(3): N33-N40.

Tong, M.S., Li, L., Wang, W.N., Jiang, Y.Z., Shi, D.Q. and Du, G.T., 2005b. Multi-exponential inversion and laboratory study of Induced Polarization relaxation time spectra of shaly sands. Journal of Canadian Petroleum Technology, 44(11): 32-38.

Tong, M.S., Wang, W.N., Li, L., Jiang, Y.Z. and Shi, D.Q., 2004. Estimation of permeabilit y of shaly sand reservoir from induced polarization relaxation time spectra. Journal of Petroleum Science and Engineering, 45(1-2): 31-40.

Tsai, T.T., Kao, C.M. and Wang, J.Y., 2011. Remediation of TCE-contaminated groundwater using acid/BOF slag enhanced chemical oxidation. Chemosphere, 83(5): 687-692.

Ulrich, C. and Slater, L.D., 2004. Induced polarization measurements on unsaturated, unconsolidated sands. Geophysics, 69(3): 762-771.

Urish, D.W., 1981. The Practical Application of Surface Geoelectrics to Detection of Groundwater Pollution. Ground Water, 19(4): 442-443.

Urynowicz, M.A. and Siegrist, R.L., 2005. Interphase mass transfer during chemical oxidation of TCE DNAPL in an aqueous system. Journal of Contaminant Hydrology, 80(3-4):93-106.

van Voorhis, G.D., Nelson, P.H. and Drake, T.L., 1973. Complex resistivity spectra of porphyry copper mineralization. Geophysics, 38(1): 49-60.

Vanhala, H., 1997. Mapping oil-contaminated sand and till with the spectral induced polarization (SIP) method. Geophysical Prospecting, 45(2): 303-326.

Vanhala, H., Soininen, H. and Kukkonen, I., 1992. Detecting Organic-Chemical Contaminants by Spectral-Induced Polarization Method in Glacial Till Environment. Geophysics, 57(8): 1014-1017.

Varanasi, P., Fullana, A. and Sidhu, S., 2007. Remediation of PCB contaminated soils using iron nano-particles. Chemosphere, 66(6): 1031-1038.

Vaudelet, P., Schmutz, M., Pessel, M., Franceschi, M., Guérin, R., Atteia, O., Blondel, A., Ngomseu, C., Galaup, S., Rejiba, F. and Bégassat, P., 2011. Mapping of contaminant plumes with geoelectrical methods. A case study in urban context. Journal of Applied Geophysics, 75(4): 738-751.

Vesela, L., Nemecek, J., Siglova, M. and Kubal, M., 2006. The biofiltration permeable reactive barrier: Practical experience from Synthesia. International Biodeterioration & Biodegradation, 58(3-4): 224-230.

Vieth, A., Kästner, M., Schirmer, M., Weiß, H., Gödeke, S., Meckenstock, R.U. and Richnow, H.H., 2005. Monitoring in situ biodegradation of benzene and toluene by stable carbon isotope fractionation. Environmental Toxicology and Chemistry, 24(1):51-60.

Vignola, R., Cova, U., Fabiani, F., Grillo, G., Molinari, M., Sbardellati, R. and Sisto, R., 2008. Remediation of hydrocarbon contaminants in groundwater using specific zeolites in full-scale pump&treat and demonstrative Permeable barrier tests. In: R. Vignola et al. (Editors). Elsevier, pp. 573-576.

Vinegar, H. and Waxman, M., 1984. Induced polarization of shaly sands. Geophysics, 49(8): 1267-1287.

Vrionis, H.A., Anderson, R.T., Ortiz-Bernad, I., O'Neill, K.R., Resch, C.T., Peacock, A.D., Dayvault, R., White, D.C., Long, P.E. and Lovley, D.R., 2005. Microbiological and geochemical heterogeneit y in an in situ uranium bioremediation field site. Applied and Environmental Microbiology, 71(10): 6308-6318.

Wachter, T.F., Dethlefsen, F., Gödeke, S. and Dahmke, A., 2004. Räumlich-statistische Charakterisierung der Hydrogeochemie einer BTEX-Grundwasserkontamination am Standort "RETZINA"/Zeitz. Grundwasser, 9(1): 21 - 32.

Ward, S.H. 1990. Resistivity and Induced Polarization Methods. Society of Exploration Geophysicists.

Waxman, M.H. and Smits, L.J.M., 1968. Electrical Conductivities in Oil-Bearing Shaly Sands. Society of Petroleum Engineers Journal, 8(2): 107-&.

Weichgrebe, D. and Vogelpohl, A., 1994. A comparative study of wastewater treatment by chemical wet oxidation. Chemical Engineering and Processing, 33(4): 199-203.

Weidelt, P. and Weller, A., 1997. Computation of geoelectrical configuration factors for cylindrical core samples. Scientific Drilling, 6: 27-34.

Weller, A. and Börner, F.D., 1996. Measurements of spectral induced polarization for environmental purposes. Environmental Geology, 27(4): 329-334.

Weller, A., Slater, L., Nordsiek, S. and Ntarlagiannis, D., 2010. On the estimation of specific surface per unit pore volume from induced polarization: A robust empirical relation fits multiple data sets. Geophysics, 75(4): WA105.

West, C.C., 1992. Surfactant-Enhanced Solubilization of Tetrachloroethylene and Degradation Products in Pump and Treat Remediation. Acs Symposium Series, 491:149-158.

Wilkin, R.T. and Lee, T.R., 2010. Iron hydroxy carbonate formation in zerovalent iron permeable reactive barriers: Characterization and evaluation of phase stability. Journal of Contaminant Hydrology, 116(1-4): 47-57.

Wilkin, R.T., Puls, R.W. and Sewell, G.W., 2003. Long-term performance of permeable reactive barriers using zero-valent iron: Geochemical and microbiological effects. Ground Water, 41(4): 493-503.

Wilkin, R.T., Su, C., Ford, R.G. and Paul, C.J., 2005. Chromium-Removal Processes during Groundwater Remediation by a Zerovalent Iron Permeable Reactive Barrier. Environmental Science \& Technology, 39(12): 4599-4605.

Wilkins, M.J., VerBerkmoes, N.C., Williams, K.H., Callister, S.J., Mouser, P.J., Elifantz, H., N'Guessan, A.L., Thomas, B.C., Nicora, C.D., Shah, M.B., Abraham, P., Lipton, M.S., Lovley, D.R., Hettich, R.L., Long, P.E. and Banfield, J.F., 2009. Proteogenomic Monitoring of Geobacter Physiology during Stimulated Uranium Bioremediation. Appl. Environ. Microbiol., 75(20): 6591-6599.

Will, B.N., Schrick, B., Blough, J.L., Vogel, A.J. and Mallouk, T.E., 2003. Remediation of chlorinated hydrocarbon contaminants using supported bimetallic nanoparticles. Abstracts of Papers of the American Chemical Society, 225: U972-U972.

Williams, K.H., Kemna, A., Wilkins, M.J., Druhan, J., Arntzen, E., N'Guessan, A.L., Long, P.E., Hubbard, S.S. and Banfield, J.F., 2009. Geophysical Monitoring of Coupled Microbial and Geochemical Processes During Stimulated Subsurface Bioremediation. Environmental Science and Technology, 43(17): 6717-6723.

Williams, K.H., Long, P.E., Davis, J.A., Wilkins, M.J., N'Guessan, A.L., Steefel, C.I., Yang, L., Newcomer, D., Spane, F.A., Kerkhof, L.J., McGuinness, L., Dayvault, R. and Lovley, D.R., 2011. Acetate availability and its influence on sustainable bioremediation of uranium-contaminated groundwater. Geomicrobiology Journal, 28(5-6): 519-539.

Williams, K.H., Ntarlagiannis, D., Slater, L.D., Dohnalkova, A., Hubbard, S.S. and Banfield, J.F., 2005. Geophysical imaging of stimulated microbial biomineralization. Environmental Science and Technology, 39(19): 7592-7600.

Wilopo, W., Sasaki, K., Hirajima, T. and Yamanaka, T., 2008. Immobilization of Arsenic and Manganese in Contaminated Groundwater by Permeable Reactive Barriers Using Zero Valent Iron and Sheep Manure. Materials Transactions, 49(10): 2265-2274.

Wisitsoraat, A., Tuantranont, A., Patthanasettakul, V. and Mongpraneet, S., 2008. Electron field emission from ZnOx nanoparticles decorated on vertically aligned carbon nanotubes prepared by vapor-phase transport. Journal of Vacuum Science and Technology B, 26(5): 1757-1760.

Wong, J., 1979. An electrochemical model of the induced-polarization phenomenon in disseminated sulfide ores. Geophysics, 44(7): 1245-1265.

Wong, J. and Strangway, D.W., 1981. Induced Polarization in Disseminated Sulfide Ores Containing Elongated Mineralization. Geophysics, 46(9): 1258-1268.

Wu, Y., Slater, L., Versteeg, R. and LaBrecque, D., 2008. A comparison of the low frequency electrical signatures of iron oxide versus calcite precipitation in granular zero valent iron columns. Journal of Contaminant Hydrology, 95(3-4): 154-167.

Wu, Y., Slater, L.D. and Korte, N., 2005. Effect of Precipitation on Low Frequency Electrical Properties of Zerovalent Iron Columns. Environmental Science & Technology, 39(23): 9197-9204.

Wu, Y., Versteeg, R., Slater, L. and LaBrecque, D., 2009. Calcite precipitation dominates the electrical signatures of zero valent iron columns under simulated field conditions. Journal of Contaminant Hydrology, 106(3-4): 131-143.

Wu, Y.X., Hubbard, S., Williams, K.H. and Ajo-Franklin, J., 2010. On the complex conductivity signatures of calcite precipitation. Journal of Geophysical Research-Biogeosciences, 115.

Xu, B. and Noel, M., 1993. On the completness of data sets with multieelectrode systems for electrical resistivity survey. Geophysical Prospecting, 41(6): 791-801.

Yao, W.S. and Millero, F.J., 1996. Oxidation of hydrogen sulfide by hydrous Fe(III) oxides in seawater. Marine Chemistry, 52(1): 1-16.

Yu Ting, W., Shian Chee, W., Chih Ming, C., De Huang, H. and Hsing Lung, L., 2009. Iron Nanoparticles for In Situ Groundwater Remediation of Chlorinated Organic Solvents in Taiwan, Environmental Applications of Nanoscale and Microscale Reactive Metal Particles, pp. 233-243.

Zaporozec, A. and Miller, J.C., 2000. Groundwater Pollution, UNESCO, Paris, France. Zekster, I. and Margat, J., 2004. Groundwater resources of the world and their use. UNESCO-IHP, Paris.

Zhang, D., Wei, S., Kaila, C., Su, X., Wu, J., Karki, A.B., Young, D.P. and Guo, Z., 2010. Carbon-stabilized iron nanoparticles for environmental remediation. Nanoscale, 2(6):917-919.

Zhang, W.X., Wang, C.-B. and Lien, H.-L., 1998. Treatment of chlorinated organic contaminants with nanoscale bimetallic particles. Catalysis Today, 40(4): 387-395.

Zhang, W.Z., 2004. Iron awe - nanoparticles for mine site remediation. Materials World, 12(4): 33-34.

Zhang, Y. and Gillham, R.W., 2005. Effects of Gas Generation and Precipitates on Performance of Fe° PRBs. Ground Water, 43(1): 113-121.

Zhou, D.M., Cang, L., Wu, D.Y. and Alshawabkeh, A.N., 2009. Coupling Electrokinetics with Permeable Reactive Barriers of Zero-Valent Iron for Treating a Chromium Contaminated Soil. Separation Science and Technology, 44(10): 2188-2202.

Zimmermann, E., Kemna, A., Berwix, J. and Glaas, W., 2007. EIT Measurement System with High Phase Accuracy for the Imaging of Spectral Induced Polarization Properties of Soils and Sediments, 5th World Congress on Industrial Process Tomography, Bergen, Norway.

Zimmermann, E., Kemna, A., Berwix, J., Glaas, W., Munch, H.M. and Huisman, J.A., 2008. A high-accuracy impedance spectrometer for measuring sediments with low polarizability. Measurement Science & Technology, 19(10).

Zisser, N., Kemna, A. and Nover, G., 2010a. Dependence of spectral-induced polarization response of sandstone on temperature and its relevance to permeability estimation. Journal of Geophysical Research-Solid Earth, 115.

Zisser, N., Kemna, A. and Nover, G., 2010b. Relationship between low-frequency electrical properties and hydraulic permeability of low-permeability sandstones. Geophysics, 75(3): E131-E141.